

Thin Film Precursors, Properties and Applications:
Chemical Vapour Deposition and Atomic Layer Deposition
of Group 4, 11 and 13 Elements and Their Oxides

by

Peter George Gordon

A thesis submitted to the Faculty of Graduate and Postdoctoral
Affairs in partial fulfilment of the requirements for the degree of
Doctor of Philosophy

in

Chemistry

Carleton University
Ottawa, Ontario
Canada

August 2013

© 2013, Peter George Gordon

Abstract

Brass and bronze substrates were coated by atomic layer deposition (ALD) with alumina and titania in small and large scale batches. These films were evaluated for use as protective and cosmetic coatings. Optimization of deposition parameters for uniform coatings both on individual coins and across a batch for Al_2O_3 and TiO_2 films was performed. The effect of film thickness on colour was examined. High-quality, uniform coatings were achieved with multi-pulse programs.

The interference colours resulting from thin films of Al_2O_3 deposited by ALD on silicon were analyzed using a robotic gonireflectometer. A series of thin films were deposited and their reflectivity values obtained for the visible spectrum. A comparison of these values with the predictions of computer simulations has revealed deviations from predicted reflectivities. The effect of these discrepancies on perceived colour appearance was investigated. Simulation predicts larger iridescence than what was observed.

Alumina films were deposited by ALD on flat and nanostructured silicon substrates, and incorporated into PEDOT- Al_2O_3 -silicon architectures that were then evaluated as photovoltaic devices. The reverse saturation currents observed on flat devices made with Al_2O_3 films were similar devices made with an SiO_2 layer. The structured samples with Al_2O_3 showed a considerable increase in efficiency (of up to five times) over the equivalent flat samples.

A new indium(III) guanidinate, $(\text{In}[(\text{N}^i\text{Pr})_2\text{CNMe}_2]_3)$, was synthesized.

Thermogravimetric analysis showed elemental indium was produced from the compound as a residual mass. Thermolysis in a sealed NMR tube showed carbodiimide and

protonated dimethyl amine by ^1H NMR. Chemical vapour deposition (CVD) experiments above 275 °C with air as the reactant gas produced cubic indium oxide films with good transparency.

Dimeric silver(I) and gold(I) tert-butyl-imino-2,2-dimethylpyrrolidines were synthesized and evaluated for thermal stability by thermal gravimetric analysis, differential scanning calorimetry and variable-temperature solution NMR. The compounds were used to deposit metallic films on silicon and glass substrates by CVD, with and without a flow of heated nitrogen gas. The compounds decomposed to produce metallic films at 140 °C for the silver compound and 300 °C for the gold compound. Additional CVD experiments with heated nitrogen gas flow improved film uniformity without sacrificing film purity.

Preface

This preface provides full bibliographical details for each article included in this thesis, as well as whether the article is reproduced in whole or in part. Use of copyrighted material is likewise acknowledged here. When citing material from this thesis, please cite both the thesis and the article relevant to the chapter, if the chapter is based on a publication.

Pursuant to the Integrated Thesis policy of Carleton University, the “supervisor” (Seán T. Barry) and the “student” (Peter G. Gordon) confirm that the student was fully involved in setting up and conducting the research, obtaining data and analyzing results, as well as preparing and writing the material presented in the co-authored article(s) integrated in the thesis. Additionally, the supervisor confirms the information provided by the student in this preface.

Chapter 1

Figure 1.5 is reprinted with permission from the American Institute of Physics.

Chapter 3

Gordon, P. G.; Baribeau, R.; Barry, S. T.; Goniocolorimetric Study of Aluminum Oxide Films Deposited by Atomic Layer Deposition, *Thin Solid Films*, **2012**, 520, 2943.

The article is wholly reproduced and edited for formatting and clarity of presentation.

The student performed all work related to deposition and characterization of films (with the exception of gonio-colourelectrometry) and simulations. Writing was collaborative between all co-authors.

Chapter 4

Demtchenko, S.; McGarry, S.; **Gordon, P. G.**; Barry, S. T.; Tarr, N. G.; Characterization and assessment of a novel hybrid organic/inorganic metal-insulator-semiconductor structure for photovoltaic applications, *Proc.SPIE 7750*, **2010**, DOI 10.1117/12.871360.

The article is wholly reproduced and edited for formatting and clarity of presentation.

The student performed all work related to deposition of alumina films and thickness characterization. Writing was collaborative between all co-authors.

Chapter 5

Gordon, P. G.; Ward, M. J.; Heikkila, M. J.; Monillas, W. H.; Yap, G. P. A.; Ritala, M.; Leskelä, M.; Barry, S. T.; Chemical Vapour Deposition of In₂O₃ Thin Films from a tris-Guanidinate Indium Precursor, *Dalton Trans.*, **2011**, 40, 9425.

The article is wholly reproduced and edited for formatting and clarity of presentation.

The student performed all work related to synthesis of precursors, deposition of films, thickness characterization, SEM and resistance measurements. Writing was collaborative between all co-authors.

Chapter 6

Coyle, J. P.; **Gordon, P. G.**; Wells, A. P.; Sirianni, E. R.; Yap, G. P. A.; Barry, S. T.; Thermally Robust Gold and Silver Iminopyrrolidines for Chemical Vapour Deposition of Metal Films, *Chem. Mater.*, **2013**, *submitted*. Manuscript ID: cm-2013-02658c.

Chapter 6 includes data presented in the as-yet unpublished manuscript referenced above, as well as additional unreported Ag and Au CVD data. J.P. Coyle is the corresponding author for the submitted manuscript.

The student performed all work related to deposition of metal films (with the exception of gold depositions without nitrogen flow), thickness characterizations, resistance measurements and SEM imaging.

Acknowledgements

It is a pleasure to thank the many people who made the long road to this thesis not only possible, but thoroughly enjoyable.

It is difficult to overstate my gratitude to my Ph.D. supervisor, Dr. Seán T. Barry. The extent to which I understand chemistry can in large part be attributed to his generosity, knack for explaining things clearly and simply, and his willingness to let me pursue my own path. Throughout my return to graduate studies, he provided encouragement, sound advice, good teaching, interesting challenges, amazing opportunities, and friendship.

I am indebted to my many Barry Lab student colleagues for providing untold hours of thoughtful discussion and foolish shenanigans in nearly equal measure. In roughly chronological order I would especially like to thank Allison Brazeau, Yamile Wasslen, Julie Delahunt, Jason Coyle, Agnieszka Kurek and Peter Pallister. From my increasingly distant undergraduate years, I would like to thank Mark Flumiani for helping me stumble through the first leg of this journey, and for his enduring friendship.

I would like to thank the staff and faculty of the Chemistry Department at Carleton. I will always remain amazed at my good fortune to have worked with such a great group of people.

I would like to thank my extended family for their unrelenting support. In particular I would like to thank my step-parents Joseph Smarkala and Nancy Gordon, both for supporting me in my schooling and for the love and support they have provided my parents over the years.

I could never thank Erin Christine Sallie enough for her depth of patience, generosity, and life-changing love. I am not sure I could have made it this far without her. She is the heart of my heart.

Lastly, and most importantly, I wish to thank my loving parents, Susan Lynne Smarkala and Donald Davey Gordon. They created me, raised me, taught me to cultivate my curiosity (among a great many other things), and always supported me without question. It is to them that I dedicate this thesis.

Table of Contents

Abstract.....	2
Preface.....	4
Acknowledgements.....	6
Table of Contents.....	7
Chapter 1 - Introduction.....	1
1.1 Chemical Vapour Deposition and Atomic Layer Deposition.....	1
1.2 ALD for Protective and Cosmetic Coatings	11
1.3 Photovoltaic Devices.....	17
Chapter 2 - Protective and Cosmetic Coatings for Coinage Metals and Their Alloys	
.....	21
2.1 Abstract.....	21
2.2 Introduction.....	21
2.3 Results and Discussion.....	23
2.4 Experimental.....	35
2.5 Conclusions.....	39
Chapter 3 - Goniocolorimetric Study of Aluminum Oxide Films Deposited by	
Atomic Layer Deposition.....	41
3.1 Abstract.....	41
3.2 Introduction.....	42
3.3 Experimental.....	43
3.4 Results and Discussion.....	47
3.5 Conclusions.....	63

Chapter 4 - Characterization and assessment of a novel hybrid organic/inorganic metal-insulator-semiconductor structure for photovoltaic applications.....	64
4.1 Abstract.....	64
4.2 Introduction.....	65
4.3 Experimental.....	68
4.4 Results and Discussion.....	71
4.5 Future Work.....	77
4.6 Acknowledgements.....	78
Chapter 5 - Chemical vapour deposition of In₂O₃ thin films from a tris-guanidinate indium precursor.....	79
5.1 Abstract.....	79
5.2 Results and Discussion.....	80
5.3 Thermolysis	85
5.4 Film depositions and characterization.....	87
5.5 Experimental.....	96
5.6 Conclusions.....	100
Chapter 6 - Metallic Silver and Gold Chemical Vapour Deposition from Novel Precursors.....	102
6.1 Abstract.....	102
6.2 Introduction.....	103
6.3 Results and Discussion.....	105
6.4 Experimental.....	127
6.5 Conclusion.....	135
Chapter 7 - Conclusions.....	138

References.....	143
-----------------	-----

List of Tables

Table 2.1 Single-point thickness measurements of film thickness on bronze and silicon substrates as measured by ellipsometry. The last row indicates the percentage difference in observed values for the two substrates.....	24
Table 2.2 Pulse program timing used in the bulk ALD experiments for alumina and titania coatings. Each row represents a single ALD cycle, yielding a monolayer of target material. The metal precursors are represented by "M" and all values are in seconds.	38
Table 4.1 Voltage intercepts from the V-C characterization of flat MIS devices with SiO ₂ insulator showing increasing barrier height with increasing oxidation temperature.....	73
Table 4.2 Predicted parameters of the optimized flat MIS device with SiO ₂ insulator and PEDOT as the metal.....	75
Table 5.1 Selected crystal data and structure refinement parameters for compound 1....	82
Table 5.2 Selected bond lengths and angles for compound 1.....	83
Table 5.3 The various deposition runs undertaken using different masses of 1 as the precursor and air as the reactant gas.....	88
Table 6.1 Selected bond lengths and angles for 1 and 2.....	107

List of Figures

Figure 1.1 Various CVD apparatus configurations.....	3
Figure 1.2 Thermal decomposition routes available to copper guanidates (analogous routes available to amidates).....	7
Figure 1.3 2,2-diethyl-tertbutyl-iminopyrrolidine described and studied in Chapter 6, highlighting features that prevent decomposition routes observed for amidate and guanidate analogs.....	7
Figure 1.4 Schematic of the ALD process: a) the first precursor is introduced and a monolayer is formed; b) an N ₂ purge and evacuation removes remaining precursor and volatile side products; c) the second precursor is introduced and reacts with the first monolayer, forming the first monolayer of the target film; d) another N ₂ purge and evacuation removes remaining precursor and volatile side products. e) The process is repeated until the desired thickness is reached.	9
Figure 1.5 Table summarizing materials grown by ALD. Reprinted with permission from American Institute of Physics. ¹²⁴ Copyright 2013, AIP Publishing LLC.....	10
Figure 1.6 Model illustrating the origin of interference colours. A is an incident beam of light at a specific frequency. Due to partial reflection, it splits into beam C and B. Depending upon the thickness of the film (d) and the angle of incidence of A, the path length C+D may alter the phase of E with respect to B. Constructive or destructive interference may then occur, altering the wavelength of the outgoing light. The refractive indices of the materials are given by n ₁ , n ₂ and n ₃	14
Figure 1.7 Representation of the CIE Lab coordinate system for describing colour.	16

Figure 1.8 Band structure diagram for a Schottky barrier diode. E_C is the conduction band, E_F the Fermi level, and E_V the valence band.	18
Figure 2.1 An uncoated coin (b) is contrasted against a coin with a 1000 Å alumina coating (a) and a coin with a 1500 Å coating (c).	24
Figure 2.2 Acetamidinato alkyl aluminum precursor employed in this work.....	24
Figure 2.3 Deposition series showing coins in the top two rows and their respective silicon witness slides at the bottom. From left to right, each column presents coatings of 1000 Å, 3000Å, 8000 Å and 10,000 Å. The second witness slide is shown at two different viewing angles to demonstrate its iridescence, while the last slide exhibits delamination. Note that this delamination was observed to a much lesser degree on the coin.	26
Figure 2.4 Iridescence of 3000 Å film of Al_2O_3 on bronze.	27
Figure 2.5 SEM image of a coin coated with 1000 Å Al_2O_3 , after electrodeposition experiment. Copper metal (white) indicates a flaw in the film exposing the coin to the electrodeposition solution.	28
Figure 2.6 Thickness results for three pulse programs, revealing uniformity throughout the volume of a single batch run. Error bars depict standard deviations (evaluated across all eleven samples) of 72 Å, 20 Å and 10 Å for the single, double and triple pulse program thickness measurements respectively. Image at right depicts the placement of witness slides used for ellipsometric thickness measurements. Racks without witnesses are not shown but were present and fully loaded.....	32
Figure 2.7 XPS spectra of a bare token exposed to a TiO_2 ALD process (a) and a token with a 1200 Å Al_2O_3 coating exposed to the same TiO_2 ALD process (b). The shape of the	

baseline in a suggests a rough surface. Note that no aluminum oxide process was applied to sample a; the Al signal is marked there for comparison with b.	35
Figure 2.8 Custom-built ALD tool schematic.....	36
Figure 2.9 Empty coin racks (left) and filled, after deposition (right). Note the variation in interference colour on the coins and racks, clearly indicating non-uniform thickness..	38
Figure 3.1 Acetamidinato alkyl aluminum precursor employed in this work.	43
Figure 3.2 Schematic of the atomic layer deposition system.	44
Figure 3.3 The gonireflectometer used to collect reflectance data.....	47
Figure 3.4 Experimental data (a) and calculated data (b) of the reflectance of films of various thicknesses with a viewing angle of 10°	49
Figure 3.5 Experimental and calculated regular reflectance of a 459 \AA film over the visible range of light at various viewing angles.....	50
Figure 3.6 Plot of percent difference between experimental and calculated values for reflectance against wavelength and viewing angle for a bare silicon (100) wafer. Note that the topographical scale is in the range -2 to $+2\%$	51
Figure 3.7 Plot of percent difference between experimental and calculated values for reflectance against wavelength and viewing angle for a 1613 \AA Al_2O_3 film on a silicon (100) wafer. Note that the topographical scale is much larger than in Figure 3.6, ranging from -25% to $+90\%$	52
Figure 3.8 Reflectivity calculations for a 459 \AA aluminum oxide film on silicon using a) the bulk dispersion curve for aluminum oxide and b) the dispersion curve as measured experimentally for an aluminum oxide film deposited by ALD.....	54

Figure 3.9 a*b* CIELAB (CIE D65) plots of (a) observed and (b) calculated data for selected film thicknesses over a range of viewing angles. Coloured axes are approximate representations of the CIELAB space to help guide the eye.....	55
Figure 3.10 a*b* CIELAB (CIE D65) plots comparing +/- 5% error estimates for (a) 908 Å and (b) 1613 Å films with observed data. Each point corresponds to a viewing angle.	61
Figure 4.1 Representations of the hybrid MIS device. Flat device is shown in (a), nanostructured device shown in (b) and band diagram in (c).	68
Figure 4.2 Processing and testing of devices: (a) 2” wafer of devices (b) testing of an individual device under the solar simulator.....	71
Figure 4.3 I-V characteristics of flat MIS devices with SiO ₂ (a) full dark IV curves (b) dark reverse saturation current.....	72
Figure 4.4 Illuminated I-V characteristic of an MIS device with no intentional oxide; (a) measured under a solar simulator (b) measured under a halogen lamp with a sintered back contact and a non-sintered contact.....	74
Figure 4.5 I-V curves for flat MIS devices with Al ₂ O ₃ insulator (a) in the dark and (b) under illumination.....	76
Figure 4.6 Nanostructured MIS devices; (a) SEM image of surface structuring and (b) relative power conversion efficiency of a set of structured and flat MIS devices processed in parallel with 8 Å Al ₂ O ₃ insulator.....	77

Figure 5.1 X-ray crystal structure of $\text{In}[(\text{N}^i\text{Pr})_2\text{CNMe}_2]_3$ (1), ellipsoids shown at 30% probability, all H atoms removed for clarity. CCDC reference number 815078. For

crystallographic data in CIF or other electronic format see DOI: 10.1039/c1dt10877h.. .83

Figure 5.2 Thermogravimetric (TG) (black) and differential thermogravimetric (DTG) (gray) curves for 1, using a heating rate of 10 °C/min. The inset shows the potential onset of thermal degradation of the precursor.....85

Figure 5.3 The X-ray diffractogram of the film deposited in run b. The vertical lines indicate the expected diffraction peaks for cubic indium oxide.89

Figure 5.4 Narrow XPS spectra for indium 3d and oxygen 1s signals from run b. Values from the literature for the location of the elemental signals are shown and the two components used to fit the O 1s signal are indicated with dashed lines.^{156,157} The oxygen signals due to crystalline and amorphous material are labelled as such. Indium signals were fitted using only one component per peak.....90

Figure 5.5 A side-on SEM of the indium oxide film deposited in run b.....91

Figure 5.6 Total pressure in the CVD reactor for runs c–g, with the temperature profile (common to all runs) shown in light grey.....92

Figure 5.7 A UV-Vis difference spectrum where the absorbance of a bare borosilicate glass slide has been subtracted from the absorbance of the same slide coated with In_2O_3 (run b).....93

Figure 5.8 HTXRD measurement of the crystallization of cubic In_2O_3 under vacuum from a film deposited at 300 °C (run h). The three-dimensional plot shows the evolution of the peaks for cubic indium oxide as a function of temperature. Weak reflections

observed at room temperature and at the highest temperature originate from the sample holder.	95
Figure 5.9 CVD apparatus used for the deposition of indium oxide from 1 and air.....	99
Figure 6.1 Amidinates, guanidates, and iminopyrrolidates ligands used in precursors for CVD and ALD (R, R' = any alkyl group).....	105
Figure 6.2 Synthesis of silver(I) and gold(I) tert-butyl-imino-2,2-dimethylpyrrolidinate.	106
Figure 6.3 Molecular diagram of 2 with thermal ellipsoids at 30% probability. Hydrogen atoms omitted for clarity. Ag analogue compound 1 is isomorphic with 2.	108
Figure 6.4 Thermogravimetric analysis of 1 (black) and 2 (gray). Experiments were run under 1 atm nitrogen with a ramp rate of 10 °C/min. Sample size for 1 and 2 were 10.49 mg and 13.65 mg, respectively. Note that the maximum percentage residual mass of pure metal for 1 and 2 would be 39.35 % and 54.23 % respectively.	109
Figure 6.5 Isothermal TGA of (a) 1 and (b) 2. Isothermal temperatures, indicated in the right hand legend (°C), were reached at a rate of 40 °C/min. Sample sizes were between 3.10 mg and 3.67 mg.	110
Figure 6.6 Differential scanning calorimetry of 1, 2, and 3 in hermetically sealed aluminum pans. Temperature ramp was 10 °C/min up to 325 °C. Sample masses were 1.066 mg, 1.625 mg, and 3.790 mg for 1, 2, and 3, respectively. Exotherms are up.....	112
Figure 6.7 Evaporation kinetics of 1 (♦), 2 (■) and 3 (●).....	114
Figure 6.8 Decomposition of 1 and 2 in solution (C ₆ D ₆) measured by ¹ H NMR.....	116

Figure 6.9 Film thicknesses measured from the CVD of 1 (bottom) and 2 (top) at different furnace temperatures. Depositions with 1 consumed 50 - 60 mg of compound. Depositions for 2 consumed varying amounts: 13.9 mg (300 °C); 21.8 mg (350 °C); 5.9 mg (400 °C); 20.6 mg (450 °C); 23.5 (500 °C)..... 119

Figure 6.10 SEM images for thin films deposited without N₂ flow from (a, b) 1 and (c, d) 2 at 200 °C and 350 °C, respectively. Images from the CVD of 1 were measured (a) 0.75 cm and (b) 7.75 cm from the precursor inlet. Images from the CVD of 2 were measured (c) 5 cm and (d) 11 cm from the precursor inlet. Film thicknesses in a, b, and c are approximately 87 nm, 23 nm and 123 nm respectively. A reliable film thickness measurement for d could not be obtained. 120

Figure 6.11 Temperature series for silver CVD from 1 with nitrogen flow. 122

Figure 6.12 Film thicknesses for Ag CVD from 1 with heated N₂ flow, measured by AFM. 123

Figure 6.13 Thickness profile for Ag CVD at 300 °C, with nitrogen flow, comparing values obtained by SEM and AFM. 124

Figure 6.14 Comparison of CVD growth of gold from 2, with (dotted lines) and without (solid lines) nitrogen flow. The triangular data points depict the temperature gradient of the furnace tube. Intermediate temperatures of 350 °C and 400 °C (not shown) result in similar, intermediate growth. 126

Figure 6.15 CVD apparatus with attachment for heated nitrogen delivery. Dotted lines indicate the three separately-controlled heating zones. 132

Figure 6.16 Example of histogram technique used to determine film thickness from AFM data. Data shown is from a gold deposition from 2 at 350 °C, 8 cm from the precursor inlet.....134

Chapter 1 - Introduction

This chapter provides an introduction to the central theoretical and practical concepts addressed herein. The overarching theme in this work is the chemistry and practical applications of thin film depositions. The characterization of both the deposited films and the precursors used to create the films will be addressed. Two techniques for film deposition were studied: Chemical Vapour Deposition (CVD) and Atomic Layer Deposition (ALD). Both techniques are based on similar fundamentals regarding optimal precursor design and have similar process parameters, but there are very important differences.

1.1 Chemical Vapour Deposition and Atomic Layer Deposition

Chemical Vapour Deposition

Chemical vapour deposition (CVD) is a gas-phase thin film deposition method in which a chemical precursor is entrained in a continuous flow over a substrate. This precursor or a reactive intermediate then chemisorbs on the surface. Co-reactant gasses such as oxygen or nitrogen may also be introduced to assist in forming oxides or nitrides, for example. The driving energy for the chemistry at the surface can be supplied in a variety of ways including electrical discharge, exposure to light, or exposure to heat. The focus here will be on thermal processes. For clean films with high growth rates there are several criteria that CVD precursors (or their reactive intermediates) must meet. They must not react or decompose in the gas phase to produce unreactive species or particulate

material (unless this is the intent). Such terminal reactions in the gas phase lead to poor film coverage and poor film adhesion. Steric bulk and low molecular weight are ideal for high volatility at low temperatures, which keeps the energy demands of the system low. Halides are avoided as they tend to get incorporated into films as impurities, potentially altering the desired electrical properties even at very low concentrations.¹ More broadly, undesirable contaminants should in general be excluded from precursor design where possible. As an example, it is best to avoid oxygen-containing precursors if your target film is a nitride, as undesirable precursor decomposition may result in impurities.

The path and nature of mass transport, i.e. the manner in which the precursor is delivered to the substrate, has a large impact on the uniformity of the resulting film (or films, where multiple individual substrates are coated in the same experiment). Several reactor designs are used; some common examples are illustrated below (Figure 1.1). In each, the same processes are at work at the substrate surface: diffusion and adsorption of precursor, surface diffusion and reactions of adsorbed species, desorption and diffusion of volatile reaction products, and film growth. Operating pressures vary from tens of mTorr to 1 atm and reactor temperatures vary from room temperature to 1500 K.² Because film growth is dependent upon substrate orientation as well as heat and mass flow, different CVD reactors may yield significantly different results under otherwise identical conditions. Each process must be tuned to a given reactor; even on the same apparatus repeatability can be elusive without proper attention to detail.

There are processes for an extremely wide variety of materials and applications including semiconductors (e.g. Si, Ge, III–V, II–VI) for microelectronics, optoelectronics, and energy conversion devices (e.g. solar cells), dielectrics (e.g. SiO₂, AlN, Si₃N₄, etc.) and metallic films (W, Pt, Mo, Al, Cu, etc.) for microelectronics, refractory ceramic materials (e.g. TiB₂, SiC, B₄C, BN, TiN, Al₂O₃, ZrO₂, MoSi₂, diamond, etc.) used for protection against wear, corrosion, thermal shock, neutron adsorption or as diffusion barriers, and ceramic fibres (e.g. SiC and C) and ceramic matrix composites (e.g. SiC/SiC, SiC/C).³ Additionally there are many CVD processes reported that create one- and two-dimensional features such as inorganic nanowires (Si, Ge, Ge₂Sb₂Te₅, GeTe, In₂Se₃), carbon nanotubes and graphene.^{4,5}

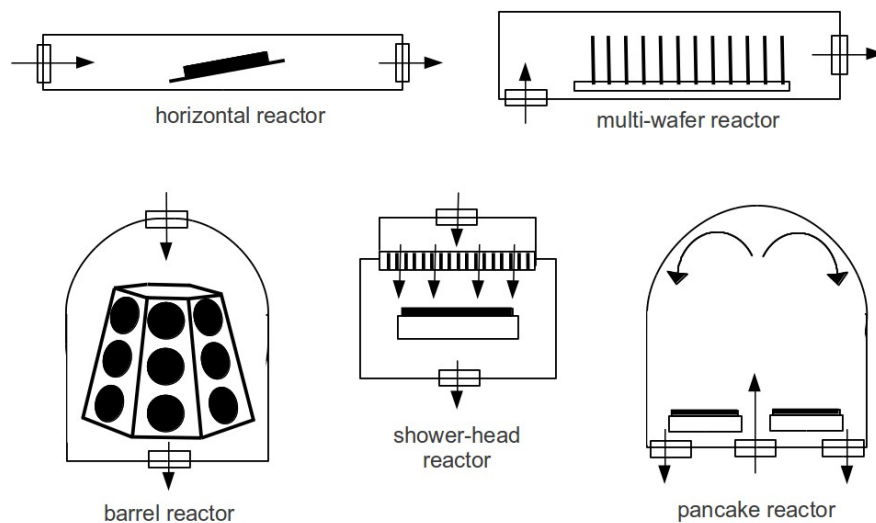


Figure 1.1 Various CVD apparatus configurations.

CVD of Indium Oxide

Indium oxide (both doped and un-doped) is a very useful transparent semiconducting oxide material with a wide band gap. Thin films of In₂O₃ are used in photovoltaic

devices,⁶ electro-optical devices,^{7,8} anti-reflection coatings,⁹ and as a sensor of various oxidizing gases.¹⁰⁻¹² Amorphous and crystalline indium oxide has been previously prepared by evaporation and sputtering,¹³ spray pyrolysis,¹⁴ atomic layer deposition (ALD),^{15,16} thermal oxidation, ion assisted deposition, pulsed laser deposition,¹⁷ and various forms of chemical vapour deposition (CVD).^{18,19} Deposition temperatures range from as low as 100 °C to 450 °C, and resistivities from as low as 2.74 mΩ·cm have been reported.^{20,15}

As mentioned above, thermal CVD is a relatively fast and straightforward way to deposit thin, smooth and conformal films on the nanometre to micrometre scale. The CVD of indium oxide has previously been studied using trimethyl indium ($\text{In}(\text{CH}_3)_3$) and triethyl indium ($\text{In}(\text{CH}_2\text{CH}_3)_3$),²¹ indium aminoalcohols and ketoimines,²² indium 2,2,6,6-tetramethyl-3,5-heptanedionate ($\text{In}(\text{thd})_3$) and indium acetylacetonates ($\text{In}(\text{acac})_3$),²³ and indium alkoxides ($\text{In}(\text{OR})_3$).²⁴ Chapter 5 presents work on the synthesis of the indium guanidinate precursor $\text{In}[(\text{N}^i\text{Pr})_2\text{CNMe}_2]_3$ and an evaluation of this compound in the thermal CVD deposition of indium oxide thin films. The precursor's suitability for use in gas-phase deposition was evaluated using bench top melting point determination, thermogravimetric analysis (TGA), differential scanning calorimetry (DSC), and NMR thermolysis studies. Films were analyzed by ellipsometry, IR and UV-Vis spectroscopy, x-ray diffraction (XRD), scanning electron microscopy (SEM), energy-dispersive x-ray spectroscopy (EDS) and x-ray photoelectron spectroscopy (XPS). To our knowledge, this is the first time an indium guanidinate species has been used for CVD.

Silver and Gold CVD

Previously, silver CVD has been achieved with several inorganic and organometallic species, including carboxylates, fluorocarboxylates and their phosphine adducts, AgF, and fluorinated β -diketonates, to name a few.²⁵⁻²⁷ A wide range of process temperatures have been reported, from 80°C to 600°C. Thermal CVD of gold has been performed with alkyl(phosphine)gold(I) compounds, (acetyl-acetonato)dimethylgold(III), MeAuP(OMe)₂Me and MeAuP(OMe)₂Bu, substituted dithiophosphate dimethylgold(III), fluorinated β -diketonates, as well as pivalate, oxyquinolate, mercaptoquinolate, and diethyldithiocarbamate compounds at temperatures ranging from 150 °C to 300 °C.²⁸⁻³⁰ There are a vast number of applications for thin gold and silver films, as well as for nanoparticulate coatings. In addition to traditional uses such as simple electronic interconnects and catalytic nanoparticles,^{31,32} some of the more interesting applications include performance enhancement of photovoltaic devices,²⁷ metal-assisted silicon etching,³³⁻³⁵ surface-enhanced Raman spectroscopy,^{36,37} and applications involving surface plasmons.^{38,39} Many applications stem from the non-linear optical effects of the metal nanoparticles.

Of particular relevance to much of the research presented below is the set of precursors that incorporate amidinate and guanidinate ligands. An amidinate ALD precursor is employed in Chapters 2 and 3 to deposit alumina films, in Chapter 5 a tris-guanidinate indium precursor is employed to deposit indium oxide, and the silver and

gold precursors described in Chapter 6 consist of a related ligand, an iminopyrrolidinate. This last ligand is related to the two partly due to structural similarity but also because it was designed specifically to address the undesirable decomposition pathways exhibited by amidinate and guanidinate compounds, first characterized using a copper compound.⁴⁰ Two specific pathways common to both amidinate and guanidinate precursors were eliminated by the iminopyrrolidinate structure: *beta-hydrogen abstraction* and *carbodiimide de-insertion* (Figure 1.2). The synthesis of the single-source iminopyrrolidinate ligands used in this work has been reported by our group previously.⁴¹ Increased thermal stability and improved deposition has since been observed for silver and gold iminopyrrolidinate, described in Chapter 6, as neither decomposition pathway is possible in the iminopyrrolidinate compounds (Figure 1.3).

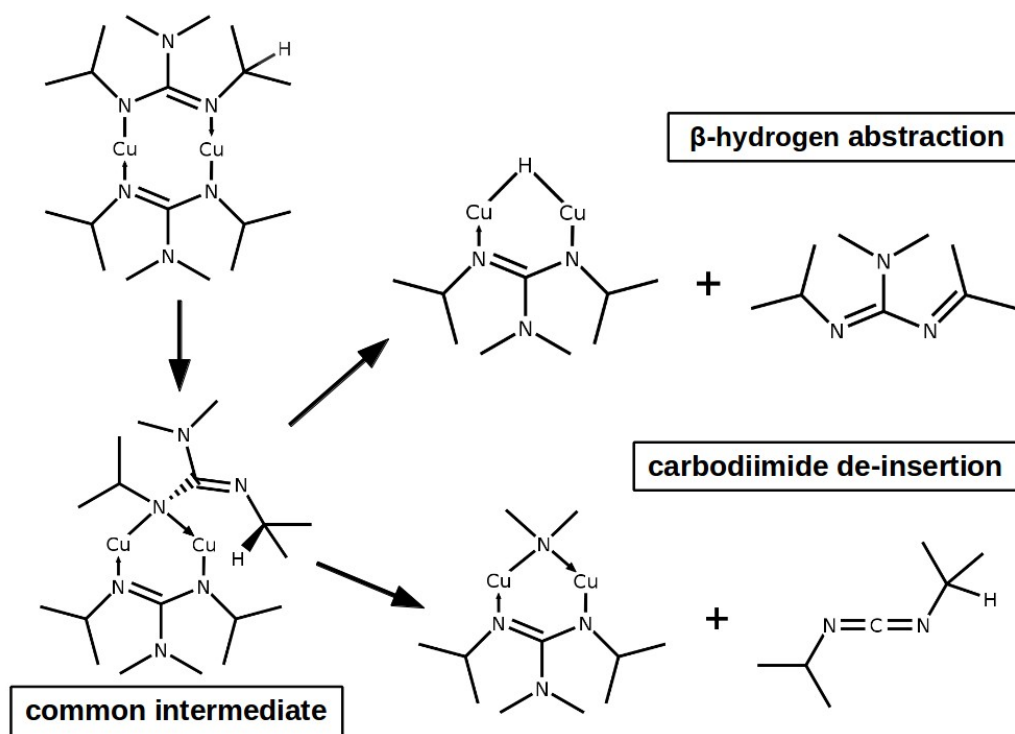


Figure 1.2 Thermal decomposition routes available to copper guanidates (analogous routes available to amidinates).

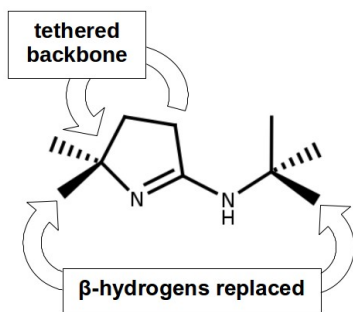


Figure 1.3 2,2-diethyl-tertbutyl-iminopyrrolidine described and studied in Chapter 6, highlighting features that prevent decomposition routes observed for amidinate and guanidinate analogs

Chapter 6 presents work on the synthesis of silver and gold iminopyrrolidinate precursors and an evaluation of these compounds as single-source precursors in the

thermal CVD deposition of metallic silver and gold thin films. The precursors' suitability for use in gas-phase deposition was evaluated using thermogravimetric analysis (TGA), differential scanning calorimetry (DSC), and NMR thermolysis studies. Depositions were performed with and without nitrogen flow to study mass transport dynamics. Films were analyzed by ellipsometry, XRD, SEM, EDS and XPS. To our knowledge, this is the first time silver and gold iminopyrrolidinate species have been used for CVD.

Atomic Layer Deposition

Atomic layer deposition, while similar, is significantly different from CVD in terms of how the film growth proceeds throughout the deposition. ALD is a gas-phase stepwise thin film deposition method that results in highly conformal coverage of complex surfaces.⁴² Where chemical vapour deposition is a continuous deposition process, ALD is distinguished by the self-limiting nature of the molecular monolayer formed at each step. Otherwise the requirements for precursor design are identical: high volatility, gas phase stability and high reactivity at the substrate. The simplest ALD process sees the first precursor, often but not necessarily a metal-organic species, entrained into a thermally-defined deposition zone and over the target substrate. By design, this precursor saturates the surface with chemisorbed species that render the surface inert, preventing further film growth (this is the crux of the difference from a CVD process, which would continue chemisorbing species for as long as they are entrained over the surface). A pulse of inert gas followed by evacuation of the deposition chamber (a “purge” pulse) eliminates excess

precursor and the products of the chemisorption reaction. This prepares the system for the next precursor which when entrained over the substrate reacts with the previous monolayer to form another self-limiting monolayer. Another pulse/purge step follows and the process is repeated until the desired film thickness is reached. Of course the term “monolayer” is a misnomer; often a more accurate description of the morphology would be that of a nanoparticulate (common with metal depositions) or partial coating which then knits together over subsequent cycles. Growth rates are calculated simply by dividing the final film thickness by the number of cycles, providing an average growth rate.

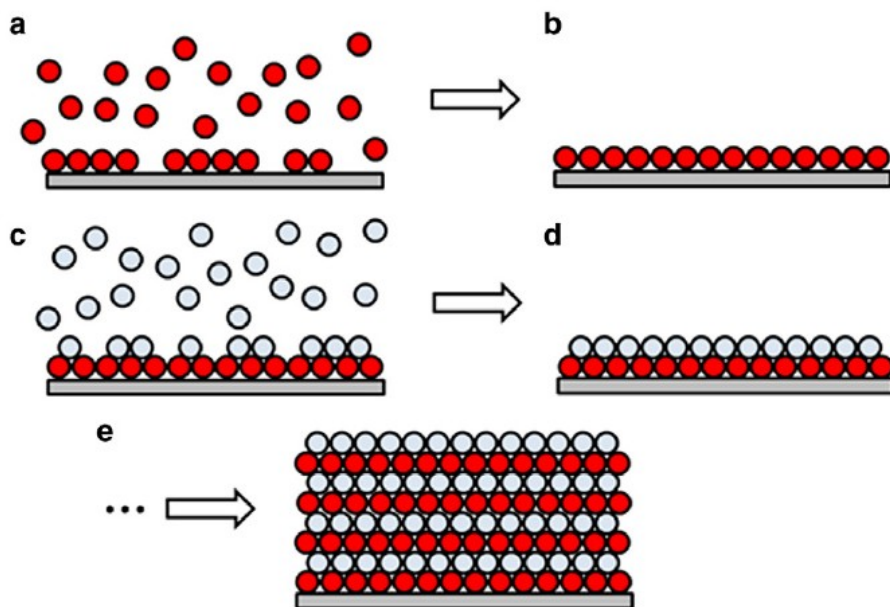


Figure 1.4 Schematic of the ALD process: a) the first precursor is introduced and a monolayer is formed; b) an N_2 purge and evacuation removes remaining precursor and volatile side products; c) the second precursor is introduced and reacts with the first monolayer, forming the first monolayer of the target film; d) another N_2 purge and evacuation removes remaining precursor and volatile side products. e) The process is repeated until the desired thickness is reached.

The ALD process was originally developed for electroluminescent displays,⁴³ and has seen a renaissance recently due to its usefulness in microelectronic fabrication.^{44–46} The technique is becoming very widespread, with applications in optoelectronic fabrication,^{47,48} MEMS fabrication,^{49–51} wear-resistant coatings^{52,53} and catalysis,^{54,55} to name only a few applications. ALD thin films are also useful for protective and cosmetic purposes. Precise control of film thickness, density, and composition leads to precise control of the films’ optical properties, including colour and appearance, described in detail in the following section.

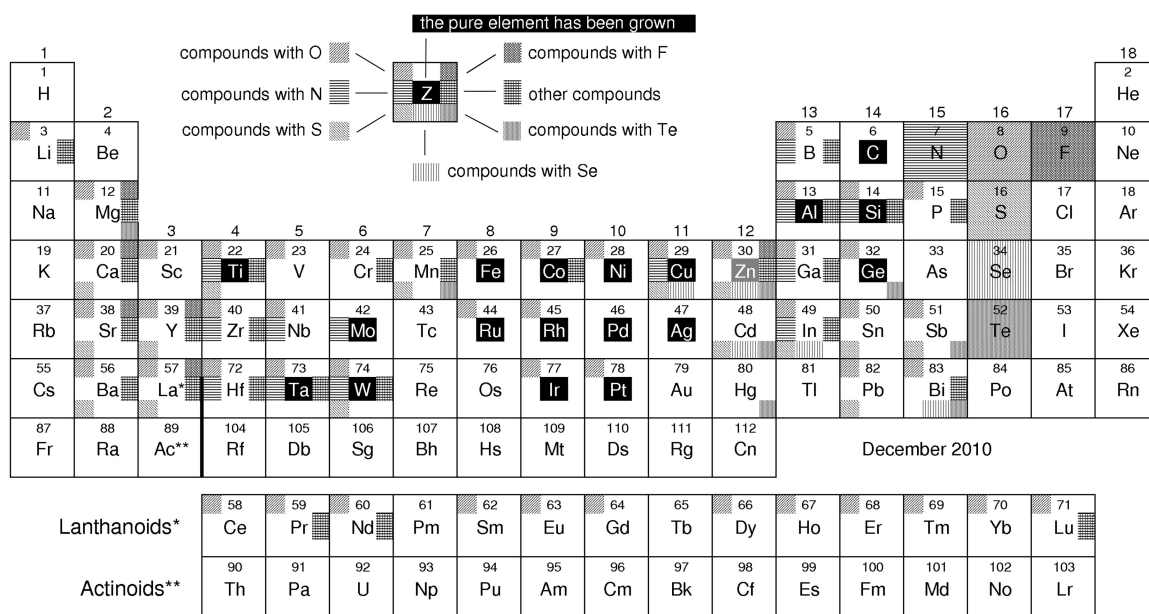


Figure 1.5 Table summarizing materials grown by ALD. Reprinted with permission from American Institute of Physics.¹²⁴ Copyright 2013, AIP Publishing LLC.

For a given set of precursors there will be an optimal substrate temperature range within which ALD-type growth is constrained. This “ALD window” is the temperature range where film growth is self-limiting, allowing for film growth that occurs by step-

wise reaction with a second precursor. The window is observed somewhere between the volatilisation temperature and decomposition temperature of the precursor. At temperatures below the window, film growth simply does not occur either because the precursor is not volatile or it is unreactive with the substrate. At higher temperatures, CVD-type growth that is not self-limiting is often observed. While film growth rates may remain constant within the window, there are many reports in the literature of processes where growth rates vary with temperature. Often the growth rates will increase with increasing temperature, but the defining feature of ALD growth remains: step-wise and self-limiting growth for a given temperature. Commonly, a precursor is limited to use in CVD when the volatilisation temperature and decomposition temperature of the precursor are not adequately separated.

1.2 ALD for Protective and Cosmetic Coatings

Protective Coatings

We investigated coatings offering two types of protection: protection from chemical attack and protection from mechanical wear. The relatively small concentrations of sulphides in the atmosphere is enough to tarnish otherwise untouched silver metal over time, and metals that are subjected to more regular use such as tools or coins will at a minimum be exposed to salt, sweat and oils in addition to airborne contaminants. A protective coating must resist these chemical attacks as well as physical wear; a hard but brittle coating that is highly resistant to chemical attack can nevertheless develop cracks,

admitting access to and corrosion of the underlying substrate. Resilience towards physical attack requires a combination of toughness and flexibility. Cosmetic coatings present their own, related set of challenges. If a specific colour of coating is desired (including colourless), for example, the material must remain visually unchanged should contaminants be absorbed. Additionally the coating must slow or prevent the contaminants' diffusion towards contact with the substrate interface, to preclude any chemical reactions that may alter the appearance of the substrate material or compromise the adhesion of the film (such as the oxidation of metal substrates).

Conformal, complete coatings using a minimal thickness of material have generated recent interest in ALD coatings as barriers to corrosion and mechanical wear. The literature provides numerous examples of efforts to protect a wide variety of materials including plastics for use in space,⁵⁶ wood,⁵⁷ and metals in diverse applications such as silver museum pieces,⁵⁸ ball bearings⁵⁹ and brain implants.⁶⁰ Most commonly the films are deposited using well studied processes such as aluminum oxide or titanium oxide, but other more exotic depositions have also been studied such as WS₂, W/Al₂O₃ and ZnO/ZrO₂ laminates, and melt-compounded titanium dioxide nanocomposites.^{59,61,52,62} Multilayer or laminate architectures have been found to impart increased wear resistance to a coating.⁵² In part this is due to the frustration of crack propagation: a single-material coating is more likely to crack all the way through to the substrate, thus exposing the substrate to direct chemical attack. More generally, multiple

layers provide alternative pathways for the release of mechanical stress, reducing the likelihood of the formation of a crack that leads directly to the surface.

Cosmetic Effects of Films: Interference Colours

The colours that result from thin film depositions are a complication that have not garnered much attention in the literature thus far. For most protective coatings, such as tools and ball bearings, the resulting colour is not a concern and the focus is on durability. For cosmetic applications the resulting colour is of equal if not primary concern. The colours exhibited by thin film coatings emerge from the phenomena of constructive and destructive interference of light; these so-called “interference colours” are very well understood. Consider a thin film of material on a substrate: a thin film that is necessarily transparent to some degree, with an index of refraction different from that of the substrate (Figure 2.1). Light may be reflected and/or refracted multiple times at each of the interfaces encountered (air/film and film/substrate). The light observed by the eye will therefore have constructively or destructively interfered with itself, as the process ultimately results in reflections that can range from weak to strong depending on the light's wavelength, the film thickness, the angle of incidence, and the physical constants of the materials involved. A thin film illuminated with a beam of visible light of multiple wavelength components will therefore produce a reflection that can be strong at some wavelengths and weak at others, observed as a shift in the spectrum of the reflected beam and therefore a shift in the perceived colour. For a given film/substrate pair, then, the

source of light will also contribute to the final result: sunlight will yield a different perceived colour than fluorescent light, for example. Iridescence arises from the angular dependence of phase change of the light, which is observed as the viewing angle deviates from normal to the surface.

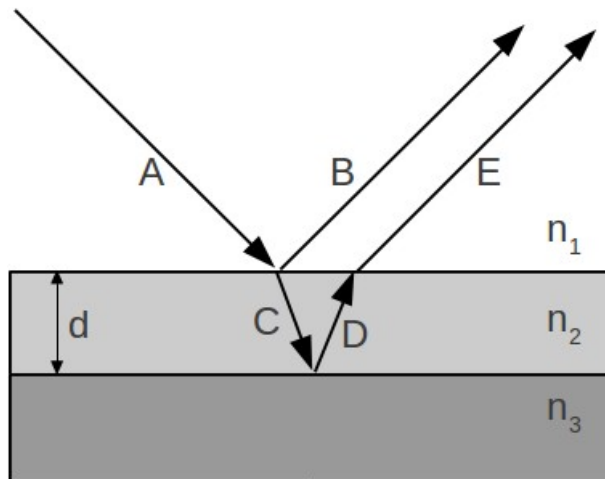


Figure 1.6 Model illustrating the origin of interference colours. **A** is an incident beam of light at a specific frequency. Due to partial reflection, it splits into beam **C** and **B**. Depending upon the thickness of the film (**d**) and the angle of incidence of **A**, the path length **C+D** may alter the phase of **E** with respect to **B**. Constructive or destructive interference may then occur, altering the wavelength of the outgoing light. The refractive indices of the materials are given by n_1 , n_2 and n_3 .

Interference colours are strongest when the interfaces are at distances comparable to, or smaller than, the light's coherence length (the distance over which the light wave can be considered to be a single sinusoid) which for ordinary white light is on the order of a few micrometers.⁶³ These thicknesses are exactly where the precision and control of an ALD process excels and furthermore multilayer structures are trivial, providing a high degree of versatility and tunability for optical and cosmetic applications.

While interference colours for the films can be modelled to some extent, the pertinent details of the actual physical system differ significantly from idealized models and thus merit direct observation. For example the dispersion curve (the wavelength-dependent index of refraction) for a bulk material may differ significantly from that of a thin film of the same material due to the manner in which the film was grown. Annealing under various gasses may further alter optical properties. Additionally, with respect to cosmetic applications (which may be subject to a range of lighting and observation environments) the perceived colour of the coated material may differ in subtle but significant ways from the measured wavelengths. Furthermore, as the angle of incidence will alter the path length of light through a given film, different viewing angles often result in different perceived colours (iridescence). These subtleties can have a direct impact on the choices made for cosmetic coatings. The CIE Lab “colour space” formalism for describing perceived colour is illustrated in (Figure 1.7). A difference of one unit along any of the axes roughly corresponds to a difference in colour distinguishable by the human eye-brain system.

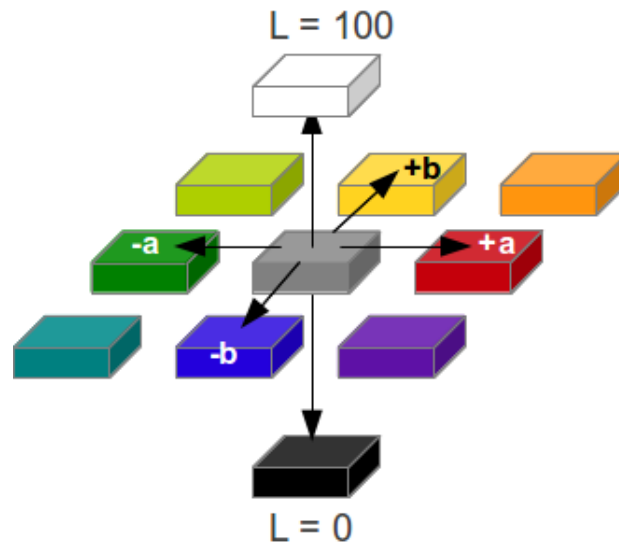


Figure 1.7: Representation of the CIELab coordinate system for describing colour.

Goniospectrometry is a technique used to measure the angular distribution of perceived colour scattered from a surface (gonio = angular). Previous goniospectrometric analysis of thin films is extremely rare. Lamminpää et al. extracted the optical parameters of SiO₂ thin-film coatings based on reflectance and transmittance but do not consider physiological colours as such.⁶⁴ Diamanti et al. characterized the colours of different titanium oxide films using spectrophotometry, but do not address angular dependency.⁶⁵ Beck et al. compared goniospectrometry with spectroscopic ellipsometry for the evaluation of the optical properties and colours of decorative coatings of Ti, TiN, TiCN, TiCN and TiAlCN.⁶⁶ Niyomsoan et al. investigated the colour variation in 0.5µm zirconium and titanium nitride decorative thin films with respect to the atomic ratio between nitrogen and the metals with oxygen as a contaminant.⁶⁷

Chapter 2 presents preliminary research into the colours produced by alumina and titania deposited by ALD on copper alloys in small scale and large scale batches. Protection from chemical attack and uniformity over large batches is also addressed. Chapter 3 reports detailed goniocolourimetric analysis of alumina deposited by ALD on silicon slides, comparing simulated spectra with observed spectra collected over a wide range of observation angles. Deviations from the predicted observations are discussed.

1.3 Photovoltaic Devices

Photovoltaic devices exploit the photovoltaic effect to generate a useful electric current from light. When light of the proper frequency impinges upon a material, electrons in the valence band of the material can be excited to the conduction band. With the proper architecture a device consisting of two materials can be created that then separates these electrons from the resulting positively charged “holes” they leave behind, guiding their flow in a manner that generates a useful electromotive force. The first such practical device, achieving 6% efficiency, was created in 1954 at Bell Laboratories by Daryl Chapin, Calvin Souther Fuller and Gerald Pearson, using a silicon p–n junction.⁶⁸ The basic architecture of this device is still in use today due to its simplicity and effectiveness. A p-n junction is a physical interface between two materials, one that is electron-rich (n-material) and one that is electron-poor (p-material). The composition of these materials may be entirely different, or they may each consist primarily of the same bulk material treated in such a way (e.g. doped with another element) as to make one

electron-rich and one electron-deficient. The materials are chosen such that the energy gap (the band-gap) between the valence band of the n-material and the conduction band of the p-material is on the order of the energy provided by the visible light spectrum. When an electrically conductive connection is made between the two materials and light of the appropriate frequency is absorbed, a direct current is generated as the resulting electron-hole pair are attracted towards one another through the conductor.⁶⁹ The materials used and exact architecture vary considerably.

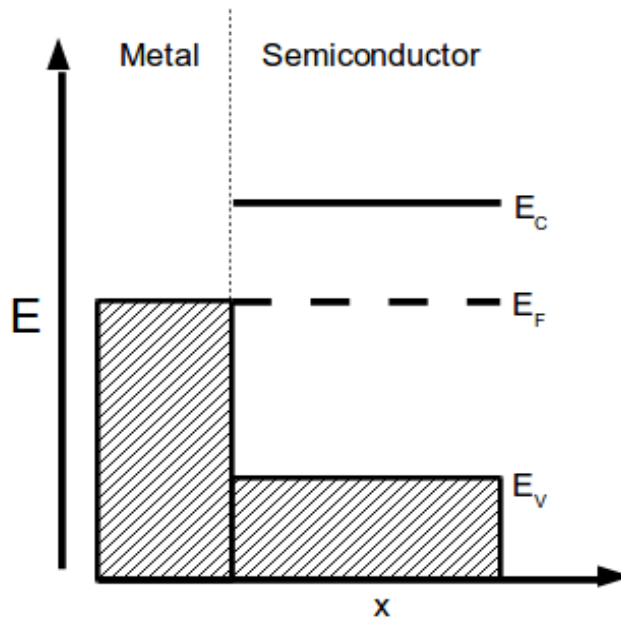


Figure 1.8: Band structure diagram for a Schottky barrier diode. E_C is the conduction band, E_F the Fermi level, and E_V the valence band.

Metal-semiconductor junctions are similar in form and function to p-n junctions, which are an interface between a p-doped and n-doped semiconductor. When a metal of the right work function is brought in contact with a semiconductor, charge carriers flow

across the junction until a thermal equilibrium is established, much like a p-n junction. This particular arrangement is called a Schottky-barrier diode (Figure 1.8). A Schottky barrier is simply a potential energy barrier for electrons formed at a metal–semiconductor junction. While these devices can act as solar cells, their photovoltaic conversion efficiencies can be considerably increased by the presence of a thin interfacial insulating layer (often an oxide) between the metal and the semiconductor. In a metal-SiO₂-Si structure for example, the insulating SiO₂ layer must be extremely thin for optimal performance: on the order of 10 Å.⁷⁰ This architecture is called a metal-insulator-semiconductor (MIS) structure. They received a great deal of attention in the 1970's and 1980's due to their relative economical advantage over the conventional p-n junction solar cells. The reflectivity and poor light transmission properties of the top metal layer limits the practical efficiencies of such cells, however.⁷¹⁻⁷⁴ Nonetheless structures with efficiencies of 10% - 15% have been demonstrated with theoretical efficiencies for flat Si based cells reaching up to 20%.^{75,71} To eliminate the problem of highly reflective metal layers, these have been replaced with transparent conductive oxides, yielding device efficiencies of 11.5% for spray deposited indium-tin-oxide (ITO).⁷⁴ Unfortunately, this improvement also results in increased device cost as ITO remains a relatively expensive material. This has motivated research into low-cost transparent conductor alternatives that may be compatible with this architecture, such as poly(3,4-ethylenedioxythiophene) poly(styrenesulfonate) (PEDOT:PSS).⁷⁶

In Chapter 4 photovoltaic devices using the MIS architecture are assembled wherein the “metal” is spin-coated PEDOT:PSS, the insulating layer is aluminum oxide deposited by ALD, and the semiconductor is n-type silicon. The performance of flat and nanostructured silicon are compared and the nanostructured silicon substrate is found to generate a superior photovoltaic response.

Chapter 2 - Protective and Cosmetic Coatings for Coinage Metals and Their

Alloys

The work presented here is unpublished. It was performed in collaboration with the Royal Canadian Mint. Co-contributors to this work include Agnieszka Kurek, Adam Wells and Seán T. Barry.

2.1 Abstract

Stamped coins of brass and bronze were coated by ALD with alumina and titania. These coatings were evaluated for use as protective and cosmetic coatings for circulation and numismatic coinage. Initial alumina ALD experiments establishing proof of concept on individual coins were performed, assessing feasibility and film continuity. These were followed by scaled-up depositions on 2744 coins per batch where optimization of deposition parameters for uniform coatings both on individual coins and across a batch for alumina and titania films was performed. The effect of film thickness on colour was examined and preliminary investigations of protective properties undertaken. The process was optimized to minimize batch times, emulating an industrial setting. It was found that high-quality, uniform coatings could be achieved with “multi-pulse” programs, yielding coins indistinguishable by eye or touch from uncoated coins.

2.2 Introduction

Protecting bulk metals (mainly of Fe, Al, Cu, Zn, Mg and their alloys) from corrosion has been a problem for centuries and remains a major ongoing concern in modern times.

A large number of coatings for corrosion inhibition have been developed where the

principle issue is oxidation and subsequent corrosion in air, with other considerations dependent on the application, including mechanical wear, moisture, and specific chemical concerns (salts, H₂S, CO₂, etc). Applications of significant concern in the literature include corrosion inhibition in water cooling systems, in the oil and gas and electronics industries, and generally inhibition of corrosion in industry due to acids.⁷⁷

Recently, interesting work in this area includes polymer layers, silica-organic layers, conversion layers, metallic layers and ceramic layers deposited by a wide variety of methods to form self-healing anti-corrosion coatings.⁷⁸ Inorganic-organic sol-gel methods are widely used for thin ceramic coatings. Ceramic coatings are usually deposited on metals to improve their performance in high temperature and/or abrasive environments and have been shown to improve resistance against gas, solid, molten and condensed phase oxidation and corrosion; decreasing wear; decreasing heat losses and/or reflecting radiation in high temperature systems.^{79,80} Vapour-phase methods dominate the list of techniques for protective coatings, but electrochemical plating is common as well. The literature provides several examples of efforts to protect a wide variety of materials with ALD coatings including plastics, wood, museum pieces and ball bearings.⁵⁶⁻⁵⁹ Most commonly simple metal oxide films are used, but other more complex depositions using laminates have generated interest as multilayer or laminate architectures have been found to impart increased wear resistance to a coating.⁸¹

Research into protective coatings is primarily motivated by applications in industrial settings or microelectronics and nanotechnology. With the notable exception of a patent

application from Beneq Oy for an ALD process used to coat silver with a variety of transparent films (aluminum oxide, titanium oxide, chromium oxide, zirconium oxide, indium oxide, and niobium oxide),⁸² very little work has been done in the area discussed below, specifically: thin film protective coatings for legal tender that will see large scale, public use (coins). The particular concerns of this type of application are similar but distinct from industrial settings: the coatings must still protect against environmental factors such as human sweat and oils, atmospheric components and significant mechanical wear, but the substrates must continue to present a relatively unblemished and uniform appearance that does not deviate from the established, accepted appearance of the coins.

2.3 Results and Discussion

The feasibility of depositing alumina films on bronze Canadian dollar coins (minted 2009, 88% Cu, 12% Sn w/w, Figure 2.1) was initially assessed using a custom-built ALD tool (Figure 2.8) and a previously reported⁸³ acetamidinato alkyl aluminum compound (Figure 2.2). A series of thicknesses were deposited on coins using these precursors, ranging from 1000 Å to 10,000 Å. Silicon witness slides were included in each run for characterization and comparison. Table 2.1 shows the values obtained for each by ellipsometry.



Figure 2.1 An uncoated coin (**b**) is contrasted against a coin with a 1000 Å alumina coating (**a**) and a coin with a 1500 Å coating (**c**).

Target film thickness (Å)	1000	3000	8000	10000
Measured film on coin (Å)	1015	3273	7790	10173
Measured film on Si (Å)	1093	3243	7379	9135
Difference (%)	7	1	5	11

Table 2.1 Single-point thickness measurements of film thickness on bronze and silicon substrates as measured by ellipsometry. The last row indicates the percentage difference in observed values for the two substrates.

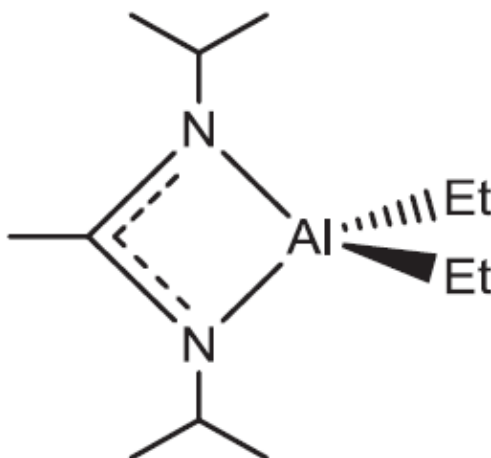


Figure 2.2 Acetamidinato alkyl aluminum precursor employed in this work

The coins were characterized by visual inspection (an important consideration for legal tender), by SEM and using a electrodeposition test to evaluate film continuity. Interference colours from the films altered the appearance of the coins, dramatically in some cases. Figure 2.1 demonstrates the sensitivity of the eye to seemingly minor differences in film thickness: 1000 Å and 1500 Å coatings produce clear changes in perceived colour. Coin cleanliness prior to deposition also had a pronounced impact on appearance. Any oils remaining on the coin, invisible prior to coating, are unmistakably highlighted by deposited films. This was mitigated by cleaning with soap and water, sonication in distilled water, ethanol and then ether, and finally by treating the coins to a 5% H₂ in N₂ purge for 30 min at 200 °C *in situ* immediately prior to deposition. Substrate cleanliness became a much more pressing issue once the project moved to batch deposition experiments with implications for integration into bulk production, discussed below. Thicker films resulted in a very interesting variety of colours, including iridescence. Figure 2.3 shows a selection of results along with silicon witness slides for comparison. As the interference colours produced are a function of the index of refraction of both the film and the substrates, the colours produced on the coins and on the silicon cannot be quantitatively compared. At a thickness of 3000 Å a pronounced iridescence was observed on the coins: at low viewing angles the coin appeared mostly violet and at high viewing angles (normal to the coin face) it appeared green (Figure 2.4).

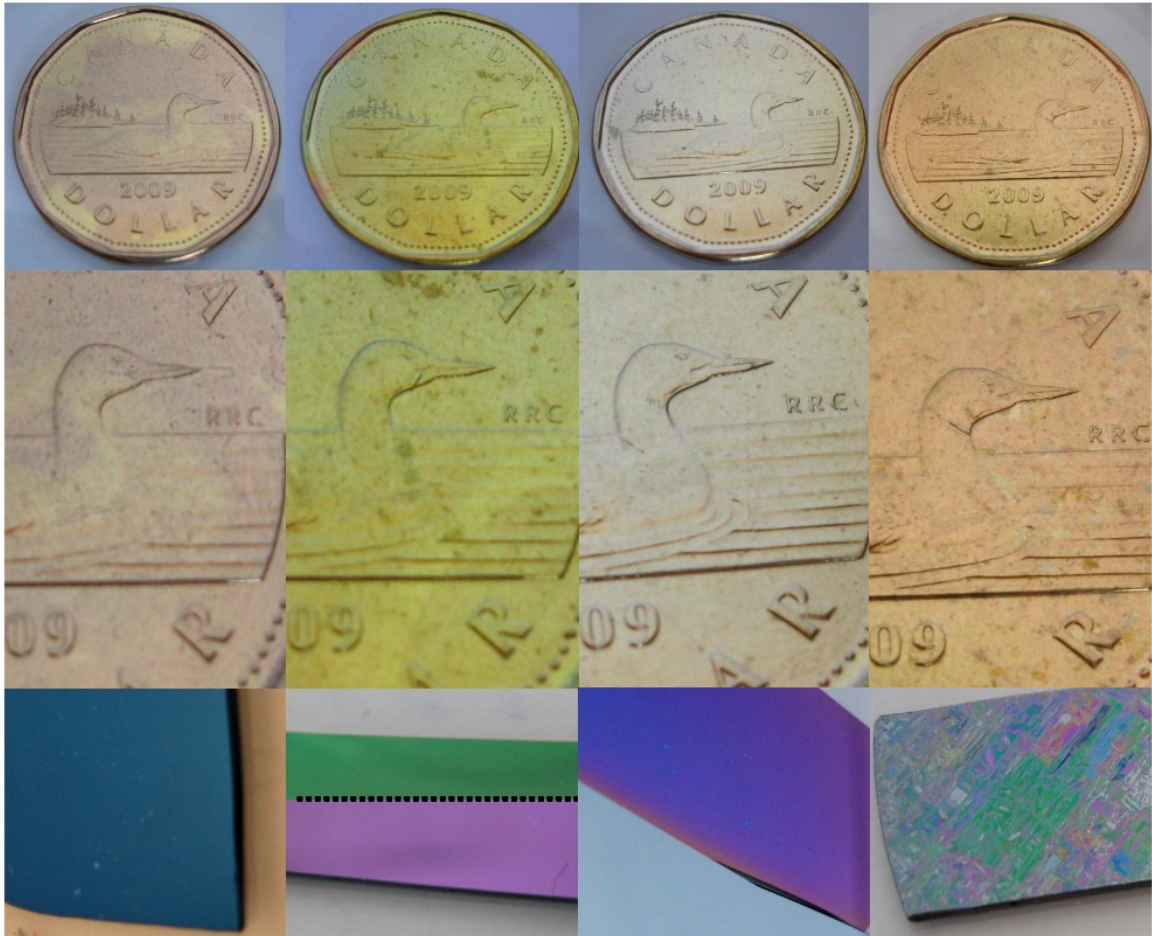


Figure 2.3 Deposition series showing coins in the top two rows and their respective silicon witness slides at the bottom. From left to right, each column presents coatings of 1000 Å, 3000Å, 8000 Å and 10,000 Å. The second witness slide is shown at two different viewing angles to demonstrate its iridescence, while the last slide exhibits delamination. Note that this delamination was observed to a much lesser degree on the coin.

Film adhesion on bronze began to degrade for film thicknesses above 6000 Å, becoming much more pronounced for the 10,000 Å sample (Figure 2.3). Interestingly, film adhesion on bronze was much better than it was on silicon. This was surprising as it was anticipated that the metal substrates would present poor adhesion, particularly given their non-pristine nature. It had been assumed that the thin silicon oxide interfacial layer

which is unavoidable in alumina depositions on silicon would provide a strongly binding intermediate layer between the silicon substrate and the Al_2O_3 film but the delamination of the 10,000 Å film from the silicon was nearly complete, while the same film on the coin showed only moderate delamination. It is well known that strain can originate from growth on lattice-mismatched substrates and from post-growth cooling.⁸⁴ The nature and composition of the interface between the bronze substrate and alumina film is not known and bears closer scrutiny.



Figure 2.4 Iridescence of 3000 Å film of Al_2O_3 on bronze.

For the coatings to act as a barrier to tarnishing, they must be conformal. The conformality of the coatings was assessed by electrochemical deposition of copper from aqueous solution, followed by examination by SEM. Defects in the film (either holes or extremely thin films) that allowed electrical contact with the solution became conspicuous due to the growth of copper metal on the surface. An uncoated coin exhibited complete coverage by electrodeposited copper metal, as expected. A coin with a

1000 Å coating subjected to the test was found to have only a few sites where copper growth was observed by SEM, shown in Figure 2.5. This was an encouraging result given the non-ideal nature of the substrates.

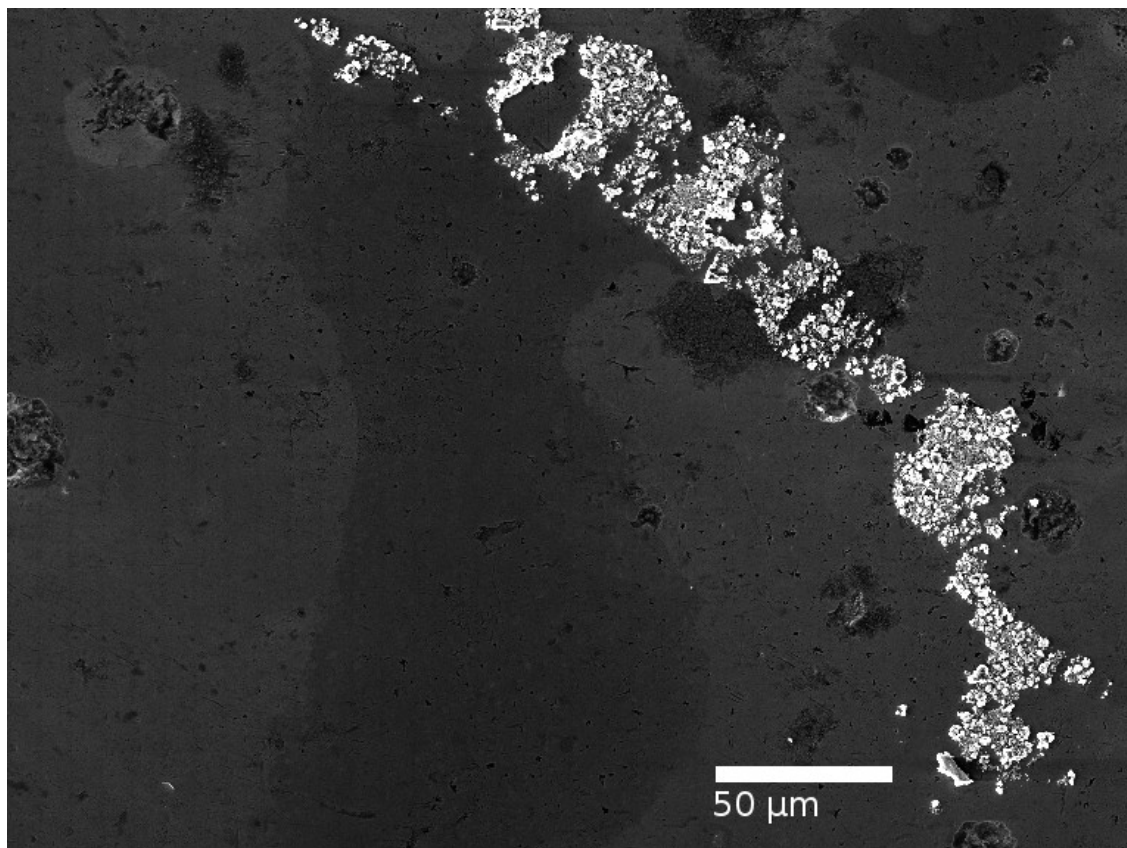


Figure 2.5 SEM image of a coin coated with 1000 Å Al_2O_3 , after electrodeposition experiment. Copper metal (white) indicates a flaw in the film exposing the coin to the electrodeposition solution.

Batch Depositions

The results from these initial depositions on the custom-built reactor led to larger scale, “bulk” depositions of alumina and titania using a Picosun SUNALE P-300B tool. “Tokens” were used in place of legal tender and provided by the Mint; these had the same

dimensions, composition and processing as circulation coins used in previous testing with the exception that they were stamped with a different image. A set of racks were machined to hold the tokens parallel to system flow in a stacked configuration (Figure 2.9). A total of 2744 tokens could be loaded in this manner. The precursor chemistry was changed to adapt to batch depositions as well; the well-known trimethyl aluminum(TMA)/water precursor pair was used for aluminum oxide and a titanium tetraisopropoxide/water pair was used for titanium oxide. Both of these new precursors could be obtained commercially in large quantities at reasonable cost.

There was some concern that points of contact between the tokens and the racks could lead to defects in the films due to obstruction of precursor flow. Indeed, prior to the optimization of deposition parameters (specifically the thermal equilibration wait time prior to deposition) some film irregularities were localized at points of contact. The nonuniform growth observed near points of contact are attributed to a thermal gradient rather than to any irregularities of precursor flow. There was in fact an altered growth rate in these areas due to a thermal gradient as insufficient time had been allowed for the entire thermal mass to equilibrate. The deposition chamber is heated by external sets of resistively heated coils. As the deposition chamber was held under vacuum with no convection currents to assist heat distribution, the majority of heat transfer was achieved radiatively or by direct thermal contact of the internal components as the rack assembly was directly affixed to the chamber ceiling. Those parts of the tokens in direct contact with the racks were therefore warmer, leading to an altered film growth rate as compared

to the areas further away from the points of contact. The resulting film thickness gradient was clearly observed by eye. The proper wait time for the system to reach thermal equilibrium was established with an array of thermocouples affixed to a fully-loaded bulk run, followed by verification with ALD deposition experiments. In this manner it was determined that a thermal equilibration time of 6 hours for a process temperature of 250 °C was necessary for uniform film growth across all substrates. This process temperature was chosen as it accommodated both the alumina and titania ALD processes, based on literature values for the precursors employed.^{85,86} A study of the effectiveness of nitrogen flow during the heating step to accelerate equilibration would be useful to reduce total process time, but was beyond the scope of this work.

An issue of interest that then became obvious was initially attributed to non-uniform coatings: a small number of individual tokens (approx. 0.6% of tokens) on an otherwise successful deposition would present a colour markedly different from the rest. Further testing with heating but without any precursor pulsing (essentially an anneal under vacuum) produced similar results; a similar number of individual, randomly located tokens would acquire an entirely uniform, slightly pink hue. This evidence and discussions with the Mint revealed that the observed colour change was due to a variation in the copper composition of the bronze coatings in these tokens, which can vary by as much as $\pm 5\%$. This is a known issue that is usually caught on the Mint production line by visual inspection but our tokens were obtained prior to this step. The difference in colour is subtle on the production line and was considerably enhanced by the thermal anneal

imposed by the ALD experiments. The colour change under anneal may be due to preferential migration of the tin towards the surface but this was not verified or studied further.

Tokens were provided by the Mint directly after stamping. This proved problematic initially as a colourless, transparent oil (composition not divulged by the Mint) is used in the stamping process that both aided the stamping process and protected coins and tokens from tarnishing during subsequent transport. This oil interfered with the ALD process, often causing a cloudiness in the coatings that was typically minimal but occasionally noticeable on casual inspection. The solvent-based cleaning regimen used for individual coins described earlier was not practical for batch depositions. To resolve the issue the Mint began pre-treating the tokens with an anneal at 500 °C under hydrogen gas (exact experimental details not divulged). To streamline this process for production, it was proposed that this “hydrogen scrub” be performed in the ALD tool immediately prior to deposition but this experiment is beyond the scope of the work described here.

Initial bulk ALD experiments employed standard, single pulse programs. These proved inadequate for complete and uniform coatings. Replacing a single, long pulse with a pulse program that used multiple pulses of the same precursor separated by short purges resulted in uniform coverage. Long purges were still required between precursors. The brief pauses to purge between each small pulse allowed the bubbler vapour pressure to rise somewhat and so deliver a larger total precursor mass than a single pulse of equivalent length could generate. Table 2.2 describes the pulse program timing in detail.

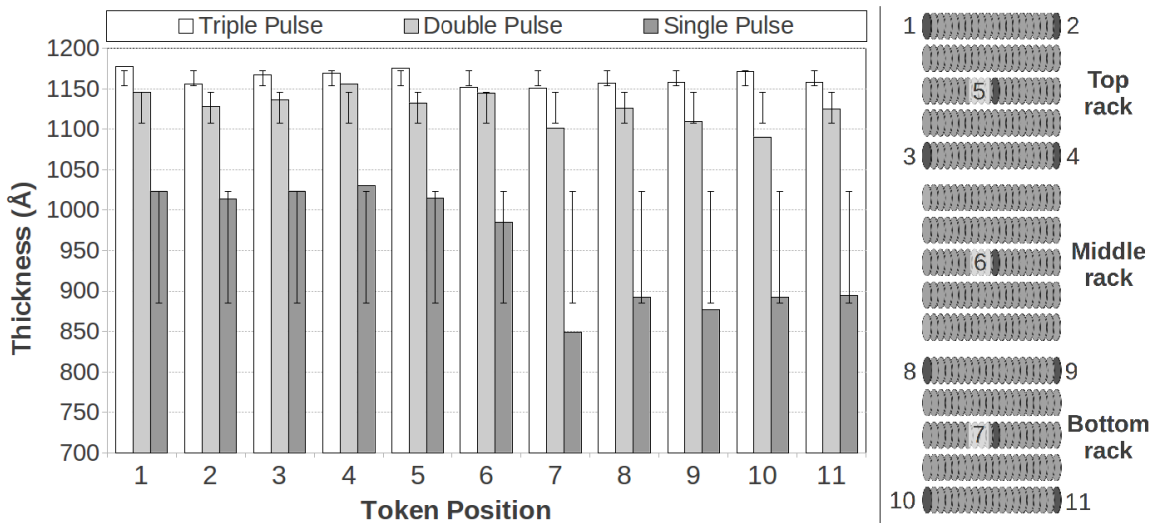


Figure 2.6 Thickness results for three pulse programs, revealing uniformity throughout the volume of a single batch run. Error bars depict standard deviations (evaluated across all eleven samples) of 72 Å, 20 Å and 10 Å for the single, double and triple pulse program thickness measurements respectively. Image at right depicts the placement of witness slides used for ellipsometric thickness measurements. Racks without witnesses are not shown but were present and fully loaded.

To quickly and efficiently evaluate thicknesses and uniformity, silicon witness slides were again used. In the bulk experiments, these were placed at the four corners of the top and bottom racks, with three more slides placed in the centre of the top, centre, and bottom racks for a total of eleven slides (Figure 2.6). This distribution allowed for straightforward monitoring of batch-wide film uniformity. The slides were preferred for analysis because they were more amenable to ellipsometry than the tokens: ellipsometry is straightforward on flat silicon but the various three-dimensional features of a stamped coin made reliable results elusive. This was deemed acceptable since the work prior to batch reactor scale-up indicated that the growth rates for films of the target thicknesses were known to be nearly identical regardless of substrate (Table 2.1). Regardless,

attempts were made to obtain flat tokens from the Mint but this proved problematic due to the nature of the stamping process. Silicon was also preferred for analysis as removing tokens and coins from the Mint premises was not straightforward due to required security procedures.

Three pulse program types were evaluated: a single pulse, double pulse, and triple pulse sequence. In each case, both precursors employed the same number of sub-pulses, and each sub-pulse was the same duration (0.1 seconds). Between sub-pulses of the same precursor, 0.5 seconds was used. It was clear from the data in Figure 2.6 that single and double pulses produced nonuniform films that showed a characteristic depletion pattern in the direction of flow. As this could be simply attributed to the fact that a larger dose is delivered with an increasing number of pulses, thus improving coverage, an experiment was performed using single 0.3 s pulses. It was found that the uniformity of the triple-pulse program remained superior. These results are attributed to the increased demand for precursor due to the large total surface area of the substrates, and the diminishing returns of vapour pressure as a precursor bubbler is held open. A single 0.1 second pulse, or a 0.3 second pulse simply did not deliver enough precursor to form a monolayer on every available surface. It is reasonable to assume that an even longer single precursor pulse would ultimately achieve this saturation, but this would add to process time (unacceptable in an industrial setting) and confer no advantage over the multi-pulse approach with respect to film properties.

For the triple pulse formulation, purge times *between* precursors were also optimized to minimize total process time and maximize uniformity. A set of experiments evaluated purge times of 5, 7.5 and 10 seconds for 1200-cycle depositions of alumina. Thickness measurements yielded standard deviations of 39, 19 and 10 Å respectively clearly indicating a purge of at least 10 seconds is required for maximum uniformity. Additionally, shorter purge times resulted in thicker films, further indicating some CVD growth taking place due to incomplete removal of co-reactants. Partly by trial and error and partly through simulations with colourimetric simulation software (discussed in detail in Chapter 3) it was found that alumina coatings on brass and bronze in a narrow range around 1200 Å yielded tokens that were indistinguishable from uncoated tokens. TiO₂ depositions were also tuned in this manner.

A small series of experiments depositing titania from titanium (IV) tetraisopropoxide and water were also performed. In an initial experiment, coincident depositions of a nominally 50 Å film of TiO₂ on both a previously uncoated token and a token previously coated with approximately 1200 Å Al₂O₃ were performed. XPS analysis was performed to characterize the films. The results indicated poor growth on the bare tokens; titanium is detected but the strength of the signal and the baseline of the data trace suggests a rough, incomplete film. However, excellent growth of titania on alumina films was inferred as no significant aluminum signal was detected by the instrument. This provides qualitative evidence for the expected TiO₂ film thickness of 50 Å, as this thickness exceeds the penetration depth of the XPS x-rays thus rendering the alumina layer inaccessible to the

technique. Ellipsometric analysis of the film was attempted but the instrument was not sensitive enough to deconvolute the two coatings. With this encouraging preliminary data a series of laminate structures were generated, always using alumina as a base layer. The characterization of these is beyond the scope of the present work.

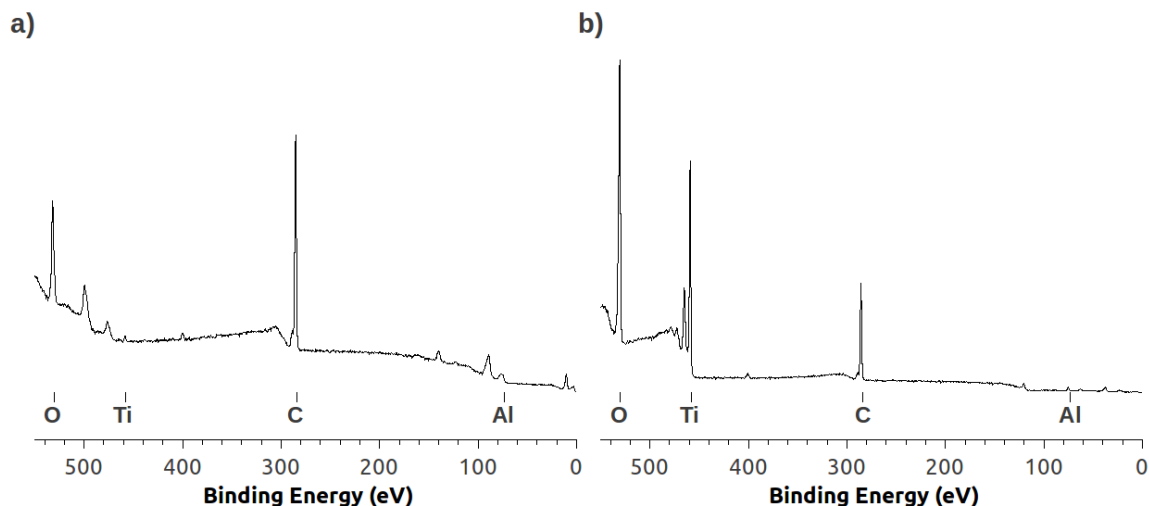


Figure 2.7 XPS spectra of a bare token exposed to a TiO₂ ALD process (**a**) and a token with a 1200 Å Al₂O₃ coating exposed to the same TiO₂ ALD process (**b**). The shape of the baseline in **a** suggests a rough surface. Note that no aluminum oxide process was applied to sample **a**; the Al signal is marked there for comparison with **b**.

2.4 Experimental

Small Scale Depositions

Canadian Dollar Coins (minted 2009) were coated in these experiments, delivered in person by a Mint representative from the production line. They were 26.5 mm in diameter, 1.95 mm thick, composed of a nickel core and plated with bronze (approx. 88% Cu, 12% Sn w/w). Prior to deposition they were hand washed with soap and water, then

sonicated in distilled water, then ethanol, the ether and finally by treating the coins to a 5% H₂ in N₂ purge for 30 min at 200 °C *in situ* immediately prior to deposition. Silicon witness slides were included in ALD experiments to allow additional film characterizations that were difficult or impossible on the metal substrates. Silicon slides were sonicated in acetone, placed in piranha etch solution for 20 min, rinsed with distilled water and subjected to a UV-ozone treatment to ensure a clean oxide surface. UV irradiation (180–260 nm) photolyses molecular oxygen in air leading to formation of ozone, a very effective oxidizing agent. The oxidized products of any residual organic molecules on the substrate surface are volatile.

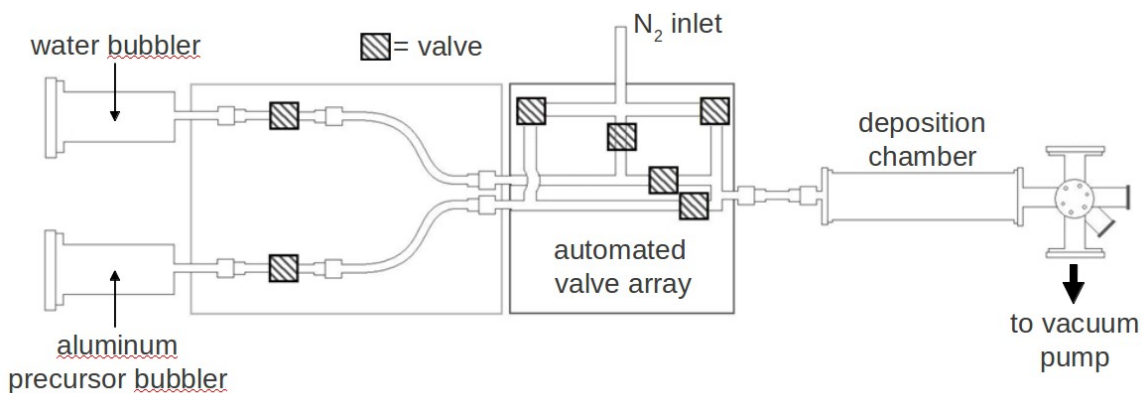


Figure 2.8 Custom-built ALD tool schematic.

Initial depositions on one to three coins per run were performed in a custom built ALD tool shown in Figure 2.8 using the acetamidinato alkyl aluminum precursor (AA) (Figure 2.1) and distilled water. The aluminum precursor bubbler was held at 50 °C and the valve array was maintained as a gradient from 80 °C to 140 °C; the furnace was held at 175 °C. Coins were allowed to rest directly on the furnace tube or were supported three at a time

by a custom built coin holder that had been passivated with at least 100 Å alumina prior to use. The pulse program employed was as follows: (1) 5.0 s purge with N₂, evacuate for 10.0 s; (2) 5.0 s fill aluminum precursor bubbler with N₂ carrier gas; (3) 5.0 s entrain aluminum precursor with carrier gas; (4) 5.0 s purge with N₂, evacuate for 10.0 s; (5) 5.0 s fill H₂O bubbler with N₂ carrier gas; and (6) 5.0 s entrain H₂O with carrier gas.

All small scale depositions began with 30 min of substrate passivation under 1.0 Torr of 5% H₂ in N₂ at process temperature to ensure a hydrogen-terminated metal surface.

Batch Depositions

Two types of so-called “tokens” were used in batch depositions as samples representative of Canadian Dollar Coins so as to avoid consuming large amounts of legal tender; brass and bronze-coated versions of the coins described above with roughly the same dimensions and composition. Brass is an alloy of copper and zinc (nominal composition not divulged). These tokens are commonly used at the Mint for process testing purposes. Initial bulk ALD experiments were conducted on “as-received” tokens directly from the Mint, which were delivered in vacuum-sealed packaging.

Batch depositions were performed at a process temperature of 250 °C on a Picosun SUNALE P-300B tool using TMA, titanium(IV) isopropoxide, and water. The pulse programs used for alumina and titania coatings are described in Table 2.2. It was found that longer pulses were necessary for each precursor for the titania coatings. Longer

purge times were used at the end of each half-cycle to ensure no vapour-phase reactions or CVD-type growth took place.

	M	purge	M	purge	M	purge	H ₂ O	purge	H ₂ O	purge	H ₂ O	purge
Al ₂ O ₃	0.1	0.5	0.1	0.5	0.1	10	0.1	0.5	0.1	0.5	0.1	10
TiO ₂	2.0	0.5	2.0	0.5	2.0	10	2.0	0.5	2.0	0.5	2.0	10

Table 2.2 Pulse program timing used in the bulk ALD experiments for alumina and titania coatings. Each row represents a single ALD cycle, yielding a monolayer of target material. The metal precursors are represented by "M" and all values are in seconds.



Figure 2.9 Empty coin racks (left) and filled, after deposition (right). Note the variation in interference colour on the coins and racks, clearly indicating non-uniform thickness.

Trimethyl aluminum (TMA), titanium (IV) isopropoxide (TTIP) and distilled water provided by Picosun were used as precursors. The TMA and water were held at room temperature and the TTIP was heated to 110 °C. Custom-built stainless steel racks were employed to support the coins during deposition (Figure 2.9).

Electrodeposition Testing for Film Continuity

An 80 mL solution of 1.0 M H₂SO₄ and 0.4 M CuSO₄ was prepared from 4.4 mL concentrated H₂SO₄ and 8 g of solid CuSO₄ dissolved in distilled water. A small section of a coin coated by ALD was abraded with sandpaper to expose a metallic area for electrical contact. The exposed area of the coin was affixed to an electrode and the coated portion of the coin was suspended in the solution. Another electrode was affixed to a copper gasket and likewise suspended in the solution. The electrodes were connected to a power supply, and a voltage of 0.5 V and a current of 0.08 A was supplied for 4 minutes. An identical arrangement was employed to evaluate uncoated coins for comparison.

Characterization

Al₂O₃ film thicknesses were determined by ellipsometry (Plasmos, HeNe laser at $\lambda = 632$ nm, $n_{\text{Si}} = 3.882$, $n_{\text{alumina}} = 1.76$, $n_{\text{Cu}} = 2.43$). Scanning electron microscopy was performed using a Tescan Vega-II XMU. X-ray Photoelectron Spectroscopy was performed using a Kratos Axis Ultra DLD instrument, with monochromated aluminum K α x-rays at 140W. A charge neutralizing electron floodgun was employed for insulating samples.

2.5 Conclusions

Aluminum oxide was deposited on individual bronze circulation coins with a previously reported process using an acetamidinato alkyl aluminum precursor and water. Ellipsometric characterization of the coins and silicon witness slides revealed that for deposited thicknesses on the order of 1000 – 10,000 Å, growth rates were independent of substrate. With microscopy and visual inspection it was found that the films adhered more strongly to the metal substrates than to the silicon at film thicknesses of 6000 Å and above. Aluminum oxide, titanium oxide, and laminate combinations of these materials were deposited on bulk quantities of brass and bronze tokens. It was determined that a pulse program with three subsets of precursor/purge pulses for each precursor was required for completely uniform coatings on all 2,744 tokens at 250 °C.

As uniformity of look and feel is important for legal tender, special attention was paid to the interference colours produced by the deposited films. A film of approximately 1200 Å was found to yield coins nearly indistinguishable from uncoated coins. While not necessarily desirable for introduction into circulation, other thicknesses produced an array of colours including iridescence that may prove useful for numismatic, limited edition coins. These optical properties also merit investigation as anti-counterfeiting measures. A study of the nature and composition of the interface layer between metal substrates and alumina film would help to understand both protective and cosmetic issues.

Chapter 3 - Goniocolorimetric Study of Aluminum Oxide Films Deposited by Atomic Layer Deposition

Modified from original manuscript, published as:

Gordon, P. G.; Baribeau, R.¹; Barry, S. T.²; "Goniocolorimetric Study of Aluminum Oxide Films Deposited by Atomic Layer Deposition", *Thin Solid Films*, **2012**, 520, 2943.

¹ Institute for National Measurement Standards, National Research Council Canada, 1200 Montreal Road, Ottawa, ON, K1A 0R6, Canada

² Department of Chemistry, Carleton University, Ottawa, ON, K1S 5B6, Canada

3.1 Abstract

The interference colours resulting from thin films of Al₂O₃ deposited by atomic layer deposition (ALD) on silicon have been rigorously analyzed using a newly developed robotic gonireflectometer. A series of eleven increasingly thick films were deposited, up to 1613 Å, and their reflectivity values obtained for the visible spectrum. A comparison of these values with the predictions of computer simulations employing Fresnel equations has revealed that while there was generally good agreement between predicted and measured spectra, there are some spectral regions that exhibit large deviations from predicted reflectivities, in particular at near-normal measurement angles and shorter wavelengths. The effect of these discrepancies on colour appearance was investigated in the CIE L*a*b* colour space for the daylight illuminant D65. Large iridescence is both predicted and measured for most film thicknesses. Chroma and hue differences as large as 20 CIELAB units between the predicted and the measured colour centers were obtained. Simulation also predicts larger iridescence than what is actually measured. A

likely cause for the observed discrepancies is that the dielectric constants of the ALD films deviate from the literature values for the bulk material.

3.2 Introduction

Herein we describe a rigorous analysis of the interference colours that arise from thin aluminum oxide films deposited on silicon substrates. The goniocolourimetric analysis in this work makes use of a gonireflectometer recently developed to measure the angular distribution of the light reflected by opaque materials.⁸⁷ The regular spectral reflectance of the sample is measured precisely over the visible range from 380 nm to 780 nm and for incidence angles varying from near normal to near grazing. International Commission on Illumination (CIE) lightness, chroma and hue values are calculated for a standard illuminant representative of daylight, and are plotted in CIELAB colour space to demonstrate the variation of colour with thickness and angle, and to compare with theoretical predictions. Simonot et al. have demonstrated a method for adapting the CIELAB space to goniocolourimetric measurements of glossy and iridescent objects.⁸⁸

The aluminum precursor employed for ALD film growth was $[\text{MeC}(\text{N}^i\text{Pr})_2]\text{AlEt}_2$ (Figure 3.1). This precursor and the deposition process employed in this work are described elsewhere.⁸³

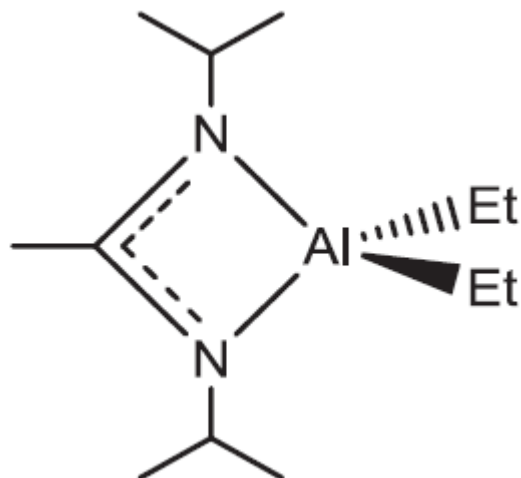


Figure 3.1 Acetamidinato alkyl aluminum precursor employed in this work.

3.3 Experimental

Substrate Preparation and Al₂O₃ Deposition

The alumina films were grown on mechanical grade n-doped Si(100) substrates. The silicon substrates were cleaned and prepared prior to the ALD experiments as follows: substrates were cleaned of surface contaminants and silicon dust by sonication in an acetone bath for 30 min and then rinsed with distilled water. They were then subjected to a chemical etch process to generate a clean silicon oxide surface, as follows: they were placed in a 10:10:1 ratio of H₂O:H₂SO₄:H₂O₂ for 30 minutes, then rinsed with distilled water, then sonicated for 10 minutes in distilled water. They were then placed in 4:1 ratio of H₂SO₄:H₂O₂ for 10 minutes, rinsed with distilled water, placed in 1:1:6 ratio of NH₄OH:H₂O₂:H₂O for 10 minutes, rinsed with distilled water, placed in 1:1:6 ratio of

HCl:H₂O₂:H₂O for 10 minutes, rinsed with distilled water and then let dry in air. Finally, the slides were subjected to UV/O₃ for 30 seconds to restore the surface oxide layer and stored in an oven until use.

The substrate was then loaded onto a substrate holder and placed in the furnace of our ALD reactor close to the injection point (Figure 3.2). The deposition sequence used was developed previously by our lab,⁸³ where one cycle consists of a 5 s pulse of aluminum precursor, a 5 s pulse of N₂, a 10 s evacuation, a 5 s pulse of water, a 5 s pulse of N₂ and finally a 10 s evacuation. This cycle was repeated as required to achieve a given thickness, with a deposition rate of 2.7 Å/cycle at 175 °C. The Al₂O₃ film thicknesses were determined by ellipsometry (Plasmos, HeNe laser at $\lambda = 632$ nm, $n_{\text{Si}}=3.882$,⁸⁹ $n_{\text{alumina}}=1.76$ ⁹⁰) and scanning electron microscopy (Tescan Vega-II XMU). ALD processes of this type tend to produce a thin SiO₂ interfacial layer between the silicon and Al₂O₃. This layer, which is on the order of 10 Å thick,⁹¹ has a trivial impact on the measurements presented here.

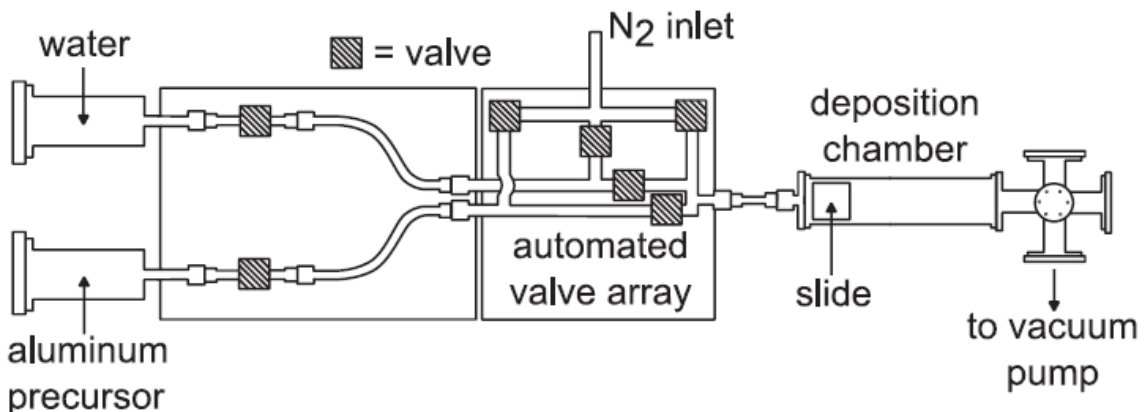


Figure 3.2 Schematic of the atomic layer deposition system.

Gonioreflectometry

Goniocolourimetric analysis of the thin aluminum oxide films on silicon was performed using a new gonioreflectometer developed at the National Research Council of Canada to measure bidirectional reflectance (Figure 3.3).⁸⁷ The instrument employs a uniform light source for sample illumination. This source is made of a sphere internally coated with barium sulfate that houses a tungsten halogen lamp behind an internal white baffle. The exit port of the sphere holds a precision aperture of 20 mm diameter that defines an area of uniform radiance. This radiance is first measured with an imaging spectroradiometer. The uniform light source is then used to illuminate the sample, and the reflected radiance is measured with the same spectroradiometer. The reflectance of the sample is derived from the ratio of the two measurements. This is done spectrally for the wavelength range 380 nm to 780 nm with a step interval of 1 nm. A five-axis robot is used as a sample holder and allows the precise positioning of the sample with respect to the sphere port and to the spectroradiometer. Elevation and azimuth angles of both the illumination direction and the reflection direction can be made to vary over full hemispheres.

The Al₂O₃-coated silicon substrates were mirror-like samples that scattered very little radiation outside the specular direction. The apparatus was thus set to measure in the specular directions only. In these conditions, the ratio of the reflected radiance to the

incident radiance corresponds to regular reflectance, a perfect mirror having a regular reflectance of 1.

The samples were measured for incidence angles (equal to the reflection angles) ranging from 10° to 70° in steps of 5° ; 10° corresponds to the minimum angle allowed before the sphere source occludes the detection path. For the measurement, the spectroradiometer stays focused on the mirror image of the uniform light source port to measure the central (3.5 mm diameter) portion. The sample itself acted as a mirror of finite size that can clip some of the reflected rays at large incidence angles. The angle of 70° corresponds to maximum incidence angle allowed for the samples (approximately 3.3 cm square) before this clipping occurs. The angular resolution is 1.2° and corresponds to the spectroradiometer's field angle (0.2°) plus the angular aperture of its imaging lens (1°).



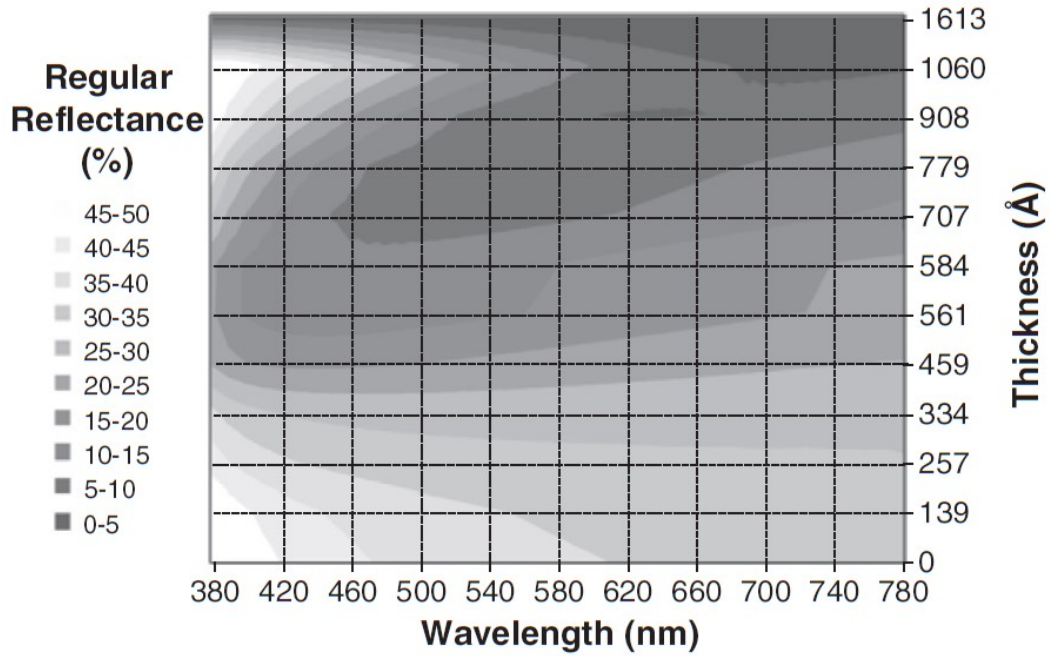
Figure 3.3 The gonioreflectometer used to collect reflectance data.

3.4 Results and Discussion

In a typical experiment, aluminum oxide was deposited to the desired thickness on a 3.3 cm x 3.3 cm silicon wafer. This wafer was then affixed to the “arm” of the gonioreflectometer, and the radiance of the reflected light was collected at angles ranging from 10° to 70° in 5° increments. This data is collected across the visible wavelength range of 380 nm to 780 nm with 1 nm sampling interval. Corresponding data was modelled using a software package (TFCompanion, ver3.4, Semiconsoft Inc.) that employs Fresnel equations⁹² to simulate the reflectance and transmittance of multilayer filmstacks. In the present work, the software was used to calculate the unpolarized

reflectance, which is an arithmetic mean of the reflectance of the p- and s-polarized light, over the same angles and wavelengths measured by the gonireflectometer. In general, there was good agreement between the observed response to incident light and the theoretical prediction (Figure 3.4). Figure 3.4(a) represents the observed reflectance (expressed as a percent) of light topographically over a data plane of wavelength versus film thickness, while Figure 3.4(b) represents the predicted values of these same data. It should be noted that the entire data space has the variables of film thickness, wavelength of reflected light, viewing angle, and percent reflectance. Thus, the data presented in the figures must always be a subset of the data space.

a) Experimental data



b) Calculated data

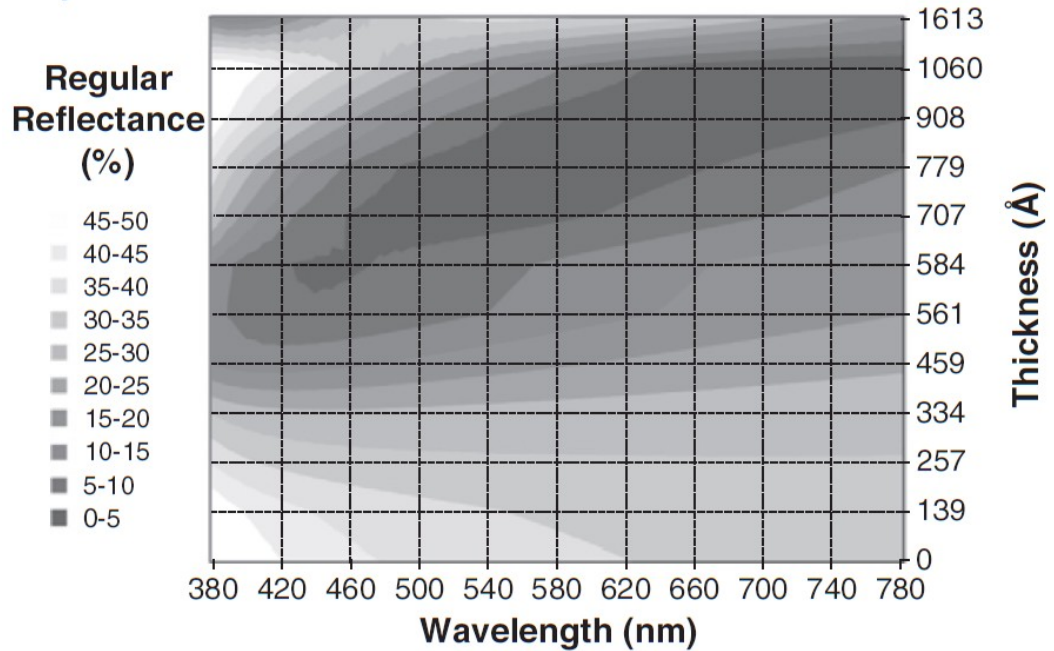


Figure 3.4 Experimental data (a) and calculated data (b) of the reflectance of films of various thicknesses with a viewing angle of 10° .

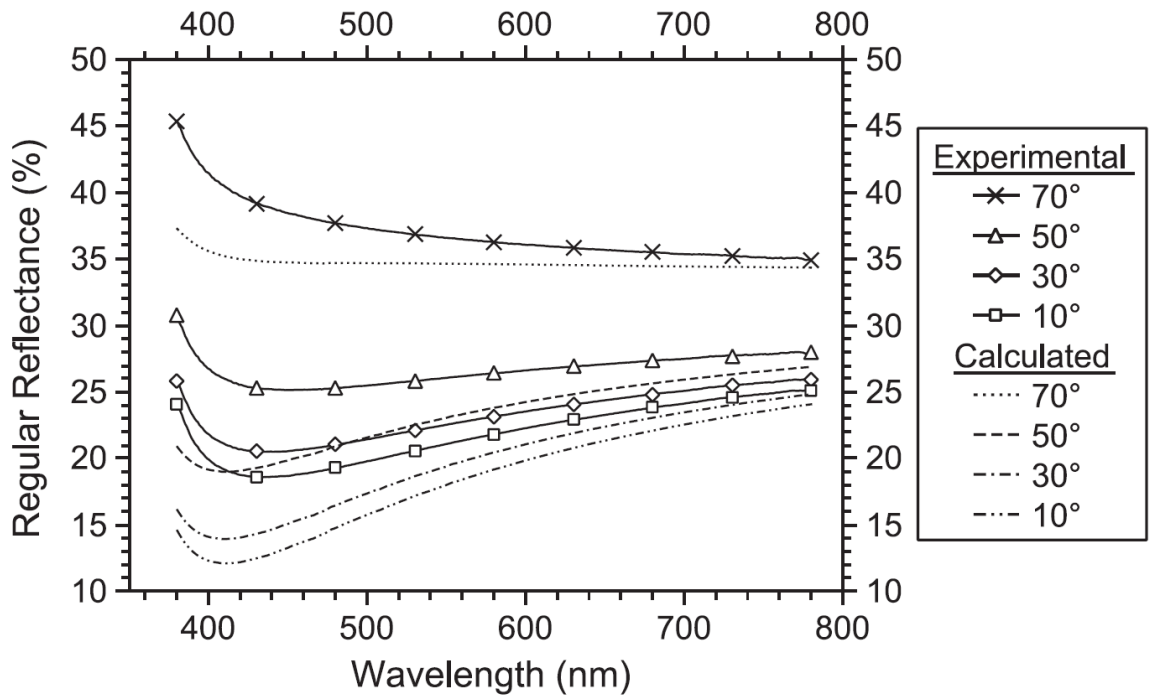


Figure 3.5 Experimental and calculated regular reflectance of a 459 Å film over the visible range of light at various viewing angles.

Consider a horizontal line at any given thickness in Figure 3.4. This represents the percent reflectance over all visible wavelengths at that thickness. The perceived colour of a film of that thickness would be the integration of this curve by the observer's brain (or "eye/brain" system). Figure 3.5 shows such reflectance curves for observation angles from 10° to 70° for a 459 Å film.

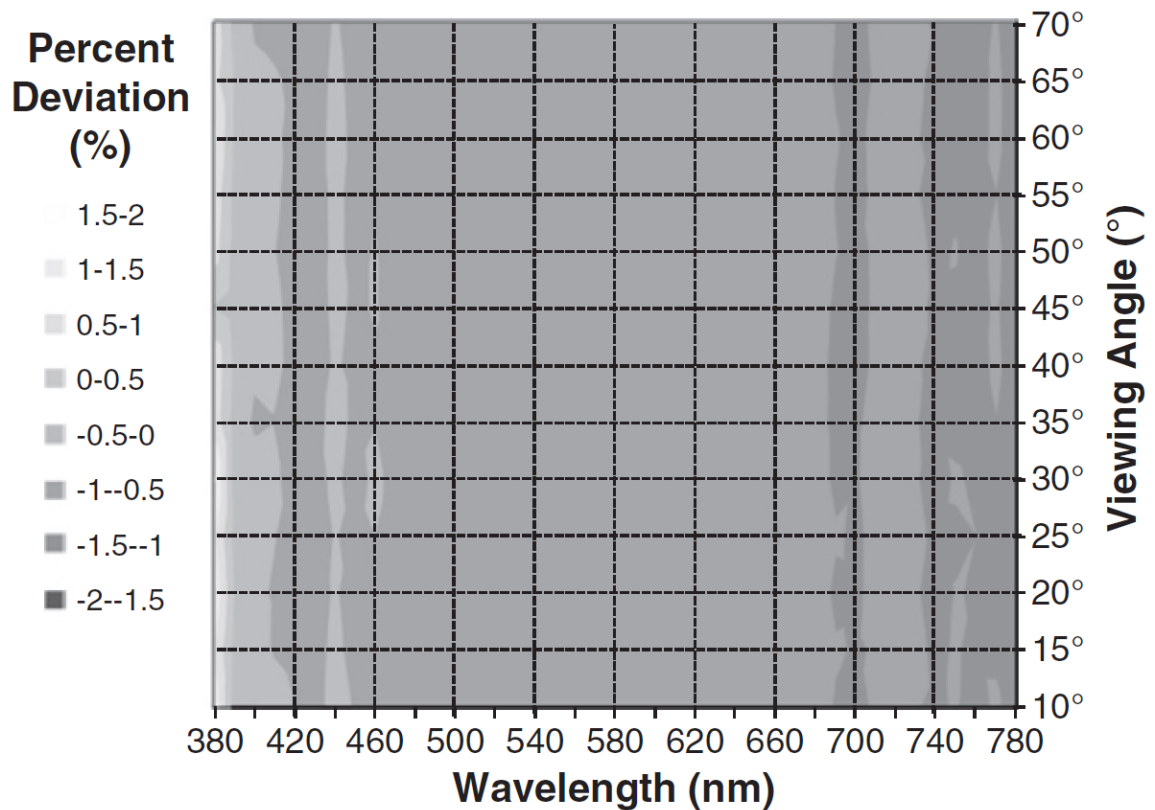


Figure 3.6 Plot of percent difference between experimental and calculated values for reflectance against wavelength and viewing angle for a bare silicon (100) wafer. Note that the topographical scale is in the range -2 to $+2\%$.

A 459 \AA film shows a higher reflectance at 380 nm and 70° (oblique) viewing angle, which tapers off at higher wavelengths. This suggests that this film thickness will show an enhanced blue colour when viewed at 70° from normal. As the viewing angle moves closer to normal, two effects are obvious. The film appears less reflective overall, with a general drop in regular reflectance. As well, there is an enhancement of lower energy reflectance, giving the film an orange cast. This iridescence is more pronounced in the predictive model than it is in the experimental samples.

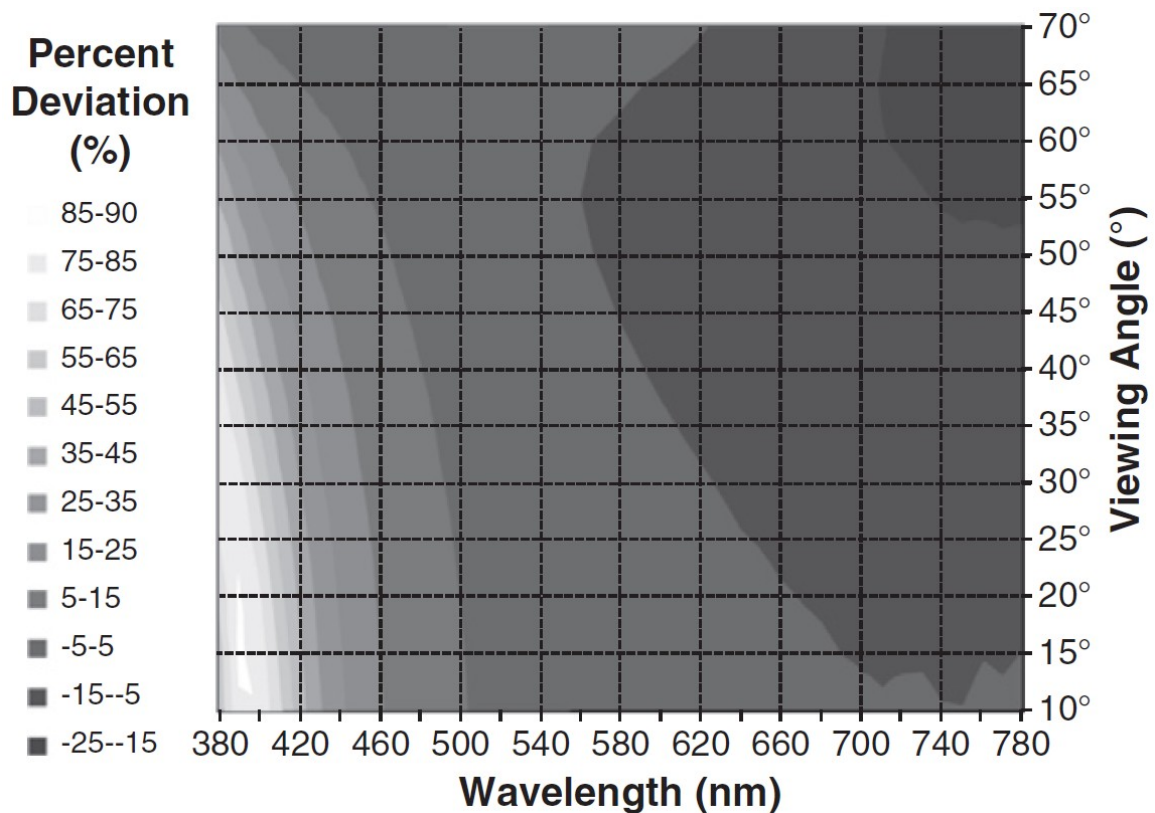


Figure 3.7 Plot of percent difference between experimental and calculated values for reflectance against wavelength and viewing angle for a 1613 Å Al_2O_3 film on a silicon (100) wafer. Note that the topographical scale is much larger than in Figure 3.6, ranging from -25% to +90%.

The observed deviations from predicted reflectance values were suspected to arise from using the dispersion curve of bulk alumina for simulation. To evaluate this source of error a 399 Å Al_2O_3 film deposited by a TMA/water ALD process was characterized by spectroscopic ellipsometry using a J. A. Woollam Co. Alpha-SE spectroscopic ellipsometer. The values obtained were then used to simulate the reflectance of a 459 Å film on silicon. (Figure 3.8b). A Cauchy model was assumed for the real part of the

refractive index of the Al_2O_3 film, given by $n(x) = A + B/x^2 + C/x^4$, where n is the refractive index, x is wavelength and A , B and C are fitted parameters. The model assumed three layers: a silicon substrate, a 19 \AA SiO_2 layer, and the Al_2O_3 layer. The values obtained for the 399 \AA film were 1.629, 0.00734 and -0.0001328 for A , B and C respectively. The film thicknesses measured using the bulk value of Al_2O_3 are considered valid as they have been previously confirmed to agree with measurements made by SEM. Reflectivity deviations from observed values were diminished but remained significant, with reflectivity measurements for the 459 \AA film deviating by as much as 14.8%. The largest deviation using bulk values for the same simulation was 66.6%. As with other samples, observed values remained in general larger than predicted and were most pronounced at a low viewing angle and shorter wavelengths. The growth rates for the amidinate/water process are faster by a factor of 2.5 and so efforts are underway to obtain Cauchy values for the films deposited by this method to determine if the deviations are attributable to film properties or the 60 \AA difference in film thickness. The faster growth rate of the amidinate/water process very likely results in a film with a different density and therefore different optical properties.

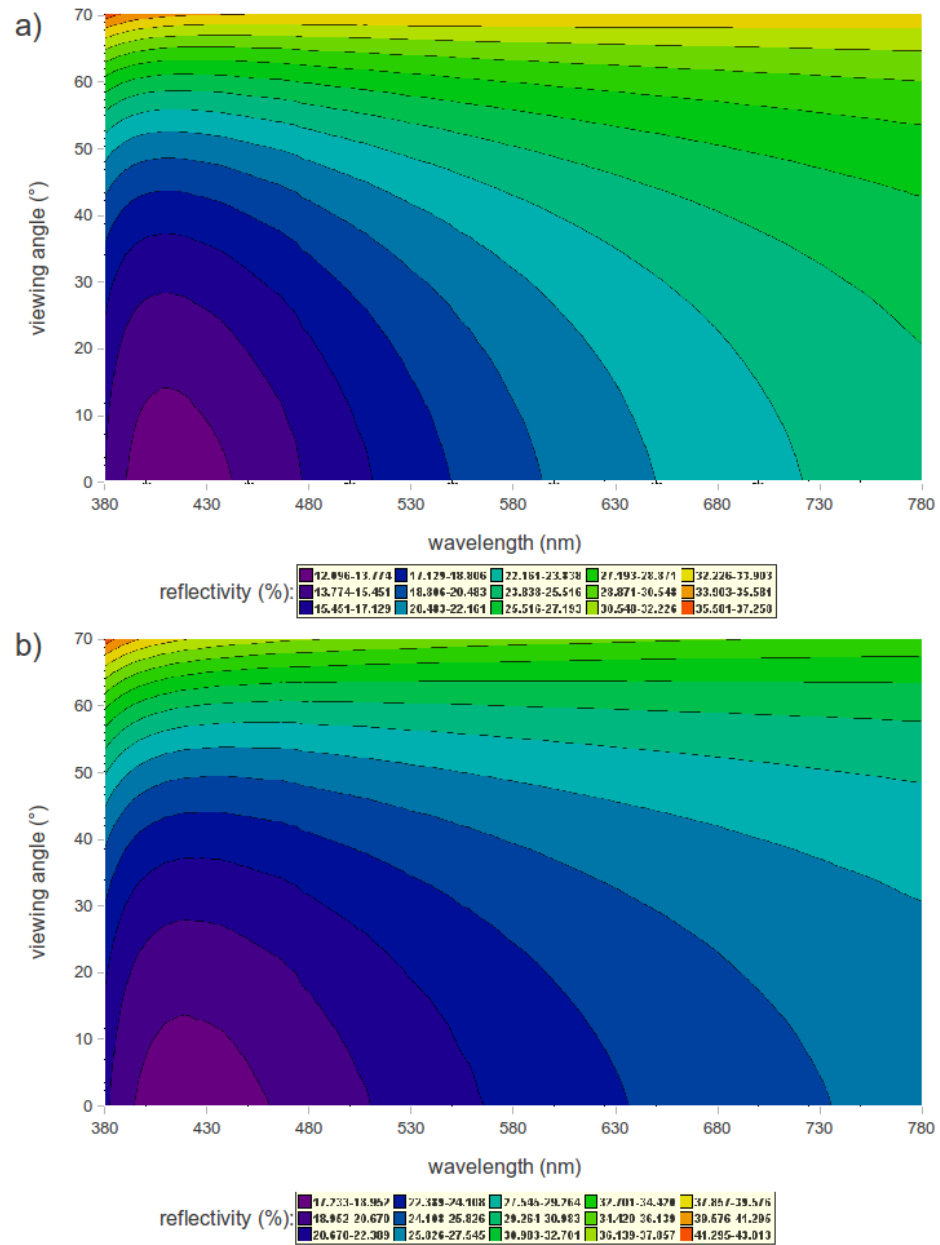


Figure 3.8: Reflectivity calculations for a 459 Å aluminum oxide film on silicon using a) the bulk dispersion curve for aluminum oxide and b) the dispersion curve as measured experimentally for an aluminum oxide film deposited by ALD.

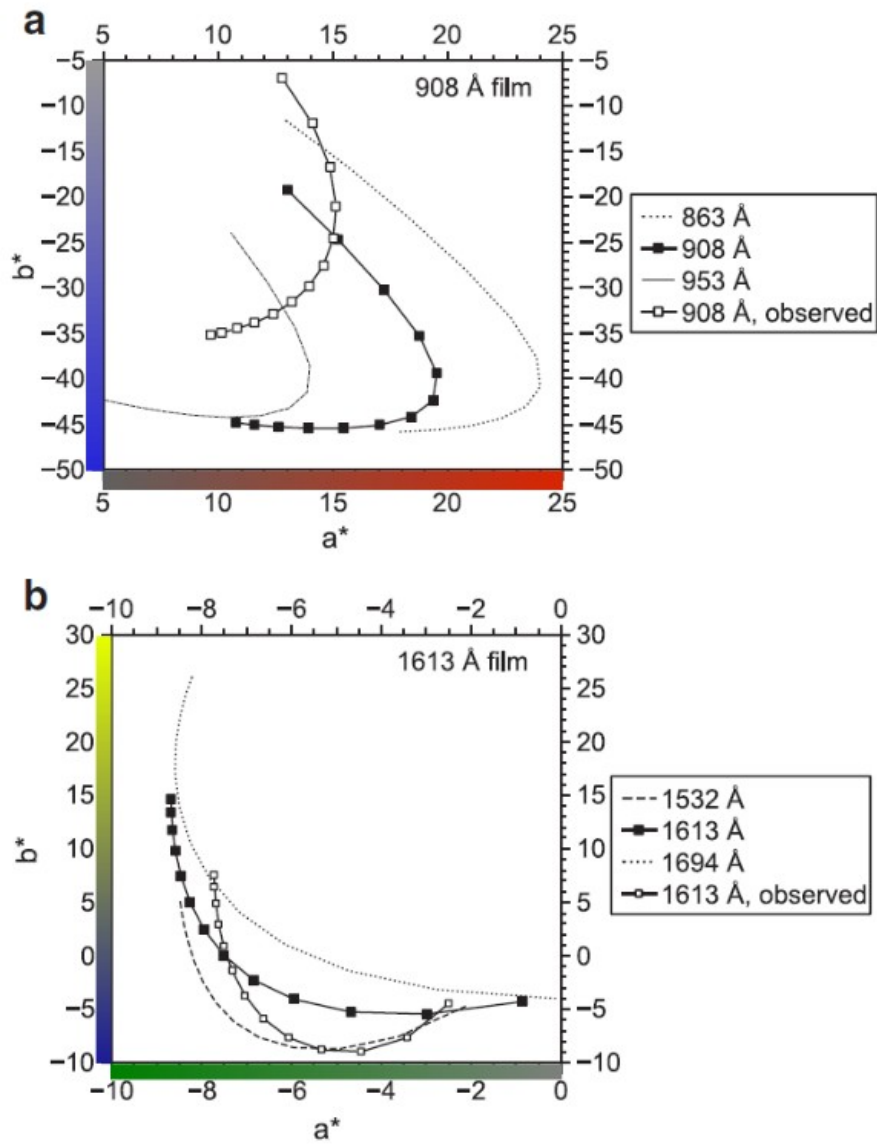


Figure 3.9 a^*b^* CIELAB (CIE D65) plots of (a) observed and (b) calculated data for selected film thicknesses over a range of viewing angles. Coloured axes are approximate representations of the CIELAB space to help guide the eye.

A comparison of the calculated versus experimental data showed an interesting trend.

When predicting the difference in reflectivity of a bare silicon substrate, the model showed only $\pm 2\%$ error (measured against the experimental value), with the errors

confined to the high and low ends of the visible wavelength range and similar across all viewing angles (Figure 3.6). When we consider the as-deposited aluminum oxide films, the range of error is much more severe (Figure 3.7). Here the errors are also found at the extremes of the wavelength range, with low wavelength errors reaching over 90%. The high wavelength errors are somewhat less severe (generally on the order of 20%), but over a much greater wavelength range.

These errors likely stem from the fact that the model employs dispersion curves for bulk aluminum oxide; ALD deposited alumina can show a process-dependent variation in density, and thus the index of refraction will be manifestly different. For example, Groner et al. reported⁹¹ a variation in density of 2.5 to 3 g/cm³ and in corresponding refractive indices of 1.5 to 1.6 for Al₂O₃ deposited by ALD using trimethyl aluminum and water precursors over a temperature range of 33 to 177 °C, whereas the literature bulk values are 3.97 g/cm³ and 1.76.⁹⁰ This being the case one might expect that the measurements with longer path lengths (thickest film at the lowest viewing angle) would show the largest deviation from the model. However, this is not observed: the largest deviations are found at near normal angles and the thickest film does not exhibit the largest deviation from theory. This discrepancy requires a much more rigorous study of the dispersion curves for ALD deposited Al₂O₃, and this is the subject of ongoing research in our laboratories.

With respect to the visual appearance of the deposited films, colour analysis is best understood in standardized colour space. The Commission Internationale de l'Éclairage

(CIE) has developed a system for the unambiguous specification of colour.⁹³ With this system, a light stimulus of a given spectral power distribution is first transformed into tristimulus values X , Y , and Z that are in a linear relationship with the amount of monochromatic red, green and blue of an additive mixture that would visually match the light stimulus. The calculation uses the colour matching functions $\bar{x}(\lambda), \bar{y}(\lambda), \bar{z}(\lambda)$ of a the so-called Standard colourimetric Observer as weighting functions for the numerical integration of spectral power over wavelength as follows:

$$[X, Y, Z] = k \int P(\lambda) [\bar{x}(\lambda), \bar{y}(\lambda), \bar{z}(\lambda)] d\lambda, \quad (1)$$

where $P(\lambda)$ is the spectral power distribution of the light stimulus and k is a constant that scales to photometric units. The CIE has established two sets of colour matching functions for performing this calculation.⁹⁴ The first one, adopted in 1931, was established with 2° viewing fields, and the second one, adopted in 1976, was established with 10° viewing fields. There is a fairly large degree of equivalence between the two sets and the 2° Standard colourimetric Observer is retained for this study.

The CIE has also adopted a series of spectral power distribution of so-called Standard Illuminants that are representative of commonly encountered natural or artificial lighting conditions, and that allow the calculation of tristimulus values for reflecting materials.⁹⁵ In this case, equation 1 is replaced by

$$[X, Y, Z] = 100 \frac{\int R(\lambda) S(\lambda) [\bar{x}(\lambda), \bar{y}(\lambda), \bar{z}(\lambda)] d\lambda}{\int S(\lambda) \bar{y}(\lambda) d\lambda}, \quad (2)$$

where $S(\lambda)$ is the spectral power distribution of the standard illuminant, and $R(\lambda)$ is the reflectance of the surface. This is the formula used herein, with the integrals evaluated through summation in 1 nm steps from 380 nm to 780 nm. The formula is scaled in such a way that $Y=100$ for the theoretically perfect white reflector, an idealized surface that has a reflectance of 1 at all wavelengths. Among the standard illuminants proposed by the CIE, CIE Standard Illuminant D65 and CIE Standard Illuminant A are recommended for use whenever possible. Illuminant D65 is a good representation of average daylight, and illuminant A corresponds to the light from a blackbody radiator at temperature 2856 K. Both were used in our calculations, although only the D65 data is represented here for simplicity.

$P(\lambda)$ and $S(\lambda)$ have similar definitions but are different in an important and subtle way. $P(\lambda)$ refers to the spectral power distribution from the light stimulus (the field the eye is looking at), e.g. a computer display, the light reflected by a leaf under sunlight, etc. $P(\lambda)$ can be measured with a spectroradiometer.

$S(\lambda)$ refers to a Standard Illuminant. This is a theoretical illuminant available in tabular format from the CIE. The CIE has a number of Standard Illuminants that are representative of typical light sources, such as daylight (CIE Standard Illuminant D65), incandescent lighting (CIE Standard Illuminant A), fluorescent lighting (CIE Standard Illuminants F1 to F8), etc. With this scheme it is $R(\lambda)$ that is measured, usually with a spectrophotometer, rather than $P(\lambda)$. Using $S(\lambda)$ in Eq.(2) is standard CIE notation.

The tristimulus values X , Y , and Z can be thought of as correlates to the outputs from the three types of cones in the human retina. The signals from these cones are transformed by the brain into colour sensations through a very complex process that is still not fully understood. Nevertheless, the CIE has proposed a number of mathematical models to transform tristimulus values into various colour quantities that correlate well with appearance attributes such as hue, saturation, lightness, brightness and many other characteristics. These models (in addition to the sample itself) at the very least take into consideration the white against which colours are judged, plus others factors such as the background, the surroundings, and the degree of adaptation.⁹⁶ For cosmetic applications, the data measured by gonioscolourimetry can thus be used to predict the colour appearance of interference films of aluminum oxide under a wide variety of viewing conditions. One of the most simple models, retained for this study, is the CIELAB colour space where tristimulus values X , Y , and Z are transformed into L^* , a^* and b^* values according to⁹⁷

$$L^* = 116(Y/Y_n)^{1/3} - 16,$$

$$a^* = 500[(X/X_n)^{1/3} - (Y/Y_n)^{1/3}],$$

$$b^* = 200[(Y/Y_n)^{1/3} - (Z/Z_n)^{1/3}],$$

where X_n , Y_n , Z_n are the values of a white achromatic stimulus and are specified here to correspond to the reflection of the white illuminant by a reflector with regular reflectance equal to 1. In these equations, when a ratio X/X_n , Y/Y_n , Z/Z_n is smaller than 0.008856, it is replaced by $7.787F+16/116$ where F is that ratio. With this system L^* corresponds to

perceived lightness and has a value of 100 for a perfect mirror, a^* corresponds to (red – green) and b^* corresponds to (yellow – blue). A derived quantity, $C^* = (a^{*2} + b^{*2})^{1/2}$ corresponds to chroma and becomes 0 for an achromatic colour. The CIELAB space was designed to be perceptively uniform, and a difference of 1 unit in any direction roughly corresponds to a colour difference at the threshold of differentiation by the human eye.

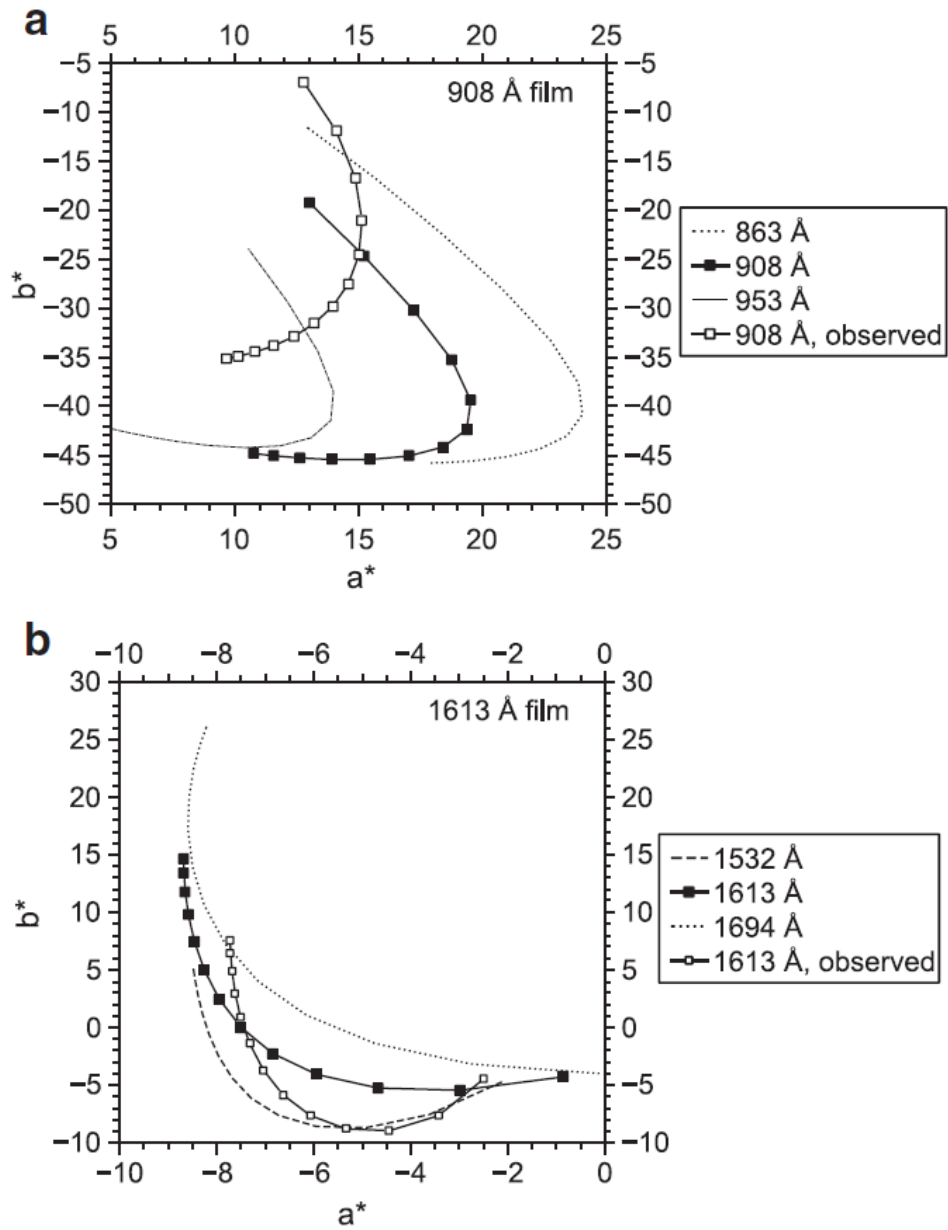


Figure 3.10 a^*b^* CIELAB (CIE D65) plots comparing +/- 5% error estimates for (a) 908 Å and (b) 1613 Å films with observed data. Each point corresponds to a viewing angle.

Figure 3.9 shows some results for nine different thicknesses. It can be seen that the 0 Å coating (bulk Si) produces the least iridescence. This sample appears grey with a very slight blue cast, and the colour variation with angle is only 3 units along the blue axis, making it barely detectable by eye. For bare Si, the measurements agree with the predictions. The 908 Å sample exhibits the largest iridescence. The colour goes from very chromatic purplish blue, at 10° viewing, to a greyish purple pink at 70° viewing. It can be observed that it is for the highly iridescent coatings that the difference between the measurement and the prediction is the highest. The iridescence appears much pronounced for the prediction, and the colour itself at some given angle can differ by more than 20 units.

To determine if the discrepancy between observed and calculated data was simply due to film thickness measurement error introduced by the ellipsometer, additional plots of +/- 5% thicknesses were calculated for 908 Å and 1613 Å (Figure 3.10 a) and b) respectively). These plots illustrate that while a 5% measurement error would have a significant impact on the shape of the curves, the induced variations would not be in the directions of the observed discrepancies. Instead it is most likely the dispersion curves of the deposited material are responsible for these discrepancies.

This comparison demonstrates that for cosmetic applications, in which the final colour is of primary concern, it is important to actually measure the end product and not rely just on predictions.

3.5 Conclusions

A robot-based gonireflectometer has been used to analyze the colours resulting from thin films of aluminum oxide deposited by ALD on silicon with unprecedented precision. A comparison has been made between the experimental reflectivities obtained and those predicted by software simulations. For the range of thicknesses studied (0 - 1613 Å), the largest disagreement between theory and experiment was observed for the films of intermediate thicknesses, which are also the most iridescent. The largest disagreement for a given sample was most often found at short wavelengths, with 7 of the 12 samples exhibiting their largest deviations from the model between the wavelengths of 380 and 445 nm. An analysis of the data with respect to angle showed that the disagreements were higher at near-normal angles of reflection ($\leq 15^\circ$). This is not totally surprising: while one might expect the larger deviations to occur at more oblique angles, where the path length through the film is longest, the reflection itself is dominated by interference between phase shifted wave fronts, and this phase shift decreases with reflection angle. Further studies are necessary to determine the dispersion curves of the deposited films, which should allow for a more accurate simulation of the system. It is very likely that the dielectric constants of the films deviate from the literature values as ALD processes are known to deposit films with densities that differ from bulk values, depending on process parameters.

Chapter 4 - Characterization and assessment of a novel hybrid organic/inorganic metal-insulator-semiconductor structure for photovoltaic applications

Modified from original manuscript, published as:

Svetlana Demtchenko^{*a}, Peter Gordon^b, Sean Barry^b, N. Garry Tarr^a, Steven McGarry^a “Characterization and assessment of a novel hybrid organic/inorganic metal-insulator-semiconductor structure for photovoltaic applications” *Proc.SPIE 7750*, **2010**, DOI 10.1117/12.871360.

^aDepartment of Electronics, Carleton University, Ottawa

^bDepartment of Chemistry, Carleton University, Ottawa

4.1 Abstract

Hybrid organic/inorganic photovoltaic devices have recently emerged as a possible solution to the stability, charge transfer and mobility issues that have been limiting the lifetimes and efficiencies of organic solar cells. The purpose of the project presented here is to assess the potential of a new hybrid metal-insulator-semiconductor (MIS) photovoltaic device design developed at Carleton University. The silicon substrate is nanostructured with a wet chemical etch resulting in about 1:1 aspect ratio structures of roughly 300 nm in size. The interface is passivated with a thin dielectric tunnel barrier of alumina or silica. A layer of transparent conducting polymer, Poly(3,4-ethylenedioxythiophene) (PEDOT), is added through *in-situ* polymerization. The structure is then completed with a printed silver/polymer composite collection electrode. The electrical current-voltage (I-V) and capacitance-voltage (C-V) characteristics along with the effect of nanostructuring the substrate on the performance of such a solar cell is

explored by comparison with unstructured devices. The C-V and I-V measurements are used to estimate changes in the effectiveness of the device junction due to the structuring. The quality of the insulator layer as well as its optimal thickness are studied. The fabricated structures show photovoltaic behaviour with the structuring yielding a significant increase in efficiency. The test structures show promise for the use in photovoltaics and further optimization of such a structure may yield fruitful results in solar applications.

4.2 Introduction

We propose to use a transparent conductive polymer, poly(3,4-ethylenedioxythiophene) (PEDOT) in place of the metal layer in the MIS structure. Additionally, to boost light capture we propose to incorporate a nanostructured surface to increase the path length of the light at the surface of the cell. The combination of these two techniques may eliminate the need for a costly anti-reflection coating. To date we have made and assessed flat structures with SiO₂ as the dielectric. Since thermal oxidation consumes silicon during processing (undesirable for nanostructured substrates) we have explored deposited dielectrics. Atomic layer deposition (ALD) is particularly attractive since it is capable of growing ultra-thin films with excellent uniformity, conformality, and thickness control.⁸³ Accordingly, we have made flat and nanostructured devices incorporating an ALD deposited Al₂O₃ layer.

A small set of cells were fabricated and tested. The fabrication flow was designed to use a vacuum-less process aimed at further reducing the cost of such a device. Our efforts in assessing the feasibility of such structures for photovoltaic applications are described herein.

The open circuit voltage (V_{oc}) of an MIS device depends on the photogenerated current (I_{sc}) and the reverse saturation current (I_o) as follows⁹⁸:

$$V_{oc} = \frac{nkT}{q} \ln\left(\frac{I_{sc}}{I_o} + 1\right)$$

Thus to increase the open circuit voltage and the overall performance of the cell, the reverse saturation current has to be minimized.

There are a number of schemes known to result in a reduced reverse saturation current in an MIS type structure. To achieve this effect the metal/semiconductor barrier height can be increased, the probability of the majority carriers tunneling through the insulator barrier can be decreased, or surface states at the semiconductor/insulator interface can be included that preferentially capture majority carriers.⁹⁹ In our devices the insulator layer serves to increase the barrier height for thermionic emission and the probability of majority carrier tunneling is reduced by the inversion of the semiconductor surface, since the tunneling probability depends on the population of states on both sides of the junction.

Such inversion at the interface will also ensure that the interfacial states are occupied by the minority carriers and thus reduce the surface recombination due to the interfacial states. The inversion condition can be achieved with high work function metals for n-type material. For silicon substrates the metal work function has to be⁷²:

$$\varphi_m \geq \chi + E_g$$

$$\varphi_m \geq 4.05 \text{ eV} + 1.1 \text{ eV}$$

$$\varphi_m \geq 5.15 \text{ eV}$$

were χ is the electron affinity of silicon and E_g is silicon's band gap. This condition is satisfied for PEDOT:PSS with an accepted work function of $\varphi_m \approx 5.2 \text{ eV}$.¹⁰⁰

Thus the structure of such a hybrid MIS device is as shown in Figure 4.1. The n-type Si substrate captures the light. The surface of the substrate can be flat or structured as shown in the figure. Even though an ordered structuring is depicted, a random structuring would result in better light capture, which is what our structuring process achieves. On top of the substrate surface an ultra-thin layer of dielectric is grown or deposited, followed by PEDOT. The structure is completed with a screen printed finder-grid contacts.

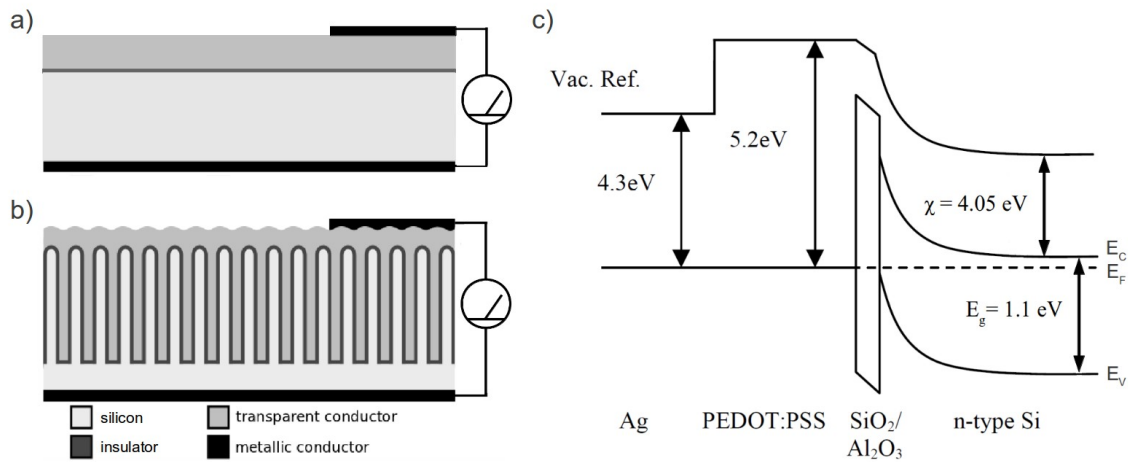


Figure 4.1 Representations of the hybrid MIS device. Flat device is shown in (a), nanostructured device shown in (b) and band diagram in (c).

For an optimal device with current-voltage characteristics approaching those of a p-n junction, the insulator layer must remain thin, less than 20 Å.^{71,72} As the thickness of the insulator influences the tunnelling probability of minority carriers as well as the majority carriers, as the V_{oc} increases with the increasing thickness, the I_{sc} will decrease. Thus there exists an optimal thickness of the insulating layer for the best performance of a photovoltaic device.

4.3 Experimental

The starting material used was n-type Si with 1-10 Ω·cm resistivity. The wafers were cleaned before processing. Three different types of structures were fabricated and examined: flat devices with thermally grown oxide, flat devices with Al₂O₃ grown by

ALD, and devices on nanostructured substrates with ALD Al_2O_3 . The fabrication for each structure is detailed below.

Flat devices with thermally grown oxide

The front side of the wafers was treated with HF vapour to remove any native oxide. After the HF treatment the wafers were immediately placed in an oxidation furnace for 10 min at various temperatures (450 °C – 550 °C) to grow increasing thicknesses of SiO_2 . Oxidation was followed by deposition of backside aluminum by evaporation. PEDOT:PSS (Clevios PH750 supplied by H.C. Starck) was spin-cast on top of the grown oxide. The structure was completed by screen printing silver ink (Dupont 5028). A finished wafer of devices is shown in Figure 4.2(a). The wafers were stored in a dry nitrogen box or under vacuum between processing steps to avoid undesirable continued growth of the oxide layer.

Flat devices with ALD Al_2O_3

The back side of the wafer was metallized with aluminum and Al_2O_3 was grown by ALD on the front surface. The samples were then annealed at 400 °C in forming gas (N_2 with 5% H_2) to activate the passivation of silicon by Al_2O_3 as was found necessary by Dingemans et al.; forming gas was used instead of N_2 to take advantage of hydrogen passivation of dangling bonds on the silicon surface as the chemical passivation by Al_2O_3 at such small layer thicknesses is deemed ineffective.¹⁰¹ High conductivity PEDOT:PSS

(Clevios FET supplied by H.C. Starck) was spun down on top of the alumina. The structure was completed by screen printing silver ink (Dupont 5028) as before.

Nanostructured devices

The nanostructuring was achieved with a wet chemical etch based on the procedure reported by Branz et al.¹⁰² The colloidal gold (5 nm particle size) solution (purchased from Sigma-Aldrich; #G1402) was dried on the silicon substrate overnight at room temperature. The substrates were not heated to minimize the aggregation of gold particles. Thus prepared substrates were sonicated in HF:H₂O₂:H₂O (1:5:2) to effect the metal-assisted chemical etch (MACE). MACE is a technique for etching silicon or other semiconductor surfaces, typically using a surface layer of silver or gold (nanoparticulate or porous) and a solution of HF and an oxidant.^{103,34,104,105} The nanostructured substrate was then washed in *aqua regia* to remove the remaining gold particles. An aluminum back contact was evaporated on to the back of the substrate and sintered at 400°C for 10 min in H₂. Various thicknesses of Al₂O₃ (~ 4-14 Å) were grown by ALD. The PEDOT was deposited in situ from EDOT monomer (Baytron M) using Fe(III) tosylate in butanol (Baytron CB-40) as an oxidizer. Silver ink was deposited on top of the structure as the current collecting electrode. A set of flat samples was processed in parallel for comparison.

Testing the devices

The current-voltage (I-V) and capacitance-voltage (C-V) characteristics of the devices were measured with HP4155 parameter analyzer and HP4280A capacitance meter respectively to access the quality and the performance of the devices. The shunt and series resistances of the structures as well as the ideality factor can be extracted from the I-V curve. The C-V measurement can be used to assess the effective surface area increase due to substrate structuring as well as to estimate the effective barrier height in the MIS structure. The measurements were performed in the dark as well under illumination using a halogen lamp as a quasi-white light source. A silicon detector was used to measure the incoming power. Some testing was also performed under an Oriel 92191 solar simulator with AM1.5D filter at 25 °C as shown in Figure 4.2(b).

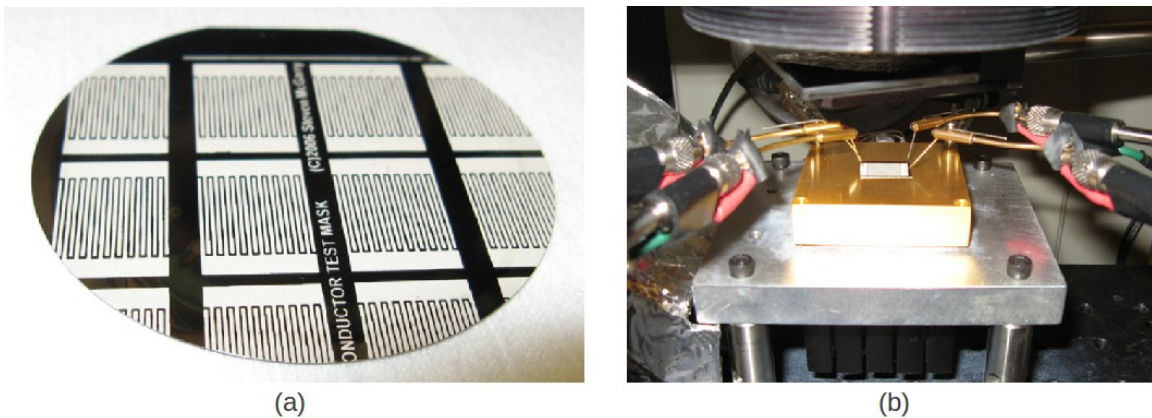


Figure 4.2 Processing and testing of devices: (a) 2” wafer of devices (b) testing of an individual device under the solar simulator.

4.4 Results and Discussion

Flat devices with SiO₂ insulator

The I-V characteristics of the flat devices with thermally grown SiO₂ (roughly 1 nm to 5 nm in thickness)¹⁰⁶ show the expected decrease in reverse current and the desired increase in the turn on voltage with increasing oxidation temperature (and thus increasing oxide thickness) as shown in Figure 4.3. The high series resistance evident in the I-V characteristic of the device with no intentional oxide is explained by the recombination at the silicon/PEDOT interface as the silicon surface is not passivated. The grown oxide provides surface passivation, as is evident from the much lower series resistance of the other devices. The device with the thickest oxide grown at 550 °C shows the highest turn on voltage as expected (Figure 4.3(a)). The non-saturating behaviour of the reverse current is usually attributed to the image force lowering of the Schottky barrier height and the presence of the insulating layer at the metal semiconductor interface (Figure 4.3(b)).¹⁰⁷

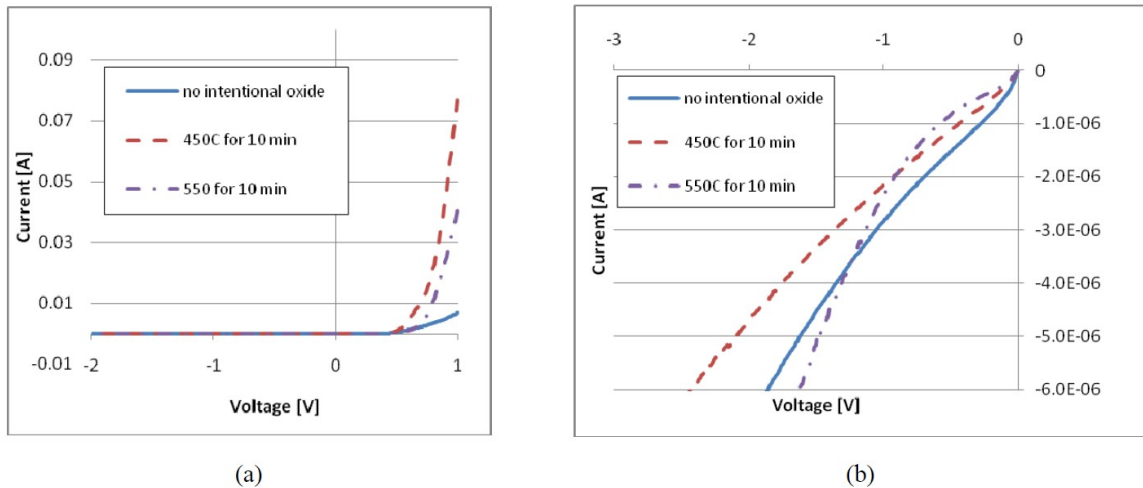


Figure 4.3 I-V characteristics of flat MIS devices with SiO₂ (a) full dark IV curves (b) dark reverse saturation current.

Additionally the devices exhibit a linear $1/C^2$ vs V relationship confirming the depletion nature of these diodes. The potential barrier height is related to the voltage intercept of this trend as

$$\phi_{B_n} = V_i + V_n + \frac{kT}{q} - \Delta\phi$$

where V_i is the voltage intercept, V_n is the depth of Fermi level below the conduction band, and $\Delta\phi$ is image force barrier lowering.¹⁰⁸ As the substrates were all of similar doping level and the image force lowering is expected to be about the same, the voltage intercept is a good measure of relative barrier height between samples with different oxide thicknesses.

These intercepts were extracted from the V-C characterizations and were found to show the expected barrier height increase with increasing oxidation temperature as summarized in Table 4.1.

Table 4.1 Voltage intercepts from the V-C characterization of flat MIS devices with SiO₂ insulator showing increasing barrier height with increasing oxidation temperature.

Sample	V_i/V
no intentional oxide	0.721 ±0.001
450 °C for 10 min	0.7390 ±0.0008
500 °C for 10 min	0.7444 ±0.0004
550 °C for 10 min	0.811 ±0.001

All of the flat MIS devices with SiO₂ showed photoresponse when illuminated with the halogen lamp. The photoresponse of the Schottky junction device with no intentional oxide was measured under a solar simulator to get an absolute efficiency measurement. The individual devices were cleaved out of the wafer to perform the measurement such that the area of the cell corresponding to the current measurement could be known. The resultant I-V characteristic in Figure 4.4(a) shows a distortion at low currents which is believed to be due to the reverse breakdown of the Si/Al junction as the Al was not sintered post deposition. Identical devices with sintered Al back contacts were made and tested to confirm this theory. As can be seen in Figure 4.4(b) devices with sintered contacts show no distortion as expected. The short circuit current density (J_{sc}) can still be extracted from the measurement and was found to be 18.5 mA/cm² at 0.8 sun illumination with 50% shading due to the non-optimized current collecting finger grid.

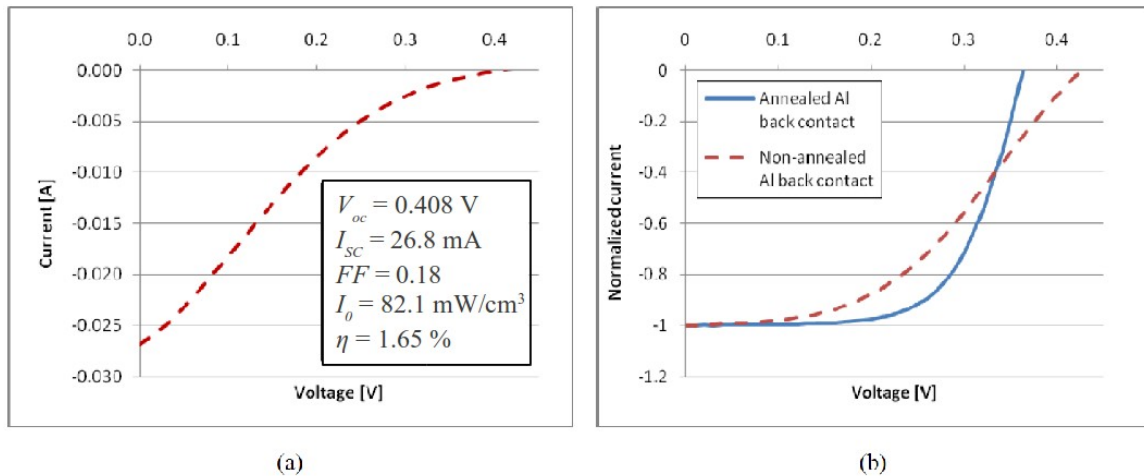


Figure 4.4 Illuminated I-V characteristic of an MIS device with no intentional oxide; (a) measured under a solar simulator (b) measured under a halogen lamp with a sintered back contact and a non-sintered contact.

Since J_{sc} is directly proportional to the illumination level,¹⁰⁹ the short circuit current at 1 sun (100 mW/cm²) can be extrapolated to be 23 mA/cm². Optimizing the current collection grid to a typical 15 % shading for screen printed cells¹⁰⁹ should increase the J_{sc} to 33.0 mA/cm². Superimposing this short circuit current on the dark IV curve of the device oxidized at 550 °C we can expect a fill factor of FF = 0.66. If an open circuit voltage is taken to be $V_{oc} = 0.536$ V as reported in the literature for n-Si based devices with SiO₂ insulator and Au metal,⁷¹ the efficiency of such a device can be estimated to be $\eta_{predicted} = 11.7$ %. The predicted device parameters are summarized in Table 4.2.

Table 4.2 Predicted parameters of the optimized flat MIS device with SiO₂ insulator and PEDOT as the metal.

V_{oc}	0.536 V ¹
J_{sc}	33.0 mA/cm ²
FF	0.66
$\eta_{predicted}$	11.7 %

Flat devices with ALD Al₂O₃ insulator

As it was not yet possible to measure the Al₂O₃ layer thicknesses directly, the samples are referred to in terms of ALD cycles of Al₂O₃ growth. The range of 2 to 5 cycles, examined here, should yield about 0.5 nm to 1.5 nm thick layers of alumina respectively.⁸³ The devices show diode I-V characteristics as seen in Figure 4.5(a). The reverse saturation currents observed on these devices are quite similar to the devices with SiO₂. The forward currents are, however, substantially lower. The devices also show

some photoresponse as seen in Figure 4.5(b). The photocurrents, again, are quite small. Such high current losses could be due to poor passivation of the surface by the grown alumina film. The nature of this carrier loss is currently under investigation.

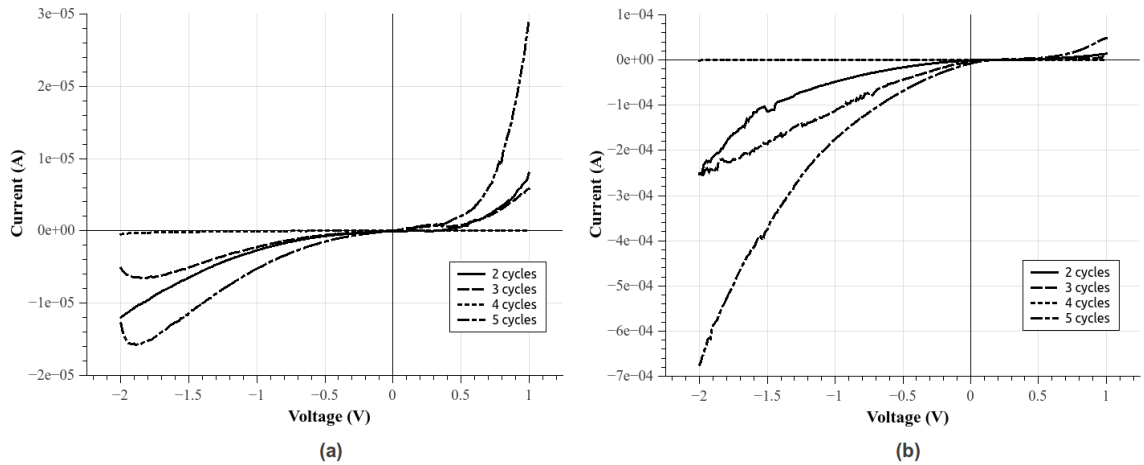


Figure 4.5 I-V curves for flat MIS devices with Al₂O₃ insulator (a) in the dark and (b) under illumination.

Nanostructured devices with Al₂O₃ insulator

The chemical etch of silicon surface results in approximately 1:1 aspect ratio random structuring with feature size of about 300 nm (due to partial aggregation of the colloidal gold particles during drying) as shown in Figure 4.6(a). The effective area increase of the surface was estimated by comparison of capacitance measurements of the structured and equivalent flat samples. The area increase was found to be 1.9 ± 0.4 . The error was taken to be the standard deviation of the values calculated for several samples. This calculated area increase agrees with the expected value of 2 for 1:1 aspect ratio structures as calculated for pyramidal structures of this aspect ratio.

The conversion efficiency of the wet-etched samples was limited by the dielectric layer, which was too thick for efficient charge tunnelling. However, the structured samples showed a considerable increase in efficiency (of up to five times) over the equivalent flat samples as can be seen in Figure 4.6(b) below.

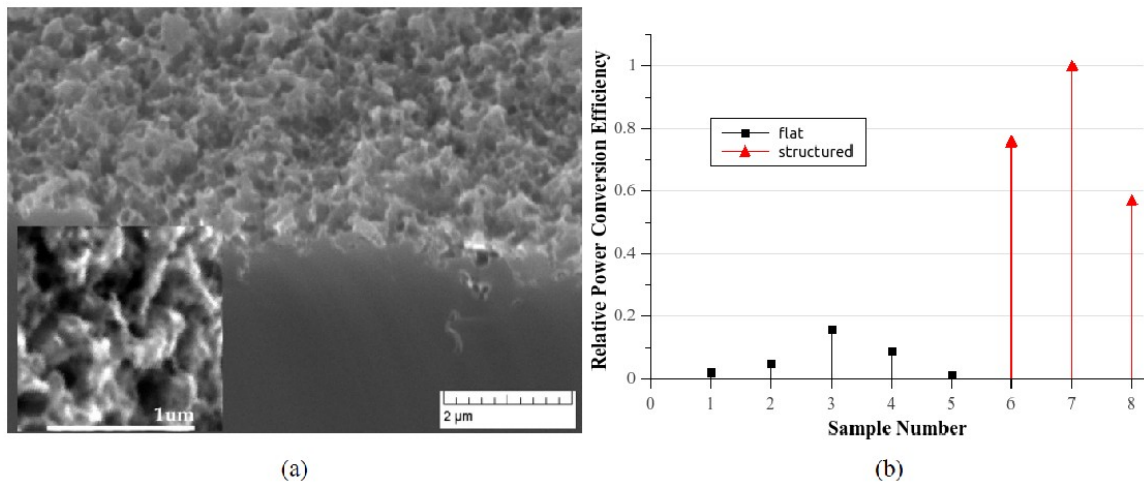


Figure 4.6 Nanostructured MIS devices; (a) SEM image of surface structuring and (b) relative power conversion efficiency of a set of structured and flat MIS devices processed in parallel with 8 Å Al_2O_3 insulator.

4.5 Future Work

We have shown that good photovoltaic MIS devices are possible when a traditional metal is replaced with PEDOT. Such MIS devices with SiO_2 insulating layer show good diode characteristics and good photoresponse. It was demonstrated that efficiencies of over 10 % should be easily achievable for optimized structures. This work, however, still presents a number of exciting research opportunities.

The improvement of the devices with ALD deposited dielectrics is of high interest, as the ALD process is deemed crucial to successful fabrication of structured devices. To this

end the ALD insulator process is still in development - other methods, precursors and compositions are under investigation.

To achieve higher aspect ratio structures self-masking electron cyclotron resonance reactive ion etching (ECR RIE) has been used. Structures with 10:1 aspect ratio were fabricated. The testing of the devices made on these substrates is ongoing. Additionally, to create finer structures with a wet chemical etch an alternative gold deposition method will be attempted, known to result in a uniform controllable particle density on the surface.¹¹⁰

It is expected that spin coating of PEDOT:PSS will be incompatible with the high aspect ratio structures that we hope to use on the substrates in the future. To mitigate this problem we will deposit PEDOT by vapour phase polymerization (VPP). Such deposition method is known to result in conformal coverage with well controlled thickness and conductivities of over 1000 S/cm.^{111,76,112} The assembly of the deposition system is in progress.

4.6 Acknowledgements

The authors would like to thank Rob Vandusen, Carol Adams, and Rick Adams for their invaluable help with the processing of the samples as well as Karin Hinzer and Mark Yandt for the use of their solar simulator. This project is financially supported by Natural Sciences and Engineering Research Council of Canada (NSERC).

Chapter 5 - Chemical vapour deposition of In₂O₃ thin films from a tris-guanidinate indium precursor

Modified from original manuscript, published as:

Barry, S. T.^a; Gordon, P. G.^a; Ward, M. J.^b; Heikkilä, M. J.^c; Monillas, W. H.^d; Yap, G. P.^d; Ritala, M.^c; Leskelä, M.^c *Dalton transactions* **2011**, 40, 9425–30.

^aDepartment of Chemistry, Carleton University, Ottawa, Canada K1S 5B6

^bDepartment of Chemistry, University of Western Ontario, London, ON, Canada N6A 5B7

^cLaboratory of Inorganic Chemistry, Department of Chemistry, University of Helsinki, P.O. Box 55, FI-00014, Finland

^dDepartment of Chemistry and Biochemistry, University of Delaware, Newark, 19716, Delaware, U. S. A. Accepted 17th June 2011, first published on the web 16th August 2011

5.1 Abstract

A new homoleptic sublimable indium(III) guanidinate, (In[(NⁱPr)₂CNMe₂]₃ (**1**), was synthesized from a facile high-yield procedure. Compound **1** crystallized as a P space group ; a = 10.5989(14) Å, b = 11.0030(15) Å, c = 16.273(2) Å, α = 91.190(2)°, β = 96.561(2)°, γ = 115.555(2)°; R = 3.50%. Thermogravimetric analysis showed **1** to produce elemental indium as a residual mass. Thermolysis in a sealed NMR tube showed carbodiimide and protonated dimethyl amine by ¹H NMR. Chemical vapour deposition experiments above 275 °C with air as the reactant gas showed **1** to readily deposit cubic indium oxide with good transparency.

5.2 Results and Discussion

Precursor synthesis

The precursor was synthesized via carbodiimide insertion into lithium dimethylamide to form the lithiated guanidinate $[(\text{Me}_2\text{N})\text{C}(\text{N}^i\text{Pr})_2]\text{Li}$ which then underwent salt metathesis with InCl_3 to produce **1** in excellent yield. The ^1H NMR spectrum of **1** contains a septet for the isopropyl methine proton, a singlet for the exocyclic amide methyl groups, and two well-resolved doublets for the diastereotopic methyl groups from the isopropyl. Our previous research has shown a range of behaviour for these isopropyl groups at different metal centres, where a single environment is found for less sterically crowded centres, and two environments are found where steric effects prevent exchange of these groups.¹¹³ Thus, the two doublets indicate a sterically crowded metal centre, as previously seen for the aluminum and gallium analogues of **1**.

In the solid state, **1** packs in a triclinic, centrosymmetric space group, $P\bar{1}$ (see Table 5.1), isostructurally with previously reported Al and Ga analogues,¹¹³ and isomorphously with Y, Gd, and Dy analogues (Figure 5.1).¹¹⁴ The indium ion displays distorted trigonal prism coordination geometry with a molecular three-fold axis of symmetry that does not coincide with any crystallographic symmetry element. Within error the bond distances and angles corresponding to chemically equivalent moieties in each of the ligands are statistically indistinguishable from each other. This is consistent to what is observed in the solution NMR. The nitrogen atoms in the exocyclic amide groups and the chelating

nitrogen atoms each exhibit planar geometry suggesting that the π system in the chelate rings extends to the exocyclic amides. However, the C–N bond lengths in the chelate rings (typically 1.33 Å) are shorter than the C–N bond length from the exocyclic amide to the bridgehead carbon (typically 1.40 Å), demonstrating that the π system resides mainly in the chelate metallocycle (see Table 5.2). This is not surprising, since the exocyclic amide groups in the ligands of **1** were rotated out of the metallocycle plane by 40.0°–47.1°. There exists a $\cos^2\theta$ relationship for the overlap of p-orbitals in such arrangements.¹¹⁵

Table 5.1 Selected crystal data and structure refinement parameters for compound **1**

Compound 1	
CCDC	815078
Formula	C ₂₇ H ₆₀ InN ₉
FW	625.66
T/K	120(2)
Crystal system	Triclinic
Space group	P
a/Å	10.5989(14)
b/Å	11.0030(15)
c/Å	16.273(2)
α/°	91.190(2)
β/°	96.561(2)
γ/°	115.555(2)
V/Å ³	1695.7(4)
Z	2
ρ (calc)/g cm ⁻³	1.225
μ/mm ⁻¹	0.726
R indices [I > 2σ]	R 1 = 0.0350 wR 2 = 0.0797
R _{int}	0.0355
Reflections collected; unique	19016; 7601

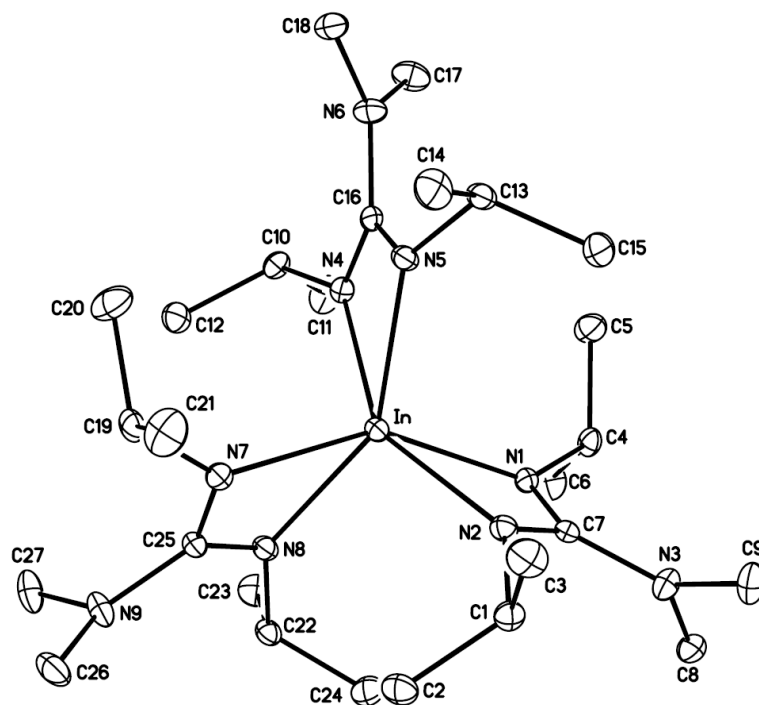


Figure 5.1 X-ray crystal structure of $\text{In}[(\text{N}^i\text{Pr})_2\text{CNMe}_2]_3$ (**1**), ellipsoids shown at 30% probability, all H atoms removed for clarity. CCDC reference number 815078. For crystallographic data in CIF or other electronic format see DOI: 10.1039/c1dt10877h.

Table 5.2 Selected bond lengths and angles for compound **1**

Selected bond lengths/Å			
In–N1	2.256(2)	N1–C7	1.333(3)
In–N2	2.255(2)	N2–C7	1.333(3)
In–N4	2.253(2)	N3–C7	1.390(3)
In–N5	2.266(2)	N4–C16	1.325(3)
In–N7	2.265(2)	N5–C16	1.332(3)
In–N8	2.266(2)	N6–C16	1.396(3)
		N7–C25	1.331(3)

N8–C25 1.326(3)

N9–C25 1.407(3)

Selected bond angles/°

N2–In–N1 59.45(7) N1–C7–N2 114.1(2)

N4–In–N5 59.30(7) N4–C16–N5 114.6(2)

N8–In–N7 59.30(7) N7–C25–N8 115.0(2)

Sum of angles/°

N1 354 ± 2 N5 354 ± 2

N2 354 ± 2 N6 360 ± 2

N3 360 ± 2 N7 354 ± 2

N4 355 ± 2 N8 355 ± 2

N9 357 ± 2

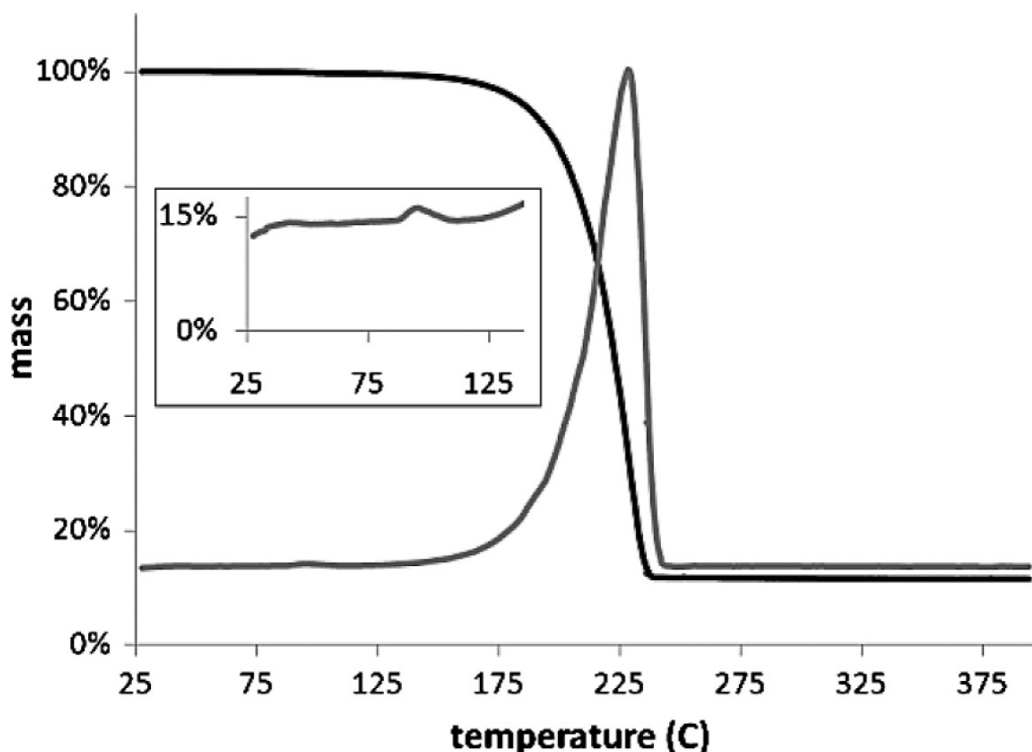


Figure 5.2 Thermogravimetric (TG) (black) and differential thermogravimetric (DTG) (gray) curves for **1**, using a heating rate of 10 °C/min. The inset shows the potential onset of thermal degradation of the precursor.

5.3 Thermolysis

Compound **1** was observed to decompose above 225 °C without melting using a bench-top melting point apparatus, and it exhibits a sublimation temperature of 150 °C at 85 mTorr. Thermogravimetric analysis of **1** revealed well-controlled thermal behaviour (Figure 5.2). Thermolysis from 28 °C to 395 °C under a nitrogen atmosphere resulted in a residual mass of 11.5%, which is well under the fractional mass of indium in **1** (18.4%). This occurred even when the ramp rate was altered (1, 2, 5, and 10 °C/min ramp rates

were tried). A flame test of the residual grey powder confirmed the presence of indium (intense indigo colour). Although the differential thermogravimetric (DTG) curve suggests a very clean sublimation, it seems that the compound undergoes both sublimation and decomposition in this region.

A thermal ^1H NMR experiment was employed where a sealed thick-walled NMR tube was subjected to increasing temperature from room temperature to $170\text{ }^\circ\text{C}$, with spectra collected at appropriate intervals. At room temperature no diisopropylcarbodiimide (CDI) was observed in the ^1H NMR spectrum of **1**. At $110\text{ }^\circ\text{C}$ signals corresponding to CDI as well as peaks for dimethyl amine were found. This onset of thermolysis may correspond to the very small peak seen in the DTG curve (inset in Figure 5.2), however there is no correlation between the mass loss in the TG and this fragment of the ligand. A more detailed thermolysis study would be required to relate these experiments to each other, and this is beyond the scope of the present study.

By $140\text{ }^\circ\text{C}$ the CDI and dimethyl amine peaks had grown further and remained in fairly constant proportion to the peaks for **1** up to $170\text{ }^\circ\text{C}$, and a precipitate was apparent in the NMR tube. This suggests that free guanidine was produced and subsequently decomposed to CDI and amine. This has been seen at similar temperatures with a copper guanidinate.¹¹⁶ This is interesting since all of these data suggest that **1** will undergo thermal decomposition and might deposit indium oxide quite easily using air as an oxygen source. More experimental work is ongoing to better understand the mechanism.

5.4 Film depositions and characterization

When **1** was used as a CVD precursor, it was found to deposit indium oxide using air or 10% O₂ in N₂ as the reactant gas. Indium metal, reduced by the ligand, was deposited under vacuum with no reactant gas. The deposition in both cases needed to occur above 275 °C to show significant film growth, and so the deposition of indium metal was difficult to quantify; at that temperature indium metal is liquid and did not remain on the substrate. Thus, only the deposition of indium oxide was explored in depth. Interestingly, the onset of growth is lower than has been typically seen for CVD of indium oxide.^{21–24}

When the deposition was undertaken at 350 °C using **1** as the precursor and air as the reactant gas (Table 5.3, runs **a–h**), crystalline cubic indium oxide was formed, giving a lattice parameter of 10.120 Å (acquired by Rietveld refinement using MAUD software¹¹⁷) while the value in PDF card 6-416 is 10.118 Å. (Figure 5.3). It was also interesting to note that crystalline indium metal could be detected by XRD in run **g**. Modelling the integration of the indium metal peaks against the peaks of indium oxide showed that this impurity was present in 1–2% abundance. This suggests that **1** thermally decomposed to a reduced indium state, and then likely re-oxidized in air to produce indium(III) oxide. This supports the thermolysis experiments presented above. An X-ray photoelectron spectrum (XPS) of the film supported the characterization of the film as indium oxide (Figure 5.4), and energy dispersive X-ray (EDS) showed both indium and oxygen (as well as silicon from the substrate) to be present in the film. The XPS spectra were calibrated using the C 1s peak as a reference, setting it to 284 eV. The oxygen signal consisted of two

components, which show oxygen in In_2O_3 (the peak at 531.8 eV), and a more easily ionized oxygen (at 530.4 eV), which may be due to i) oxygen at the silicon interface, ii) oxygen as hydroxyls at the surface, or iii) oxygen in amorphous In_2O_3 .¹¹⁸ Since the O:In ratio was found to be close to the stoichiometric value at 1.43, we suspect that the 530.4 eV peak is due to amorphous In_2O_3 . The slightly low ratio is presumed to be due to oxygen vacancies. Carbon and nitrogen were not detected by XPS, thus indicating negligible inclusion of these impurities from the ligand.

Table 5.3 The various deposition runs undertaken using different masses of **1** as the precursor and air as the reactant gas.

run	<i>T</i>/°C	precursor mass/g	time/min	thickness/nm
a	350	0.107	25	105
b	350	0.209	25	141
c	350	0.479	15	249
d	350	0.489	17.5	273
e	350	0.49	20	366
f	350	0.488	22.5	621
g	350	0.48	25	615
h	300	0.479	15	250

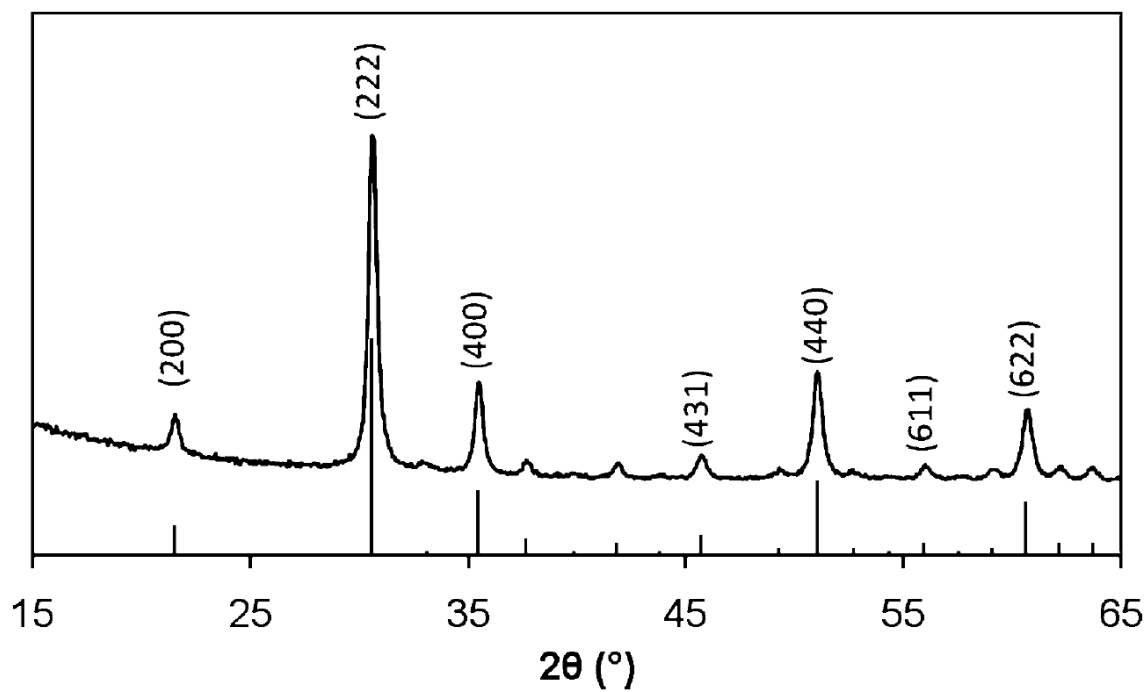


Figure 5.3 The X-ray diffractogram of the film deposited in run **b**. The vertical lines indicate the expected diffraction peaks for cubic indium oxide.

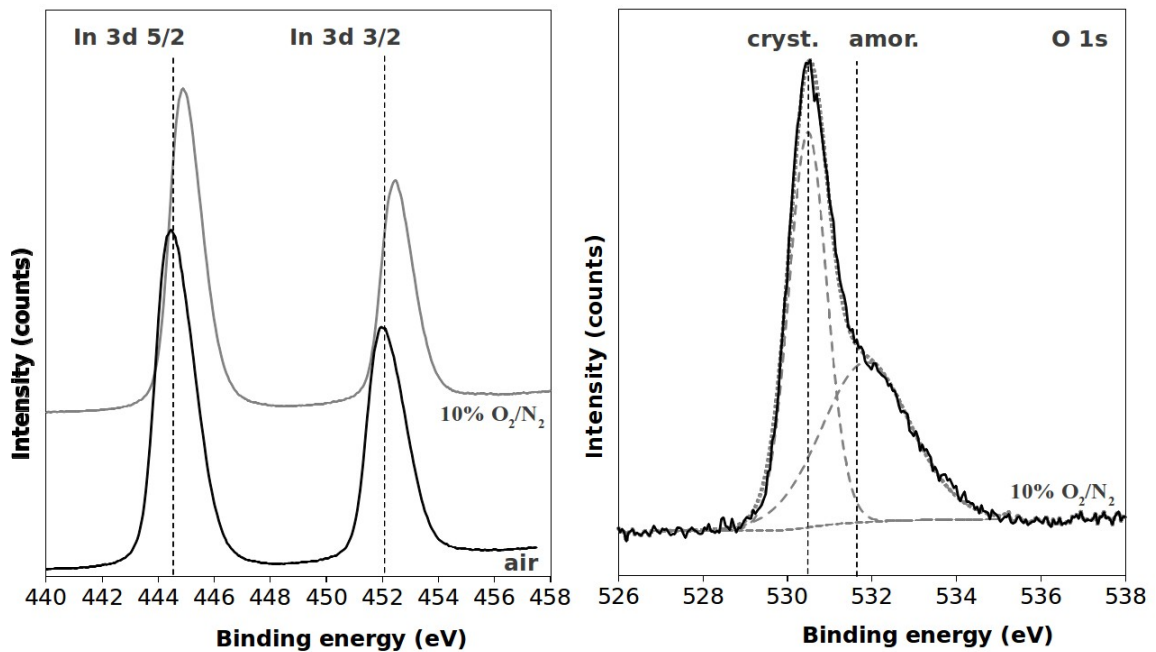


Figure 5.4 Narrow XPS spectra for indium 3d and oxygen 1s signals from run **b**. Values from the literature for the location of the elemental signals are shown and the two components used to fit the O 1s signal are indicated with dashed lines.^{156,157} The oxygen signals due to crystalline and amorphous material are labelled as such. Indium signals were fitted using only one component per peak.

We expect that the amorphous indium oxide grew as the CVD apparatus ramped to the deposition temperature, with crystalline indium oxide growing at the deposition temperature. This is supported by the XPS data above, and by the variable temperature XRD in Figure 5.8. A scanning electron micrograph (SEM) showed the indium oxide to be continuous and uniform, and also corroborated ellipsometry thickness measurements (Figure 5.5).

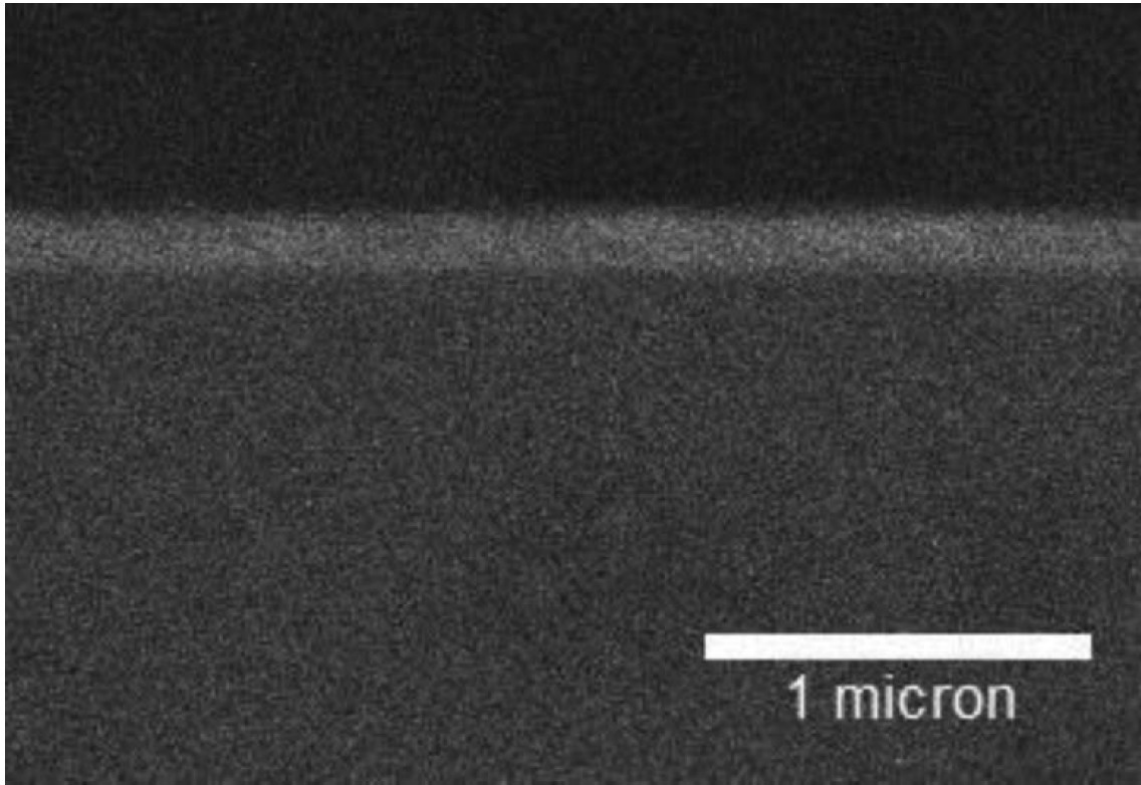


Figure 5.5 A side-on SEM of the indium oxide film deposited in run **b**.

Due to the construction of our CVD apparatus, the precursor can volatilize as soon as the furnace starts to ramp to the deposition temperature and air (as the reactant gas) is always flowing at a base pressure of 250 mTorr (Figure 5.6). The pressure of precursor can be seen to increase starting at about 275 °C, where the reactor pressure increased above the baseline pressure of air (as measured in the deposition region, this corresponded to about 150 °C at the precursor boat). Thus, early amorphous deposition occurs at a slightly lower temperature than the targeted process temperature, since there is a period of 2 min where the precursor is volatilizing before the temperature ramp is complete.

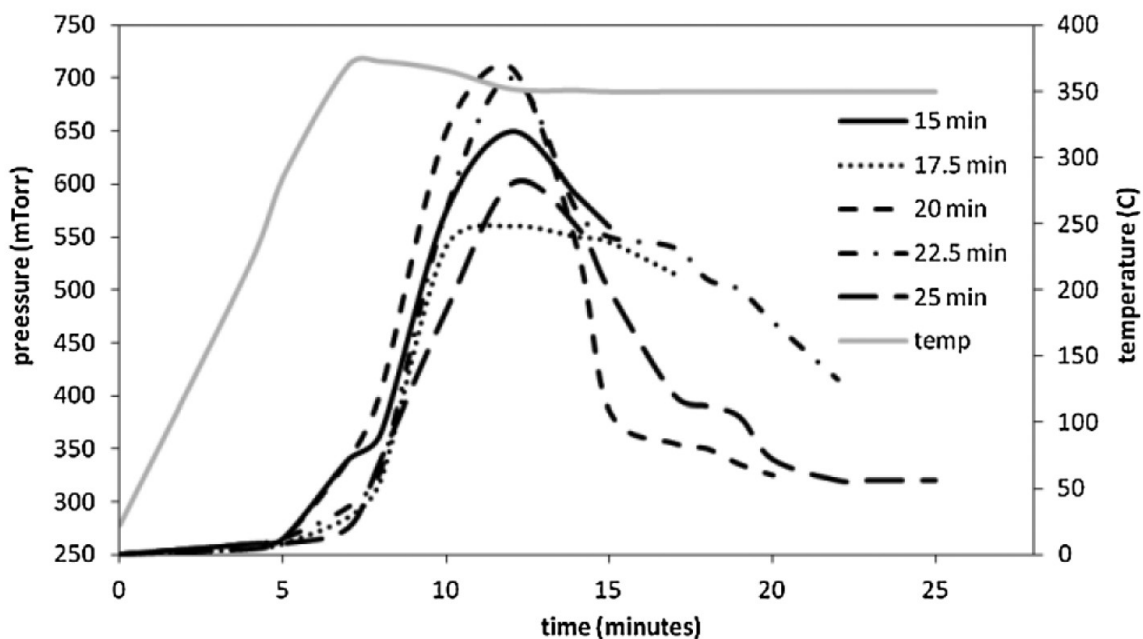


Figure 5.6 Total pressure in the CVD reactor for runs **c–g**, with the temperature profile (common to all runs) shown in light grey.

The films all showed similar, excellent transparency, as typified by the film deposited in run **b**, with absorbance below 5% over the range of 450–800 nm and a small tail of absorbance rising to about 7% at 400 nm (Figure 5.7). The initial two 25 min depositions **a** and **b** each showed complete depletion of precursor, accounting for their low growth rates. Thus, five depositions using about 0.48 g of precursor were run between 15 and 25 min with a deposition temperature of 350 °C. The growth rate of the indium oxide film from this series of depositions was 43 nm min⁻¹ (Table 5.3, runs **c–g**), wherein the precursor was not fully depleted. Although the range of literature growth rates for indium oxide deposition by CVD is large, this value is at the high end of that range (5–43 nm min⁻¹).^{21–24} Among these five runs the thickness data was not very linear, with a

coefficient of determination (R^2) of 0.88. However, this variance in thickness could be due to a variance in the amount of crystalline versus amorphous indium oxide. The films from this series of depositions were measured to have resistivities of 21.0–117.1 Ω cm using a four-point probe measurement. Contrary to expectations the resistivities generally increased with film thickness, possibly due to a larger amount of amorphous material.

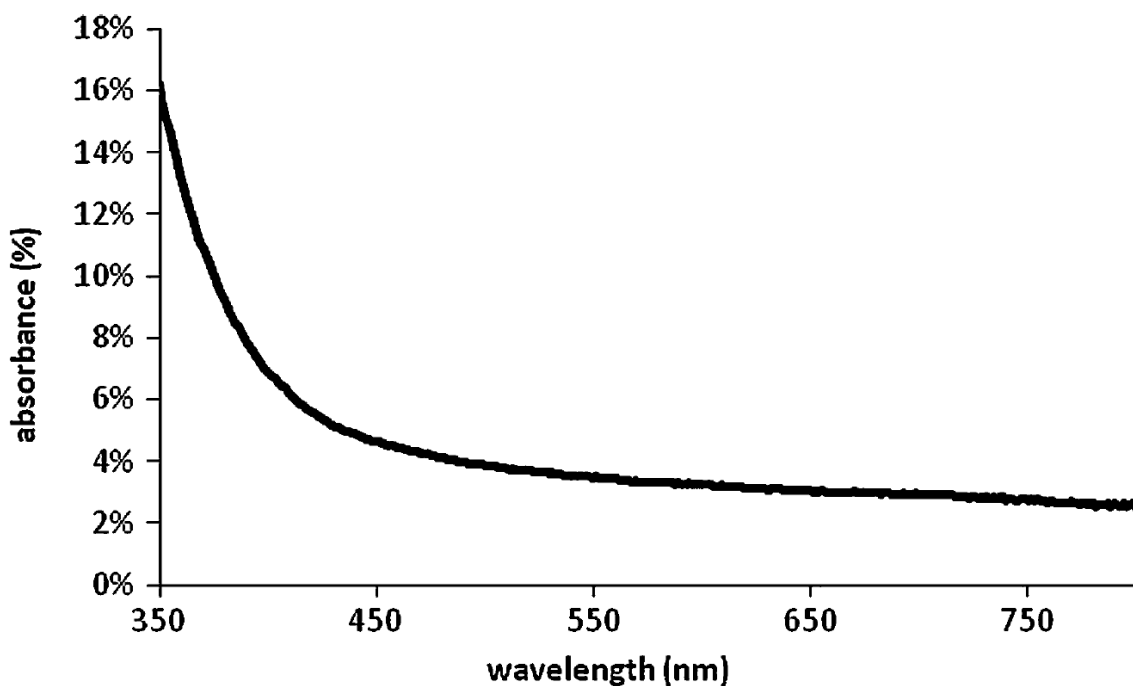


Figure 5.7 A UV-Vis difference spectrum where the absorbance of a bare borosilicate glass slide has been subtracted from the absorbance of the same slide coated with In_2O_3 (run **b**).

A broad peak was seen in the background of the XRD for run **a**, centered at approximately 32° . Upon annealing to 1175°C in air, this broad feature disappeared and the XRD showed only cubic indium oxide. This supports the existence of an amorphous indium oxide phase, as seen in the XPS for run **b**.

The growth of amorphous indium oxide was confirmed when a run was undertaken using a deposition temperature of 300 °C (Table 5.3, run **h**), and only the amorphous feature was seen by XRD (Figure 5.8). In order to unambiguously identify this as indium oxide, a high-temperature X-ray diffraction (HTXRD) experiment was undertaken in vacuum. Indeed, In_2O_3 started to appear at 275 °C, and these peaks then started to decrease at around 500 °C as it started to thermally convert to In_2O and volatilize.¹¹⁹ The film was entirely volatilized away by 875 °C.

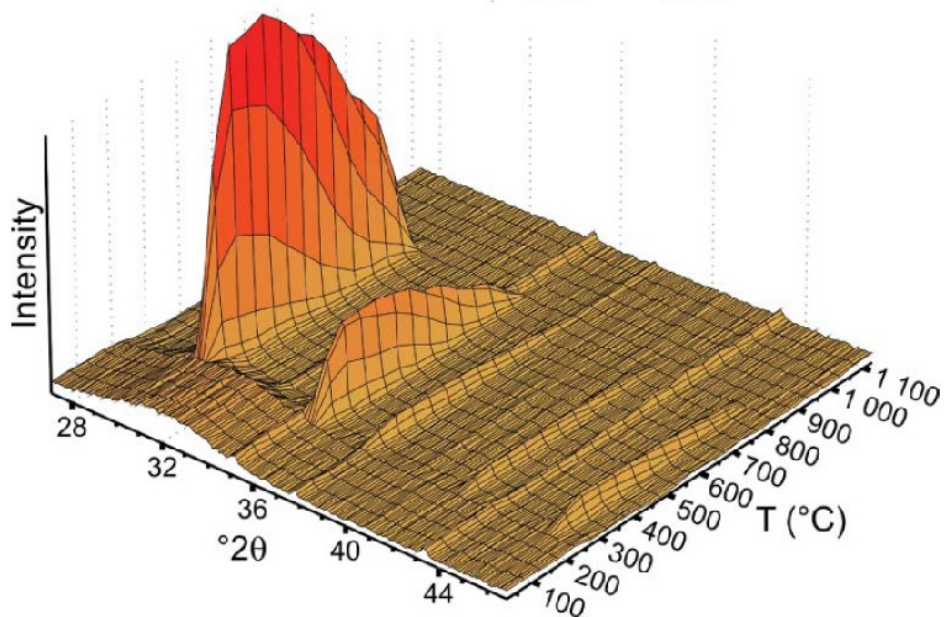
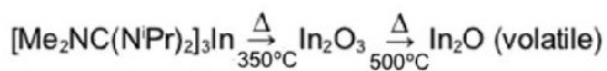
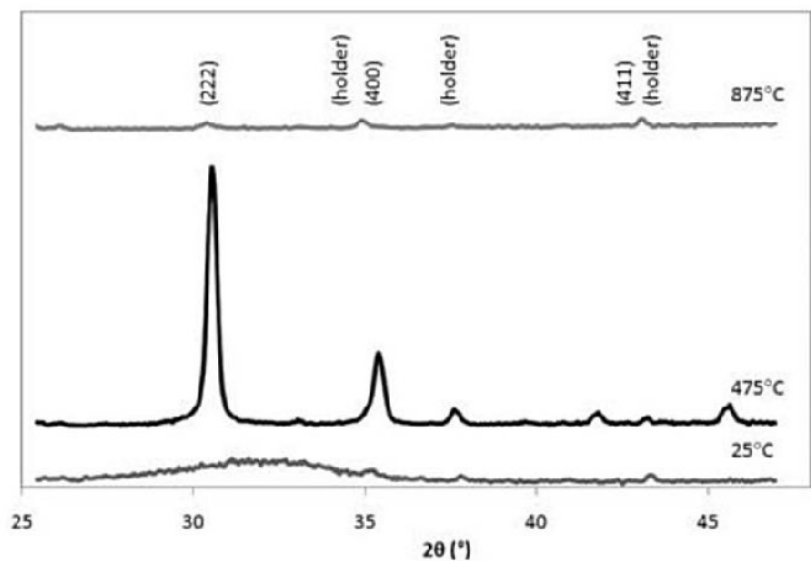


Figure 5.8 HTXRD measurement of the crystallization of cubic In_2O_3 under vacuum from a film deposited at 300°C (run **h**). The three-dimensional plot shows the evolution of the peaks for cubic indium oxide as a function of temperature. Weak reflections observed at room temperature and at the highest temperature originate from the sample holder.

5.5 Experimental

General procedures

All manipulations were done in an MBraun nitrogen-filled drybox. 1,3-diisopropyl carbodiimide, lithium dimethyl amide, indium trichloride, and deuterated benzene were purchased from Aldrich and used as received. Anhydrous grade THF was purchased from Aldrich and used as received. The solvents ether and hexane were reagent grade and were purified using an MBraun solvent purification system. The ^1H and ^{13}C NMR spectra were collected on a Bruker Ultra Shield 300 MHz spectrometer using the residual protons in the deuterated solvent for reference. X-ray photoelectron spectra were collected using a Kratos Analytical Axis Ultra, with a monochromated Al K-alpha X-ray source at a power of 140 watts. Film crystallinity and phase were determined using a PANalytical X'Pert Pro MPD diffractometer (Cu-K α -radiation, $\lambda = 1.5419 \text{ \AA}$) in a grazing incidence mode. High temperature (HTXRD) measurements were conducted in an Anton-Paar HTK1200N oven under $<10^{-4}$ mbar vacuum. Electron microscopy was performed using a TESCAN VEGA-II XMU Variable Pressure Scanning Electron Microscope with an Oxford Instruments INCAx-act Energy Dispersive X-ray spectrometer. The XPS was performed on a Kratos Axis DLD XPS system, using a monochromated 150 W aluminum anode as the source.

In[(*N*^{*i*}Pr)₂CNMe₂]₃ (**1**)

In a large vial 1,3-diisopropyl carbodiimide (1.9 g, 15 mmol) was diluted in about 3 mL of ether and chilled in a –30 °C freezer for 30 min. In a 50 mL flask lithium dimethyl amide (0.81 g, 15 mmol) was dissolved in approximately 10 mL of ether with stirring. To this solution the chilled diluted carbodiimide was slowly added and the solution was allowed to stir for three hours.

In a 50 mL flask indium trichloride (1.13 g, 5 mmol) was allowed to dissolve in about 10 mL of THF with stirring. To this solution the lithium guanidinate solution was added slowly and allowed to stir overnight. The solvent was removed under vacuum and the resultant product was dissolved in about 30 mL of hexane and stirred overnight. The solution was then filtered to remove LiCl and then put under vacuum to remove solvent, causing a white precipitate to crash out of solution. The white precipitate was dissolved in about 20 mL of hexane and then cooled to –30 °C overnight. Compound **1** precipitated as clear cubic crystals (2.51 g, 78.0%). Decomposes above 225 °C. ¹H NMR (300 MHz, C₆D₆): δ 3.77 [sept, 6H, CH(CH₃)₂], 2.66 [s, 18H, N(CH₃)₂], 1.49 (d, 18H, CH(CH₃)₂), 1.35 [d, 18H, CH(CH₃)₂]. ¹³C NMR (75 MHz, C₆D₆): δ 167.46 [NCN], 47.16 [CH(CH₃)₂], 40.17 [N(CH₃)₂], 26.55 [CH(CH₃)₂], 25.64 [CH(CH₃)₂]. Combustion analysis; found (calculated), C: 52.02% (51.81%), H: 9.61% (9.67%), N: 20.44% (20.15%).

Single crystal X-ray diffraction

A data crystal was selected and mounted on a glass fiber using viscous oil flash-cooled to the data collection temperature. Data were collected on a Bruker-AXS APEX CCD diffractometer with graphite-monochromated Mo-K α radiation ($\lambda = 0.71073 \text{ \AA}$). Unit cell parameters were obtained from 60 data frames, $0.3^\circ \omega$, from three different sections of the Ewald sphere. No symmetry higher than triclinic was observed and solution in the centrosymmetric space group option yielded chemically reasonable and computationally stable results of refinement. The data-set was treated with SADABS absorption corrections based on redundant multiscan data. The structures were solved using direct methods and refined with full-matrix, least-squares procedures on F^2 . All non-hydrogen atoms were refined with anisotropic displacement parameters. All hydrogen atoms were treated as idealized contributions. Atomic scattering factors are contained in the SHELXTL 6.12 program library.¹²⁰

Chemical vapour deposition

All CVD experiments were performed in a home built low pressure CVD apparatus using ultra high purity nitrogen as both a carrier and purge gas (Figure 5.9). Silicon (100) slides were cut and then cleaned by first sonicating in acetone followed by a piranha etch/UVO process to grow a clean hydroxide layer on the slides. The slides were then allowed to dry and stored in an oven until use.

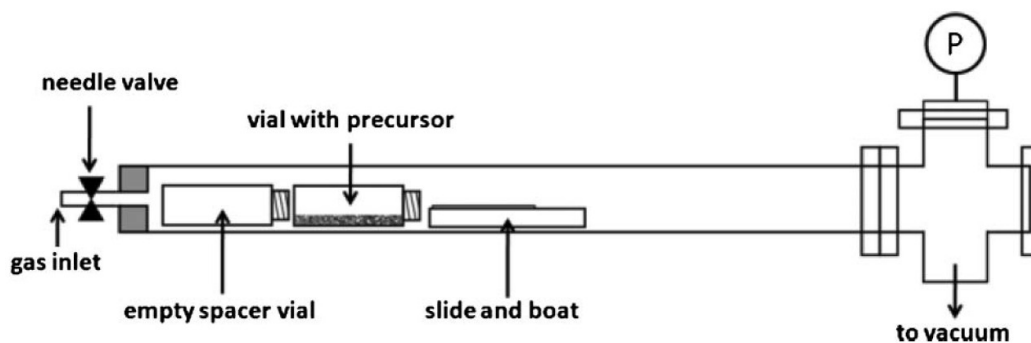


Figure 5.9 CVD apparatus used for the deposition of indium oxide from **1** and air.

*CVD of In_2O_3 with **1** and air*

An aluminum boat was used to hold the silicon (100) substrates (approximately 1 cm by 3 cm) prepared as above. The boat was placed in the furnace of the apparatus behind both a “spacer” vial which served to position the boat in a better position with respect to temperature, and a second vial which contained compound **1**. Depositions were carried out at 350 °C, with precursor masses of 0.107 g, and 0.209 g. The duration of each run was measured from the moment the furnace was turned on and lasted 25 min. Prior to engaging the furnace, the pressure of the system was set to 250 mTorr by adjusting a needle valve to admit ambient air. The slides were allowed to cool to room temperature under atmosphere in the furnace. The resultant highly reflective, mainly blue thin films were analyzed for composition by X-ray diffraction and XPS .

A second series was performed using the same arrangement as above to determine the growth rate. Trial times were 15, 17.5, 20, 22.5 and 25 min and masses were close to 0.48 g of precursor, with the same deposition temperature as above. The duration of each run

was measured from the moment the furnace was turned on and ended with the immediate removal of the slide from the furnace. The slide was then allowed to cool on the benchtop under atmosphere.

A third deposition was performed using the arrangement above to determine the crystallinity of the film at lower deposition temperature. The trial time was 15 min and the mass of **1** was 0.479g. The deposition temperature was 300 °C and the duration of the run was measured from the moment the furnace was turned on and ended with the immediate removal of the slide from the furnace. The slide was then allowed to cool on the benchtop under atmosphere.

5.6 Conclusions

$\text{In}[(\text{N}^i\text{Pr})_2\text{CNMe}_2]_3$ (**1**) was easy to synthesize, recrystallize, and sublime with excellent yields. Although it was stable to sublimation at 150 °C at 85 mTorr, it was found to eliminate protonated guanidine when sitting in an inert atmosphere for extended periods of time. Additionally, it was found to produce diisopropylcarbodiimide and dimethylamine when heated to 140 °C as a solution in deuterated benzene.

Thermogravimetric analyses suggested that **1** decomposed to indium metal in an inert atmosphere, and this was corroborated by vacuum CVD experiments without a reactant gas at temperatures above 275 °C.

When air was used as a reactant gas in a CVD experiment above 275 °C, the compound was found to produce transparent indium oxide. When 325 °C was used, the films were found to be crystalline, cubic indium oxide, and occasionally had a small impurity of indium metal. This suggests a film growth mechanism where indium undergoes reduction and is then re-oxidized to In_2O_3 .

Chapter 6 - Metallic Silver and Gold Chemical Vapour Deposition from

Novel Precursors

Results presented below have been submitted in a separate, original manuscript to Chem. Mater. in July 2013 as:

“Thermally Robust Gold and Silver Iminopyrrolidines for Chemical Vapour Deposition of Metal Films”

Jason P. Coyle^{1*}, Peter G. Gordon¹, Adam P. Wells¹, Eric R. Sirianni², Glenn P. A. Yap², Seán T. Barry¹

¹ Department of Chemistry, Carleton University, 1125 Colonel By Drive, Ottawa, K1S 5B6, Canada

² Department of Chemistry & Biochemistry, University of Delaware, Newark, Delaware 19716, USA

6.1 Abstract

Dimeric silver(I) and gold(I) tert-butyl-imino-2,2-dimethylpyrrolidines were synthesized and evaluated for thermal stability by thermal gravimetric analysis (TGA), differential scanning calorimetry (DSC) and variable-temperature solution NMR. Subsequently these compounds were used to deposit metallic films on silicon and glass substrates by chemical vapour deposition (CVD), with and without a flow of heated nitrogen gas. A previously reported analogous copper(I) compound with excellent thermal properties motivated this investigation and is used for comparison. The present compounds decomposed to produce metallic films at 140 °C for the silver compound and 300 °C for the gold compound in CVD experiments under roughing pump vacuum. Additional CVD experiments with heated nitrogen gas flow improved film uniformity

without sacrificing film purity. The deposition and characterization of metallic silver and gold films from these precursors is reported here.

6.2 Introduction

Longstanding research interest regarding the preparation of thin metallic films of Cu, Ag, and Au has been rapidly increasing over the past few decades. Each of these metals possess extremely low resistivities (and gold is highly resistant to corrosion) and so these elements are often employed as interconnects in microelectronics. Plasmonic effects, particularly the surface plasmons of these coinage metals¹²¹ are well known and research into their implementation in photonic devices is rapidly increasing.¹²² As electronic devices shrink, so to do their circuits. Processes that can create metallic architectures with decreasing feature size and increasing precision are required to move forward. Chemical vapour deposition¹²³ (CVD) and atomic layer deposition⁴² (ALD) for thin film deposition are becoming routine in industry for a wide variety of materials as they are ideal technologies for coating geometrically complex substrates with high aspect ratio features.¹²⁴ An understanding of the thermal behaviour of the precursors used to create these thin films is required for precise process control and innovation in precursor design.

Many examples of Cu(I) and Cu(II) homoleptic compounds have been reported for both ALD and CVD copper thin film processes including β -diketonates,^{125,126} β -diketiminates,¹²⁷ amidinates,^{128–131} guanidinate,¹³² aminoalkoxides¹³³ and

pyrrolylaldiminates.¹³⁴ Reports of homoleptic precursors for silver and gold are less common, which may be attributed at least in part to the larger ionic radii of silver and gold compared to copper. As there is more space for coordination, non-volatile oligomers or polymers of silver(I) and gold(I) are often obtained, frustrating the search for appropriate gas-phase precursors.¹³⁵ Perhaps mainly due to cost concerns, industry tends to select for copper precursors for interconnects in microchip fabrication whereas silver and gold thin films have remained primarily an academic pursuit. This may change, as recently a previously known CVD precursor for silver films has been re-investigated and employed as a plasma enhanced-ALD precursor¹³⁶ for use in surface-enhanced Raman spectroscopy (SERS) applications.¹³⁷⁻¹⁴⁰ Also, a gold guanidinate¹⁴¹ CVD precursor has been used to coat fibre optics as part of a plasmonic device platform.^{142,39} The potential of these applications may outweigh their cost.

There exist only a few reports in the literature of ligands for which a complete series of copper, silver, and gold compounds have been prepared and their characteristics compared.¹⁴³⁻¹⁴⁵ While copper amidinates are well-known precursors for ALD,¹²⁸ silver and gold amidinates volatilize and decompose within the same temperature range. Alkyl substituted guanidinate compounds (Figure 6.1) have shown similar behaviour and have been used as CVD precursors in custom built reactors.^{132,141}

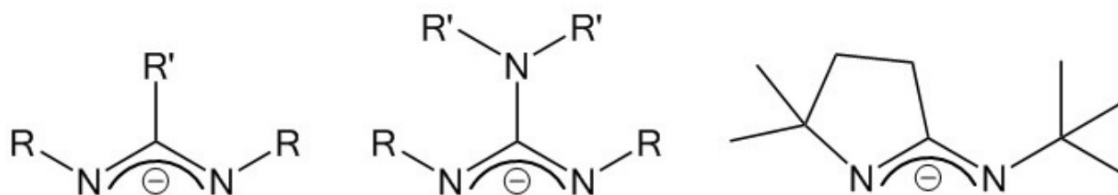


Figure 6.1 Amidinates, guanidates, and iminopyrrolidates ligands used in precursors for CVD and ALD (R, R' = any alkyl group).

Recently, our group has studied the thermolysis mechanisms of a copper(I) amidinate¹⁴⁶ and a guanidinate¹¹⁶ in the gas phase. These compounds can undergo β -hydride elimination during decomposition producing metallic films. As described previously in Chapter 1, altering the amidinate by replacing the β -hydrogen atoms with methyl groups and incorporating a ring to prevent deinsertion^{116,147} affords an exceptionally stable, volatile copper compound.¹⁴⁸ Herein, we present the analogous silver(I) and gold(I) compounds and report on their thermal stability and results from CVD experiments.

6.3 Results and Discussion

Dimeric silver(I) and gold(I) tert-butyl-imino-2,2-dimethylpyrrolidates (compounds **1** and **2**, respectively) were generated by salt metathesis of lithium tert-butyl-imino-2,2-dimethylpyrrolidate and a metal chloride salt (Figure 6.2). The isolated compounds are air stable, insoluble in nonpolar solvents, unstable in polar solvents, and soluble in benzene, toluene or methylene chloride. The ¹H NMR spectra of **1** and **2** in C₆D₆ were simple to interpret and indicate a single chemical environment. Compound **2** could also be measured in CDCl₃ and **1** decomposed immediately in CDCl₃. Compounds **1** and **2**

share an isomorphous dimeric structure with the previously reported analogous copper compound¹⁴⁸ (**3**) in the monoclinic $P2_1/c$ space group with two molecules in the unit cell each located on inversion centres (Figure 6.3, Table 6.1). The metal-metal distances are similar to previously reported dimeric amidinates, at 2.677(3) Å and 2.6801(4) Å for Ag and Au, respectively.^{131,141} In both structures, the metal ions deviate from the planar metallocycle core bending the N–M–N ideally linear geometry by $\sim 9^\circ$. The C–N bonds around the central carbon atom range from 1.32 Å – 1.34 Å, which correlates well to the expected delocalized bond character within the iminopyrrolidinate. The asymmetry in the steric bulk of the ligand leads to a distortion in the arrangement of the four nitrogen atoms in the dimeric molecular core, forming a parallelogram that deviates from an ideal rectangle by $4.9(2)^\circ$ for **1** and $3.8(2)^\circ$ for **2**.

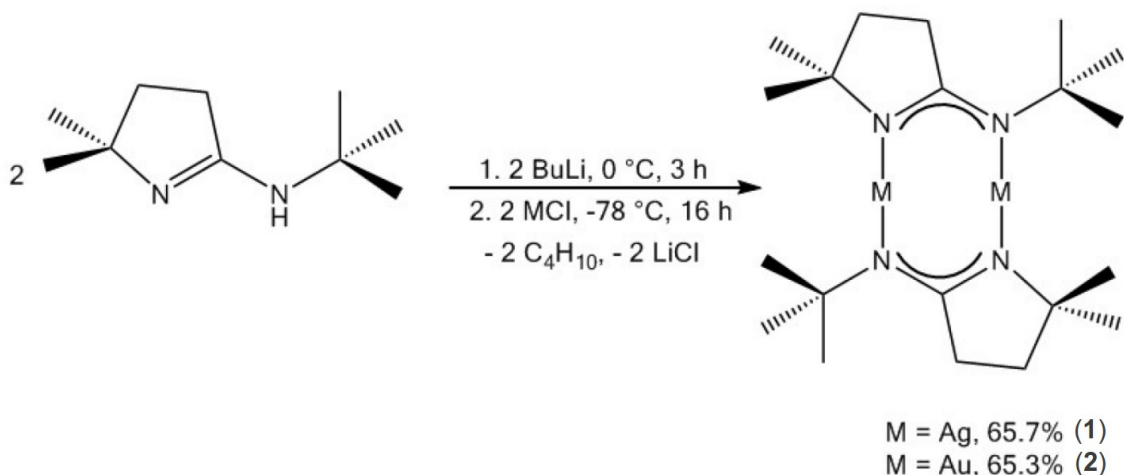


Figure 6.2 Synthesis of silver(I) and gold(I) tert-butyl-imino-2,2-dimethylpyrrolidinate.

Compound 1		Compound 2	
Selected bond	Length (Å)	Selected bond	Length (Å)
Ag - Ag	2.68	Au - Au	2.68
Ag - N1	2.08	Au - N1	2.03
Ag - N2	2.10	Au - N2	2.05
N1 - C4	1.32	N1 - C4	1.34
N2 - C4	1.32	N2 - C4	1.33
Compound 1		Compound 2	
Selected angle	Angle (deg)	Selected angle	Angle (deg)
N1 - Ag - N2	170.43	N1 - Au - N2	170.89
N1 - C4 - N2	123.61	N1 - C4 - N2	124.70

Table 6.1 Selected bond lengths and angles for 1 and 2.

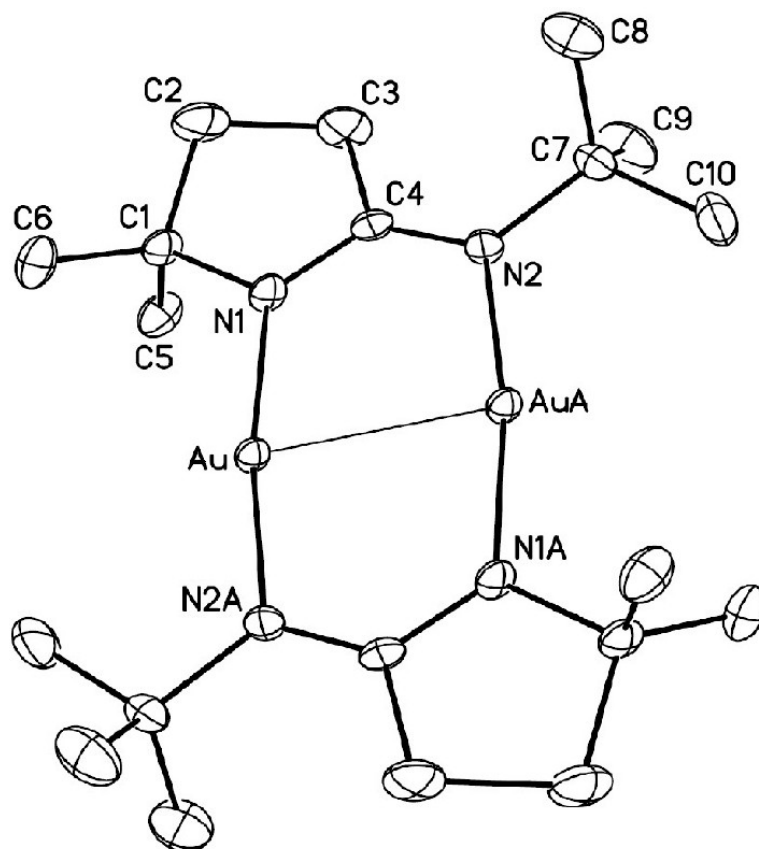


Figure 6.3 Molecular diagram of **2** with thermal ellipsoids at 30% probability. Hydrogen atoms omitted for clarity. Ag analogue compound **1** is isomorphic with **2**.

TGA of **1** and **2** showed weight loss curves with a single feature, indicating clean volatilization, and residual masses lower than the amount of metal contained in the sample. Equal molar amounts of **1** and **2** were heated under identical conditions and compared (Figure 6.4). The onset of mass loss (0.5 % weight loss) for **1** was 172 °C and 209 °C for **2**. Powder X-ray diffraction (P-XRD) analysis of the residual masses from **1** and **2** showed peaks matching those for metallic phases, showing that a large percentage

of metal was indeed volatilized and indicating promising volatile compounds that thermally decompose at high temperatures ($> 170\text{ }^{\circ}\text{C}$) to produce metal.

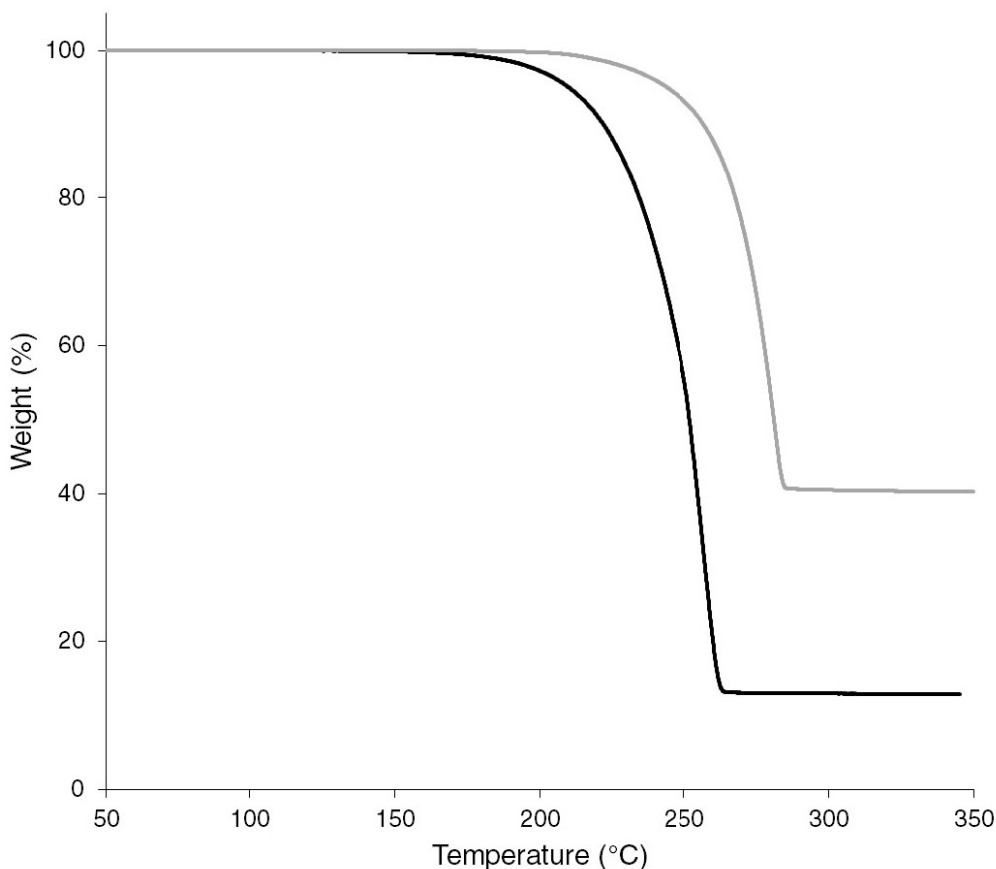


Figure 6.4 Thermogravimetric analysis of **1** (black) and **2** (gray). Experiments were run under 1 atm nitrogen with a ramp rate of $10\text{ }^{\circ}\text{C}/\text{min}$. Sample size for **1** and **2** were 10.49 mg and 13.65 mg, respectively. Note that the maximum percentage residual mass of pure metal for **1** and **2** would be 39.35 % and 54.23 % respectively.

Isothermal TGA experiments were performed to assist in separating the volatilization and decomposition events that were observed during thermal ramping experiments.

Isothermal data for **2** at $210\text{ }^{\circ}\text{C}$, $230\text{ }^{\circ}\text{C}$, and $250\text{ }^{\circ}\text{C}$ (Figure 6.5, b) yielded lower residual masses of 18 %. This indicates that the change in the rate of evaporation exceeds any

increase in the rate of decomposition that may be occurring at higher temperatures, suggesting a good range of thermal stability and a very promising thin film precursor. For **1**, isothermal data at 180 °C, 210 °C, and 240 °C yielded residual masses of 7 %, 6%, and 17%, respectively (Figure 6.5, a). Comparison of the TGA isotherms of **1** and **2** highlights **2** as the more thermally robust compound. The residual mass of **2** remains essentially unchanged over the range of temperatures studied, demonstrating stability.

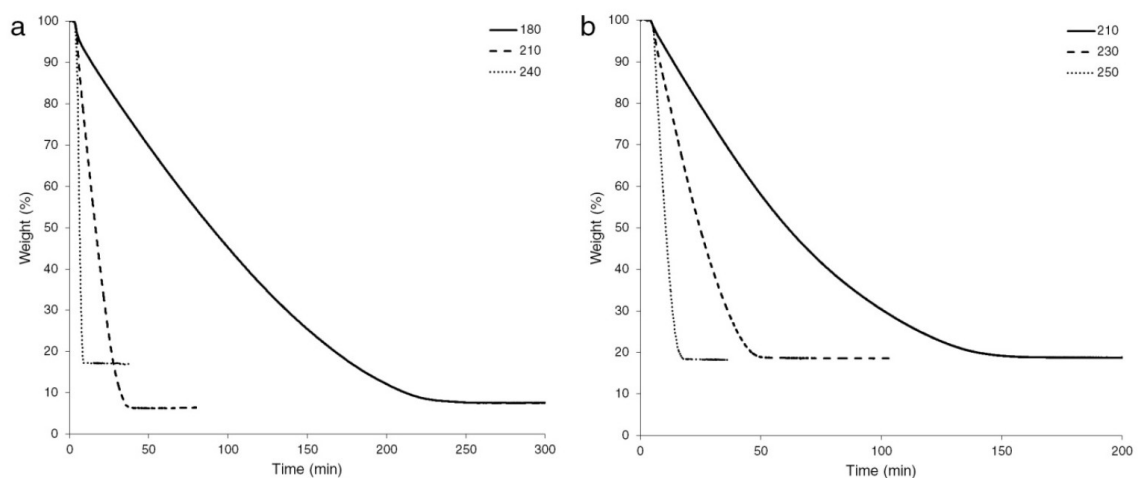


Figure 6.5 Isothermal TGA of (a) **1** and (b) **2**. Isothermal temperatures, indicated in the right hand legend (°C), were reached at a rate of 40 °C/min. Sample sizes were between 3.10 mg and 3.67 mg.

Differential scanning calorimetry (DSC) experiments were also performed to study the thermal decomposition of **1** and **2**. Figure 6.6 shows DSC traces of **1** and **2** with exothermic events (upwards on the trace) which are consistent with decomposition. Compound **1** shows an onset for decomposition at 180 °C with a slow, irregular climb to a peak maximum at 253 °C. A sharper decomposition event at 290 °C was observed for compound **2**. A small endothermic valley in the broad decomposition peak at 248 °C for **1**

may be attributed to a melting event. Copper(I) tert-butyl-imino-2,2-dimethylpyrrolidinate (**3**) was included in the DSC analysis for comparison across the coinage metals. Compound **3** showed endothermic events at 243 °C and 260 °C which were repeatable upon sample cooling and reheating and are attributed to melting and boiling points, respectively. By contrast, the exothermic events for **1** and **2** were not repeatable, again indicating decomposition processes.

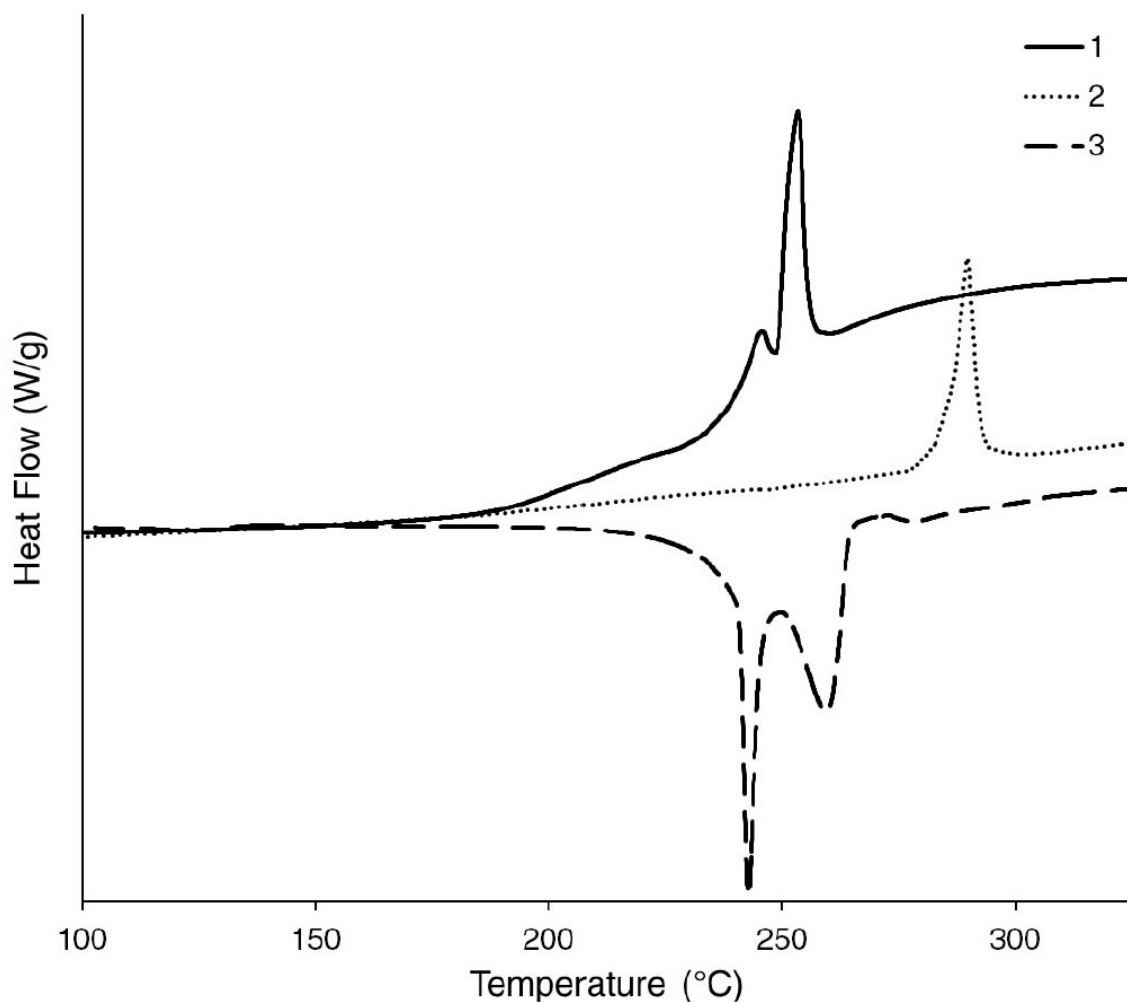


Figure 6.6 Differential scanning calorimetry of **1**, **2**, and **3** in hermetically sealed aluminum pans. Temperature ramp was 10 °C/min up to 325 °C. Sample masses were 1.066 mg, 1.625 mg, and 3.790 mg for **1**, **2**, and **3**, respectively. Exotherms are up.

The evaporation kinetics of **1** and **2** were evaluated by stepped isothermal TGA between 130 °C – 190 °C (Figure 6.7). Lower temperatures were evaluated as this minimizes mass loss due to decomposition. Both compounds presented evaporation rates with Arrhenius temperature dependence. The expected higher rates of evaporation for compounds of lower molecular mass (as compared to **3**) was observed. While

iminopyrrolidines typically demonstrate decreased volatility when compared to acyclic amidines and guanidines, largely due to their planar molecular structure,¹⁴⁹ bulky substituents and rings decrease vibrational freedom which leads to a more rigid molecule. These features of the iminopyrrolidines presented here sufficiently increase thermal stability to permit volatilization at higher temperatures while avoiding decomposition. From the isothermal TGA and using the Langmuir equation,¹⁵⁰ the temperature at which 1 torr of vapour pressure could be obtained was estimated to be 206 °C and 225 °C for **1** and **2**, respectively.

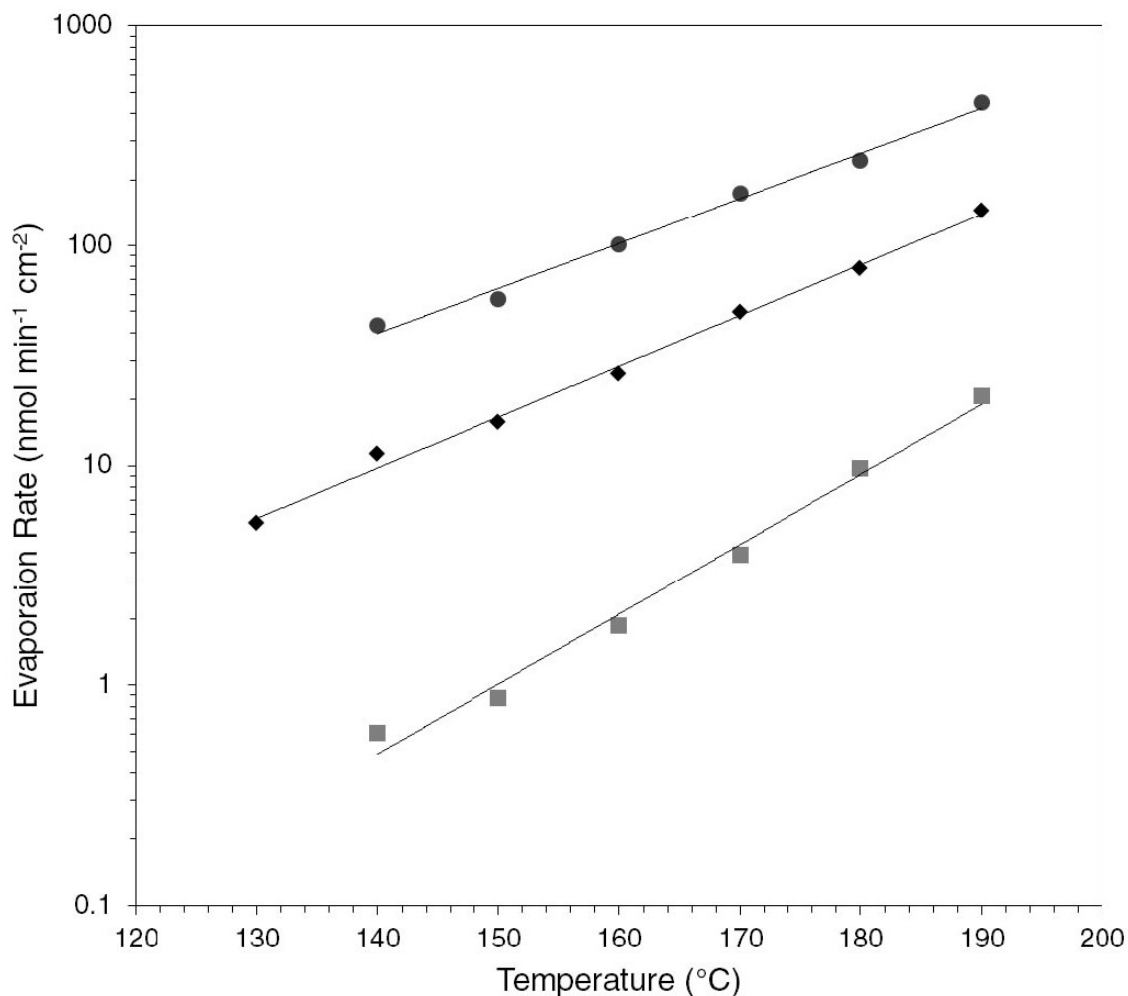


Figure 6.7 Evaporation kinetics of **1** (◆), **2** (■) and **3** (●).

Decomposition mechanisms were studied by NMR: solutions of **1** and **2** in C₆D₆ were sealed in heavy walled NMR tubes and heated in an isothermal oven equipped with a light bulb – the 2.5 ppm methylene peak in the ¹H NMR spectra was measured daily to track decomposition rates and products. For each compound, two tubes were prepared: one tube was exposed to light and one was kept in darkness for the extent of the experiment. The only distinguishing feature of these two conditions were that the

solutions exposed to light completely decomposed in less time, which was most apparent near the end of the experiments. Under both light and dark conditions, compound **2** decomposed at 100 °C whereas **1** showed negligible decomposition at 100 °C and instead required a temperature of 120 °C to decompose within the same time frame as **2** (Figure 6.8). The decomposition of both compounds resulted in a metallic mirror plating out on the tube walls. A rate order could not be assigned unambiguously to any of the decomposition trends as each trend showed similar fits to zero, 1st and 2nd order plots. This ambiguity in rate analysis suggests a complex decomposition mechanism which may involve both surface and solution based reactions. Interestingly, protonated ligand was the only decomposition product observed by ¹H NMR for each experiment.

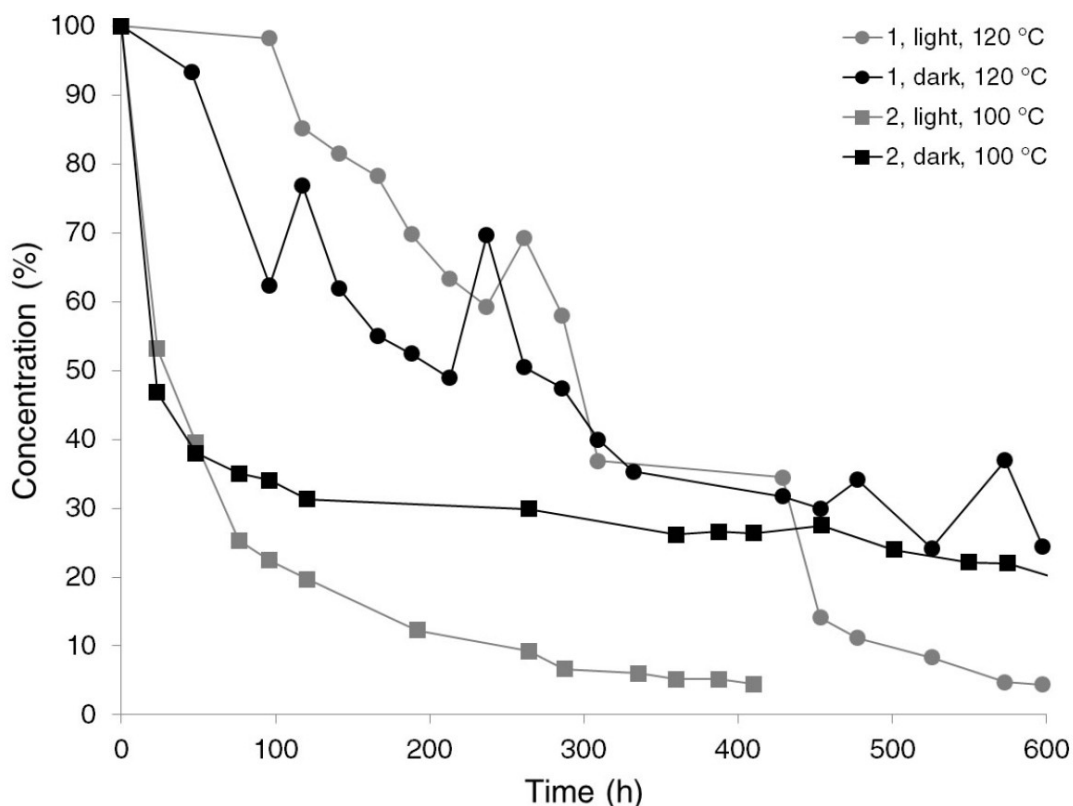


Figure 6.8 Decomposition of **1** and **2** in solution (C_6D_6) measured by 1H NMR.

While the mechanism of decomposition for these compounds remains unclear, the results are consistent with the thermolysis results of previously reported of copper(I) iminopyrrolidines.¹⁴⁹ Compounds **1** and **2** produced metallic residues during TGA and solution studies: since the metal(I) ions were reduced, the ligand must have undergone sacrificial oxidation. The presence of protonated ligand as a decomposition product suggests dehydrogenation of the sacrificial ligand. The calculated yields for protonated ligand in solution were between 30 – 80 % of the initial concentration, suggesting the remaining unaccounted-for ligand could have been surface bound in a dehydrogenated

state. Similar chemistry has been proposed for the surface decomposition of copper(I) amidinates, guanidates, and iminopyrrolidates.^{151,152}

The promising results from these thermolysis studies prompted an investigation of these compounds as CVD precursors for metallic films. CVD experiments were carried out in a tube furnace reactor on SiO₂ and Si substrates (Figure 6.15). The first series of depositions were carried out under roughing pump vacuum conditions. The second set were carried out with a flow of heated nitrogen gas to assist in mass transport. Independent heating zones were employed for the nitrogen, precursor bubbler, and furnace areas.

Depositions Without Nitrogen Flow

For **1**, the bubbler was heated to 110 °C and maintained for 3h at 35 mtorr. Approximately 50 to 60 mg of **1** in an open glass vial was completely volatilized under these conditions for each deposition. The onset for film deposition was found to be 140 °C which afforded films less than 5 nm thick, as measured by AFM. Increasing the substrate temperature in 20 °C increments from 140 °C to 220 °C afforded increasingly thicker films each with a thickness gradient receding from the precursor inlet (Figure 6.9, bottom). This series of depositions demonstrates **1** to be stable in the gas phase and at the substrate surface below 140 °C while **1** is completely consumed in the tube furnace above temperatures of 200 °C. The deposited films were confirmed to be metallic silver by XRD and a 156 nm thick film deposited at 220 °C on SiO₂ had a sheet resistance of

0.0158 Ω/\square . Images obtained by scanning electron microscopy (SEM) showed the silver films deposited at 200 °C to be granular with particle sizes corresponding to film thickness (Figure 6.10; a, b). The films were further confirmed to be metallic silver by XPS and EDX analysis.

Compound **2** was tested in a similar manner as a precursor for CVD of gold films on Si substrates. Approximately 30 mg of **2** was heated in a bubbler vial to 130 °C over a 16 h deposition at 35 mtorr. Upon inspection of the vial it was observed that the mass of precursor was not entirely consumed; however, the material remaining consisted of completely intact precursor as determined by ¹H NMR analysis. The onset of film deposition was found to be 300 °C. Increasing the tube furnace temperature in 50 °C increments from 300 °C to 500 °C afforded a thickness profile with a thickness maximum that migrated towards the precursor inlet at higher temperatures (Figure 6.9, top). The thickness profile observed for **2** was significantly different than **1** and this can be attributed at least in part to a more pronounced temperature gradient across the tube furnace at higher temperatures. This series of depositions demonstrates **2** to be stable in the gas phase and at the substrate's surface below 300 °C. Film thickness at the centre of the tube furnace reached a maximum at a temperature of 350 °C and deposition occurred predominately at the precursor inlet at a temperature of 500 °C. The deposited films were confirmed to be metallic gold by XRD. Images obtained by SEM of the gold films deposited at 350 °C consisted of densely packed particles of < 50 nm (Figure 6.10; c, d). Interestingly, film thickness did not correspond to particle size and the thicker areas

appeared more continuous than granular. The films were further confirmed to be metallic gold by XPS and EDX analysis.

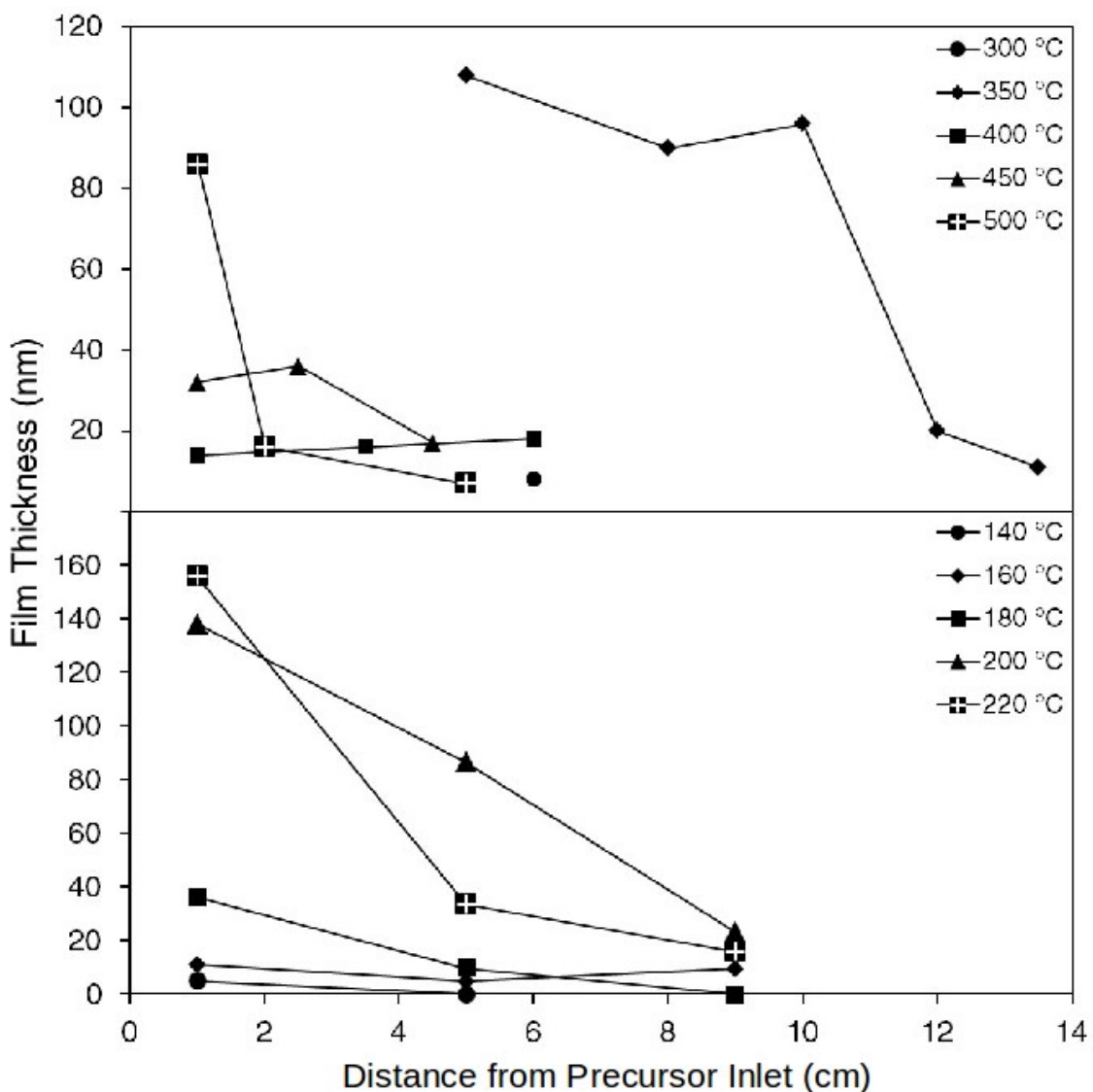


Figure 6.9 Film thicknesses measured from the CVD of **1** (bottom) and **2** (top) at different furnace temperatures. Depositions with **1** consumed 50 - 60 mg of compound. Depositions for **2** consumed varying amounts: 13.9 mg (300 °C); 21.8 mg (350 °C); 5.9 mg (400 °C); 20.6 mg (450 °C); 23.5 (500 °C).

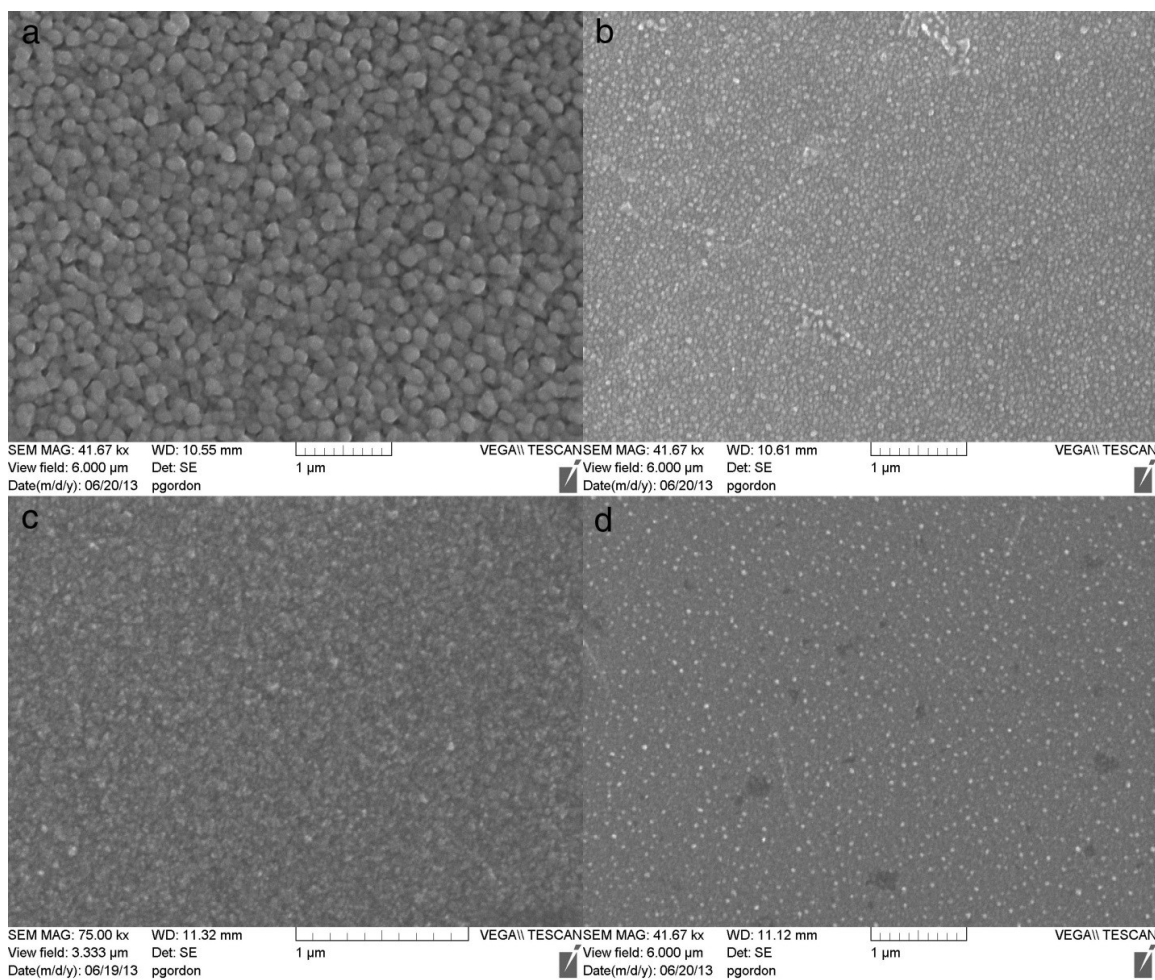


Figure 6.10 SEM images for thin films deposited without N₂ flow from (a, b) **1** and (c, d) **2** at 200 °C and 350 °C, respectively. Images from the CVD of **1** were measured (a) 0.75 cm and (b) 7.75 cm from the precursor inlet. Images from the CVD of **2** were measured (c) 5 cm and (d) 11 cm from the precursor inlet. Film thicknesses in a, b, and c are approximately 87 nm, 23 nm and 123 nm respectively. A reliable film thickness measurement for d could not be obtained.

Depositions with Heated Nitrogen Flow

The depositions described above produced films with a pronounced thickness gradient, thickest nearest the precursor inlet and diminishing from there. This prompted a series of depositions with heated nitrogen flow intended to reduce the severity of the gradient by

increasing mass transport. Similar conditions were maintained where possible, however the increased system pressure due to nitrogen flow meant that higher bubbler temperatures were required. The nitrogen was heated to 110 °C; trials with unheated nitrogen were attempted but it was found that this cooled the bubbler significantly and together with the increased system pressure, quenched precursor volatility. Bubbler temperatures were therefore increased to 120 °C and 150 °C for compounds **1** and **2**, respectively. Precursor masses were 50 mg and 65 mg for compounds **1** and **2**, respectively. Under these conditions, a series of CVD experiments varying furnace temperatures from 250 °C to 400 °C in 50 °C increments were performed with **1** to establish the optimal deposition temperature for further study (Figure 6.11). Each run was 3 hrs long, as measured from initiation of precursor heating to process shutdown by rapid increase in system pressure to atmospheric under nitrogen and termination of all heating.

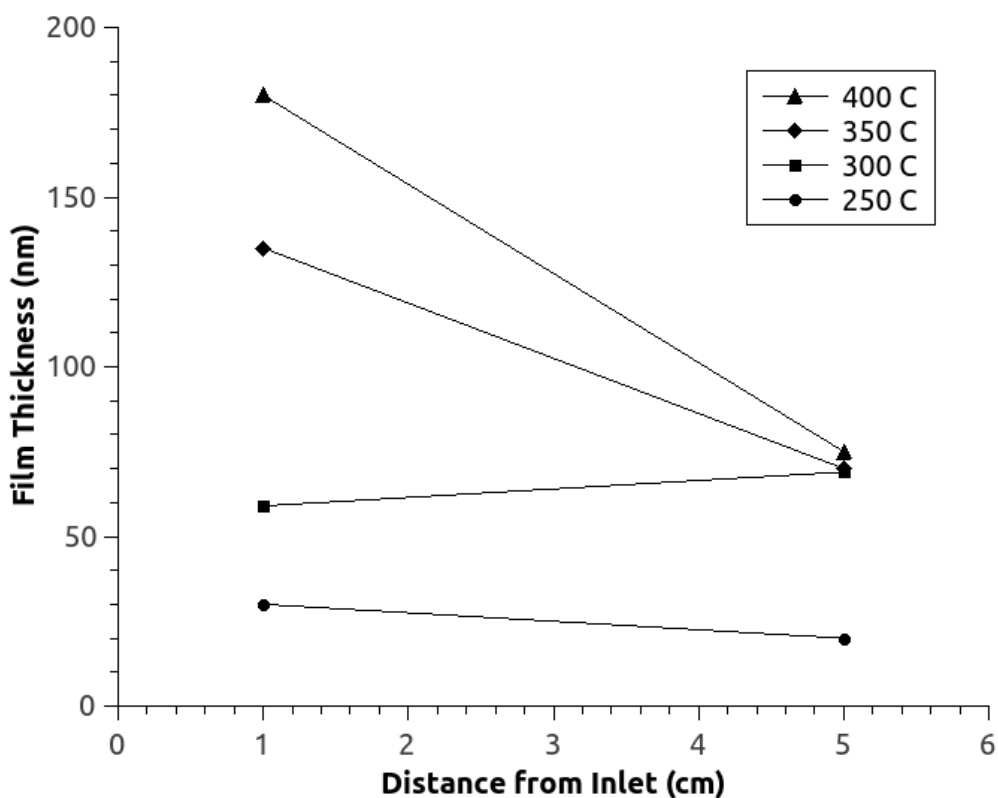


Figure 6.11 Temperature series for silver CVD from **1** with nitrogen flow.

It was found that the most uniform silver deposition was achieved at 300 °C, affording a film 50-60 nm thick. Above this temperature the thickness gradients became much more pronounced, most likely due to an increased rate of precursor decomposition, leading to a gas phase concentration gradient along the direction of flow. In light of these results a series of time-limited depositions were performed with similar precursor masses. Deposition times of 10 minutes to overnight were performed and the thicknesses measured by AFM are illustrated in Figure 6.12. The results confirm that a low flow of

nitrogen can somewhat increase the total coverage of the depositions and even out the thicknesses across a single run, as is particularly clear in the 20 minute deposition.

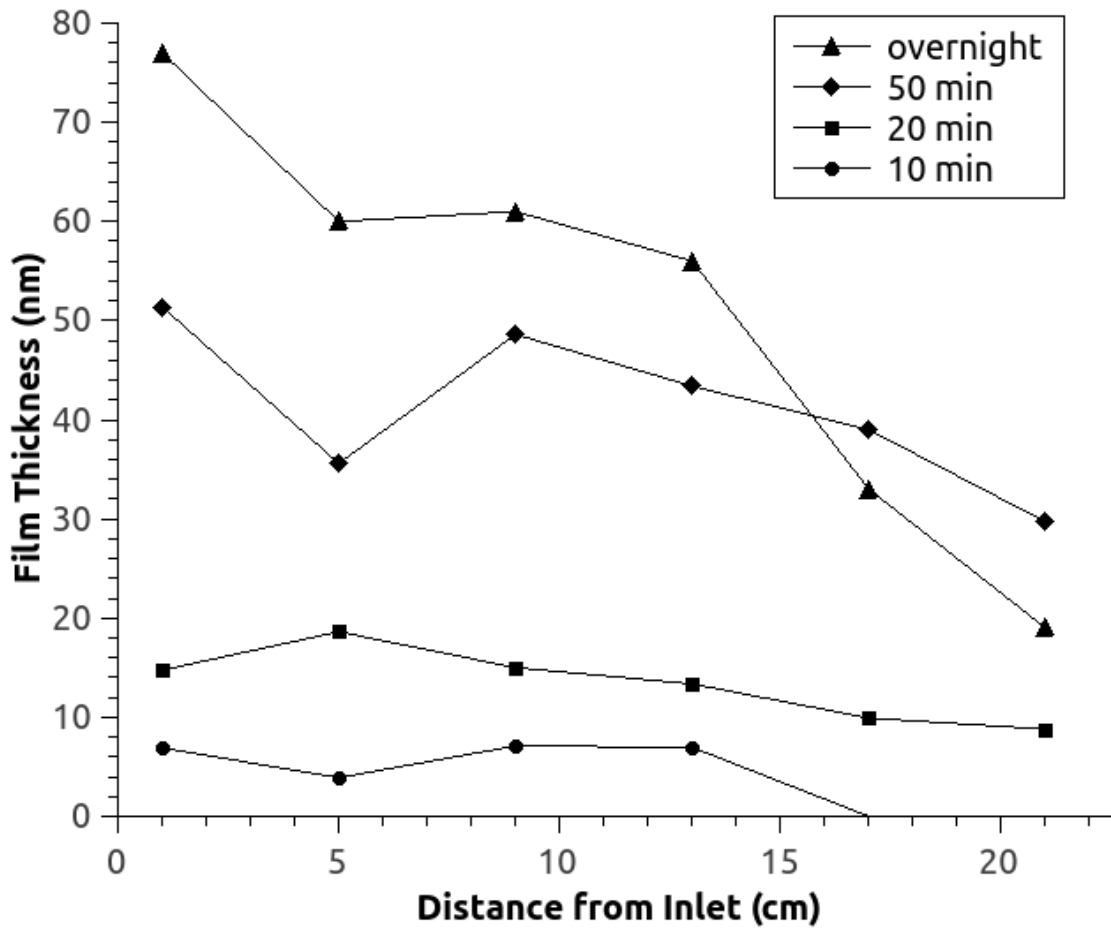


Figure 6.12 Film thicknesses for Ag CVD from **1** with heated N₂ flow, measured by AFM.

The thickness gradient in the longest experiment is attributed to attenuation of precursor flow. As available precursor is exhausted, its gas-phase concentration is reduced and the rate of precursor consumption at the surface eventually exceeds the rate

of mass transport along the surface. Therefore the deposition zone slowly moves back towards the source as precursor is depleted, generating a thicker film closer to the inlet. Figure 6.13 presents data that confirms agreement between AFM and SEM analysis of film thickness. AFM was used exclusively for the remainder of film measurements as sample preparation was straightforward and analysis more economical.

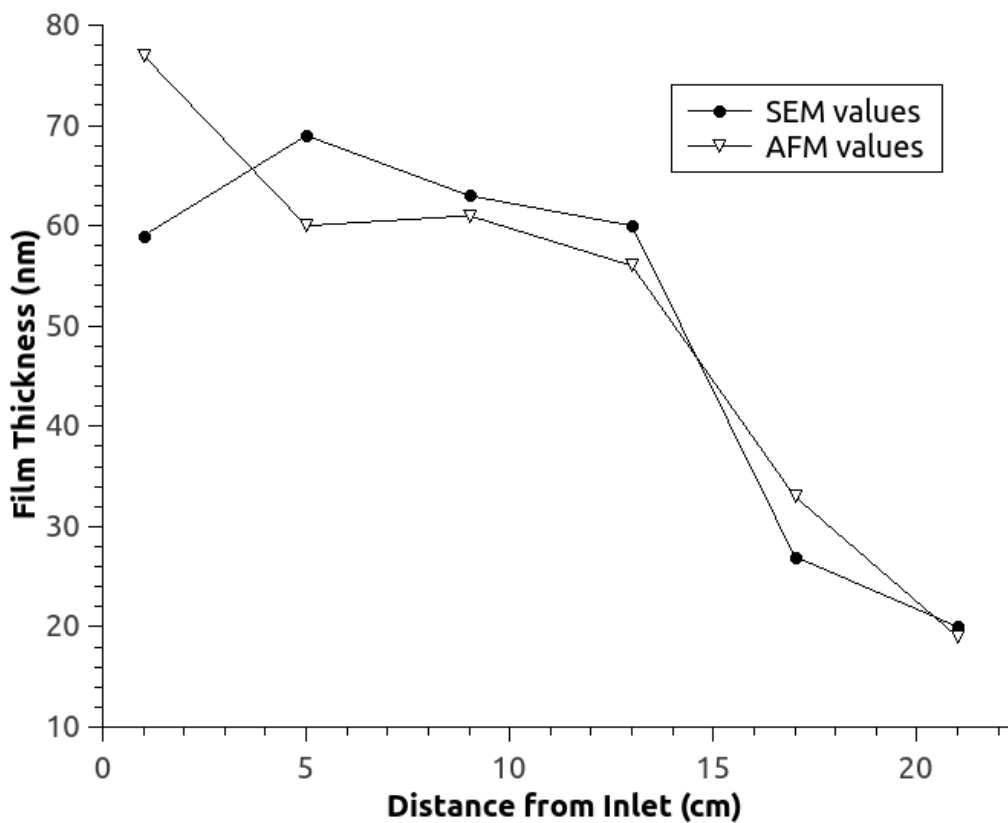


Figure 6.13 Thickness profile for Ag CVD at 300 °C, with nitrogen flow, comparing values obtained by SEM and AFM.

Nearly identical CVD experiments under flow of nitrogen were performed with **2**. It was found that the flow had a much less pronounced effect on film thicknesses (Figure

6.14), particularly at 300 °C which demonstrated no significant change. Intermediate temperatures of 350 °C and 400 °C resulted in intermediate thicknesses, demonstrating growth similar to the curve observed for 450 °C.. The large decrease in thickness past 12 cm for the higher temperatures suggests rapid film growth is depleting the precursor before it can reach more distant areas. The relatively flat films deposited at 300 °C indicate very even, slow decomposition at the surface. This stability is a promising result for the use of **2** as a CVD precursor, and suggests that it should be evaluated as an ALD precursor as well.

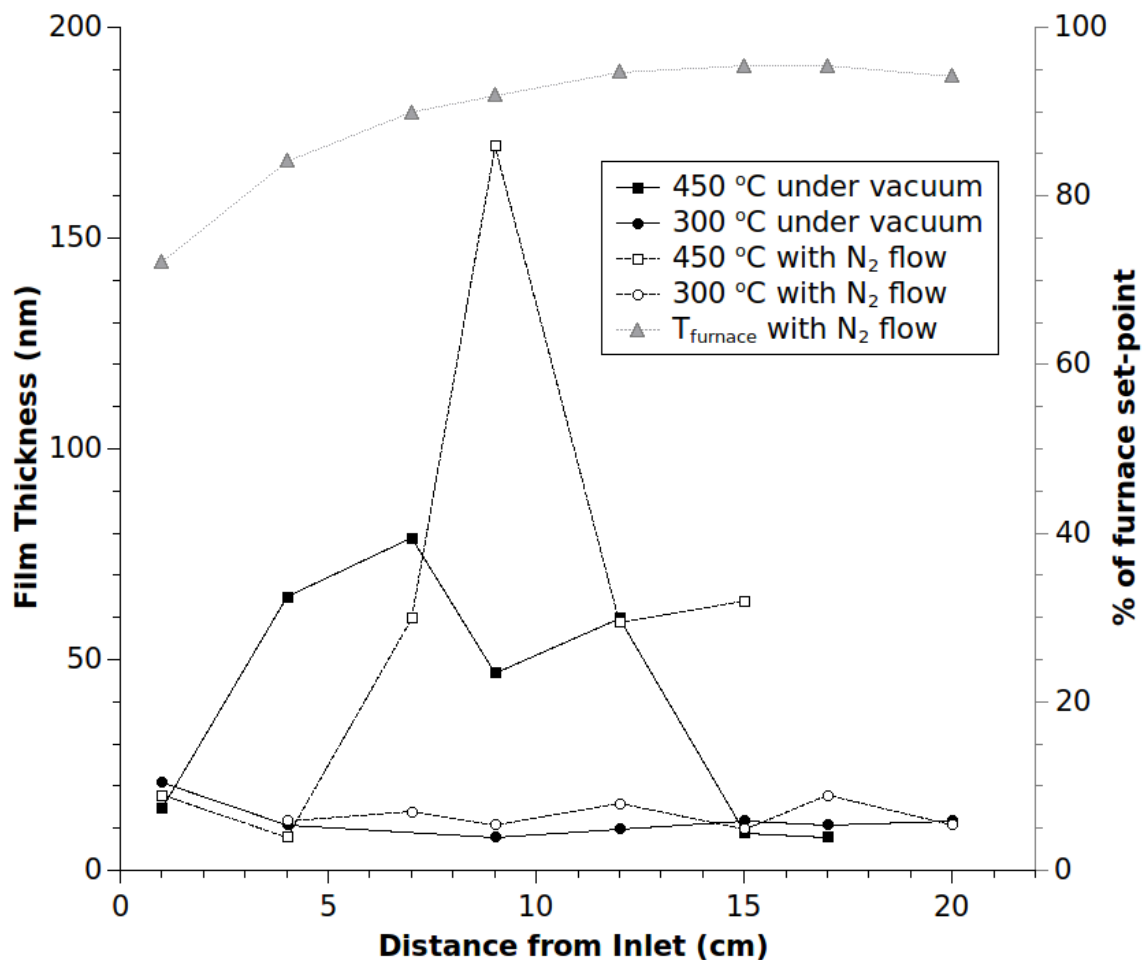


Figure 6.14 Comparison of CVD growth of gold from **2**, with (dotted lines) and without (solid lines) nitrogen flow. The triangular data points depict the temperature gradient of the furnace tube. Intermediate temperatures of 350 °C and 400 °C (not shown) result in similar, intermediate growth.

To evaluate the effect of the thermal gradient in the furnace tube on the observed film thicknesses, a study of the internal temperature of the furnace was undertaken with a thermocouple sealed in a hollow glass tube. An o-ring seal allowed the thermocouple to be positioned as desired along the length of the furnace tube while maintaining a system pressure of approximately 950 mTorr. While not an ideal, quantitative assessment, this

allowed for a rough estimate of the temperature gradient experienced by the substrates. For a furnace set-point of 400 °C, allowed to equilibrate for 3 hrs, the gradient began at 1 cm from the precursor inlet at 72% of the furnace set-point value and approached 95% of the value by the midpoint of the furnace, about 15 cm from the precursor inlet (Figure 6.14). At 20 cm the temperature gently curved back down to 68% by 29 cm. Further equilibration time did not significantly alter these values. Variations in film thickness can in part be attributed to this thermal gradient, but the effect of film growth rate must also be considered. The growth rate at 450 °C under nitrogen peaks at 9 cm, but this does not imply that higher temperatures downstream of this point are not amenable to growth; it is more likely that around this temperature growth rate is so rapid as to consume precursor faster than it can be delivered, and so growth downstream is frustrated by lack of precursor.

A study of precursor mass consumption was beyond the scope of this work but would provide valuable insight into the nature of the deposition. A series of experiments that varied precursor mass load of **1** and **2** for a fixed deposition duration and temperature could provide very useful data.

6.4 Experimental

General Considerations

Some manipulations (loading, filtering, and isolation) were performed in an MBraun Labmaster™ 130 Dry box (mBraun, Stratham, NH, U.S.A.) under a nitrogen atmosphere

while additions were performed by standard Schlenk techniques. NMR spectra were recorded on a 400 MHz Bruker AMX spectrometer. NMR spectra were measured in C₆D₆ or CDCl₃ and were referenced against residual protonated solvent or TMS, respectively. Tert-butylimino-2,2-dimethylpyrrolidine⁴⁰ and THT·AuCl¹⁵³ were prepared according to literature. AgCl was purchased from Strem Chemicals and used as received. Canadian Microanalytical Service Ltd. performed combustion analysis. Thermogravimetric analysis was performed on a TA Instruments Q50 apparatus located in an MBraun Labmaster130 Dry box under a nitrogen atmosphere. Differential scanning calorimetry was performed on a DSC Instruments Q10 apparatus. Toluene and diethyl ether were purchased as ACS grade and purified from an Mbraun Solvent Purifier System. Dichloromethane and pentane were purchased as anhydrous from Sigma Aldrich Chemical Company and used as received

Silver(I) tert-butyl-imino-2,2-dimethylpyrrolidinate (1): Tert-butyl-imino-2,2-dimethylpyrrolidine (3.364 g, 20.0 mmol) was dissolved in 60 mL of toluene and cooled to 0 °C. Butyl lithium in hexanes (2.5 M, 8.0 mL, 20.0 mmol) was added dropwise and the solution was stirred for 3h at room temperature. In a separate 500 mL Schlenk flask wrapped in aluminum foil, AgCl (2.865 g, 20.0 mmol) was suspended in 200 mL of toluene. The lithiated iminopyrrolidinate solution was added dropwise via cannula over 1 h and the resulting mixture was stirred for 16 h. The reaction mixture was filtered and the insoluble solids were washed with 20mL of toluene. Volatiles were stripped off from the combined wash and filtrate to afford a light brown solid. The insoluble solids were

washed further with dichloromethane (3 x 20 mL). These washings were combined and volatiles were stripped off to afford more of the light brown solid. The two portions of solid were combined and washed with pentane (4 x 10 mL). The crude solid was recrystallized from 20 mL of hot toluene in a pressure vessel to afford colourless, block crystals; 3.615g, 65.7%. ¹H NMR (400 MHz, C₆D₆): δ 1.16 (s, 6H, NC(CH₃)₂CH₂CH₂C), δ 1.29 (s, 9H, NC(CH₃)₃), δ 1.65 (t, 2H, NC(CH₃)₂CH₂CH₂C), δ 2.54 (t, 2H, NC(CH₃)₂CH₂CH₂C) ¹³C NMR (400 MHz, C₆D₆): 32.89 (NC(CH₃)₂CH₂CH₂C), 33.79 (NC(CH₃)₂CH₂CH₂C), 33.98 (NC(CH₃)₃), 38.26 (NC(CH₃)₂CH₂CH₂C), 52.81 (NC(CH₃)₂CH₂CH₂C), 61.29 (NC(CH₃)₃), 175.12 (NCN) Combustion analysis, found(calculated): C, 43.21(43.65); H, 7.04(6.96); N, 10.15(10.18).

Gold(I) tert-butyl-imino-2,2-dimethylpyrrolidinate (2): Tert-butyl-imino-2,2-dimethylpyrrolidine (2.874 g, 17.1 mmol) was dissolved in 60 mL of toluene and cooled to 0 °C. Butyl lithium in hexanes (2.5 M, 6.83 mL, 17.1 mmol) was added dropwise and the solution was stirred for 3h at room temperature. In a separate 500 mL Schlenk flask wrapped in aluminum foil, THT·AuCl (5.475, 17.1 mmol) was suspended in 175mL of toluene and cooled to -78 °C. The lithiated iminopyrrolidinate solution was added dropwise via cannula over 1 h and the resulting mixture was stirred for 16 h gradually warming to room temperature. Volatiles were stripped off under reduced pressure to afford a dark solid which was dried under high-vac to remove residual THT. The solid was stirred with warm toluene (4 x 50 mL) for 15 min and filtered. The extractions were combined and volatiles were removed under reduced pressure to afford a solid that was

washed with diethyl ether (4 x 5 mL). The solid was dissolved in 20 mL of hot toluene in a pressure vessel and left to stand for 12 h cooling to room temperature. A crop of colourless, block crystals were isolated by decanting the supernatant, washing with diethyl ether (3 x 5 mL) and dried under vacuum to afford 2.100 g. A second crop of product was obtained from the insoluble solid that remained post toluene extraction. The remaining insoluble solids were stirred with dichloromethane (4 x 50 mL) for 15 min and filtered. The extractions were combined and volatiles were removed under reduced pressure to afford a solid that was washed with diethyl ether (4 x 5 mL). The solid was dissolved in 20 mL of hot toluene in a pressure vessel and left to stand for 12 h cooling to room temperature. A second crop of colourless, block crystals were isolated by decanting the supernatant, washing with diethyl ether (3 x 5 mL) and drying under vacuum to afford 1.960 g; total yield was 4.060 g, 65.3%. ¹H NMR (400 MHz, CDCl₃): δ 1.18 (s, 6H, NC(CH₃)₂CH₂CH₂C), δ 1.38 (s, 9H, NC(CH₃)₃), δ 1.72 (t, 2H, NC(CH₃)₂CH₂CH₂C), δ 2.73 (t, 2H, NC(CH₃)₂CH₂CH₂C) ¹³C NMR (400 MHz, CDCl₃): δ 30.48 (NC(CH₃)₂CH₂CH₂C), δ 33.69 (NC(CH₃)₃), δ 34.25 (NC(CH₃)₂CH₂CH₂C), δ 36.78 (NC(CH₃)₂CH₂CH₂C), δ 55.99 (NC(CH₃)₂CH₂CH₂C), δ 63.45 (NC(CH₃)₃), δ 176.47 (NCN) Combustion analysis, found(calculated): C, 32.85(32.98); H, 5.23(5.26); N, 7.67(7.69).

Crystal Structure studies for compounds 1 and 2: Crystals were selected, sectioned as required, and mounted on plastic mesh with viscous oil and flash-cooled to the data collection temperature. Diffraction data were collected on a Bruker-AXS APEX II Duo

CCD diffractometer with graphite-monochromated Mo-K α radiation ($\lambda=0.71073$ Å). The data-sets were treated with SADABS absorption corrections based on redundant multiscan data. The unit cell parameters and systematic absences in the diffraction data were uniquely consistent for P2₁/c. The isomorphous structures were solved using direct methods and refined with full-matrix, least-squares procedures on F². Unit cell parameters were determined by sampling three different sections of the Ewald sphere. Nonhydrogen atoms were refined with anisotropic displacement parameters. Hydrogen atoms were treated as idealized contributions. Structure factors and anomalous dispersion coefficients are contained in the SHELXTL 6.12 program library.¹²⁰ The structures have been deposited at the Cambridge Crystallographic Data Centre under CCDC 949353 & 949354.

Chemical Vapour Deposition

Depositions were conducted in a custom built CVD apparatus (Figure 6.15). A coil of 3 mm stainless steel tubing heated with resistive heating rope controlled by a variable autotransformer was employed for heated nitrogen gas delivery. Nitrogen flow was regulated with a needle valve to achieve the desired process pressure. The nitrogen was delivered to a “bubbler” section 15 cm long containing the precursor and independently heated with resistive heating tape. The bubbler was directly connected to the deposition tube which was enclosed in a clamshell-type furnace approximately 50 cm long. The substrates were placed in the centre of the furnace tube to minimize thermal gradients and

occupied a space approximately 21 cm long. Vacuum was established with a roughing pump and monitored with a thermocouple pressure sensor. A liquid nitrogen cold trap was placed inline between the deposition zone and the pump to trap volatiles. A second nitrogen line installed at the junction between the deposition zone and the cold trap and regulated with a ball valve was used to purge the system prior to deposition and maintain a positive pressure of nitrogen during precursor loading. This nitrogen line was also used to halt depositions abruptly by rapidly increasing system pressure. The process termination effected by this technique is attributed to rapid and complete elimination of precursor volatilization and has been verified previously by our lab *in situ* for this system.³⁹

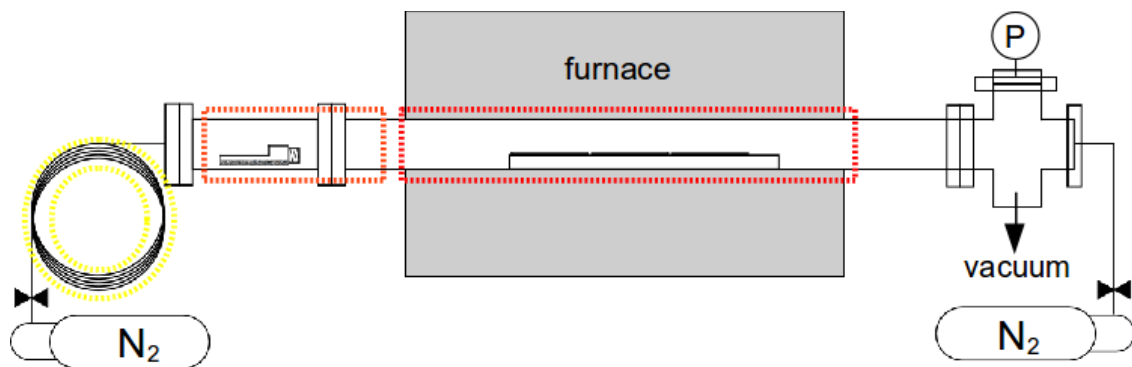


Figure 6.15 CVD apparatus with attachment for heated nitrogen delivery. Dotted lines indicate the three separately-controlled heating zones.

Substrates, including quartz slides, borosilicate glass slides, and silicon (100) wafers were all cleaned according to the same protocol: 20min in piranha solution (3:1 by volume mix of concentrated sulphuric acid and 35% hydrogen peroxide in water)

followed by a distilled water rinse and then allowed to dry in air. Substrate were all at most 1.4cm wide and between 3 and 7cm long.

In a typical deposition experiment, the precursor was weighed out into a vial under nitrogen in a glove box. The vial was then placed in the bubbler, sealed, and transported to the CVD apparatus. Prior to this the substrates were previously placed in position in the centre of the furnace tube. The bubbler was attached while the apparatus was under a flow of nitrogen. The system was then evacuated and heating of the nitrogen delivery line and furnace begun. A 30min equilibration period was allowed before depositions were attempted. At time zero, bubbler heating was initiated and heated nitrogen flow was adjusted using the needle valve until a system pressure of 100mTorr was achieved. The heating ramp for the bubbler was performed by manual adjustment of the voltage delivered to the heating tape, monitored by thermocouple, and effected rapidly. The temperature was monitored using external thermocouples throughout the depositions to ensure stability and the voltage was adjusted as required to maintain the desired process temperature.

Film Characterization

Film morphology and composition were determined by scanning electron microscopy (SEM) and electron dispersive x-ray spectroscopy (EDS) using a Tescan Vega-II XMU VPSEM equipped with an Inca EDS. Quantitative analysis was calibrated using a pure copper sample.

Film thickness and morphology were examined by atomic force microscopy (AFM). Data was acquired with a NanoSurf easyScan 2 tool equipped with an aluminum reflex coated silicon probe tip. Data was processed and analyzed using WSxM 5.0.¹⁵⁴ Film thicknesses were determined by imaging a scratch made in the film with a razor followed by a histogram analysis (count of feature heights; example shown below in Figure 6.16).

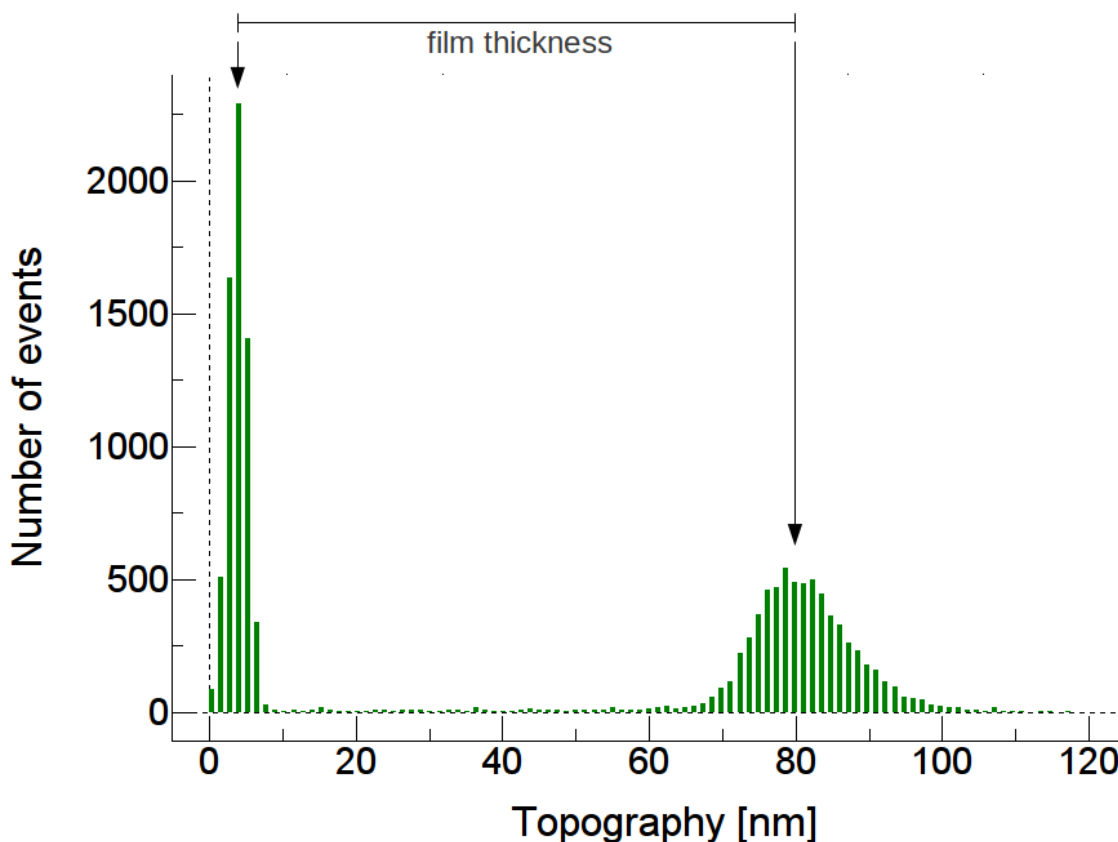


Figure 6.16 Example of histogram technique used to determine film thickness from AFM data. Data shown is from a gold deposition from **2** at 350 °C, 8 cm from the precursor inlet.

The histogram was extracted from a section of the image displaying roughly equal areas of substrate and film. This yielded a histogram with two peaks, each corresponding

to the most common heights of the substrate and the film respectively. The difference between these two peaks was taken as the film thickness. This provides a reliable method for thickness determination that also affords a qualitative examination of film roughness. Film roughness was also quantitatively extracted from this data. A second technique was employed to double-check film thickness characterization: the difference between average heights taken from linear cross-sections of nearby film and substrate sections, with generally good agreement. This method has shown good correlation with thicknesses determined from SEM interrogation of cross-sections. Sheet resistance was measured with a four-point probe.

Thermal Decomposition Solution Studies

Solutions of **1** and **2** were prepared by adding a known mass of compound to a known mass of C₆D₆. A drop of TMS was added as an internal standard. The concentrations for **1** and **2** were 7.8 mM and 1.8 mM, respectively. The solutions were frozen in heavy walled NMR tubes in liquid N₂ and flamed sealed under 100 mtorr dynamic vacuum. The isothermal oven was illuminated with a 60 W incandescent light bulb and NMR tubes were wrapped with aluminum foil to exclude light. ¹H NMR spectra were measured on a 300 MHz Avance 3 every 24 h after the tubes cooled to room temperature for 20 min.

6.5 Conclusion

Two thermally robust CVD precursors for silver and gold thin films were synthesized and thermally characterized. Compounds **1** and **2** are thermally stable up to 170 °C as

pure solids. These precursors remained volatile up to 240 °C during TGA in 1 atm of inert gas. Under low pressure CVD conditions, **1** and **2** could be volatilized, without decomposition, between 110 °C – 130 °C. Under moderate flow of heated nitrogen carrier gas, similar volatilization without decomposition was observed for 120 °C – 150 °C.

TGA, DSC and CVD experiments revealed **2** as more thermally stable than **1**. The trend in thermal stability for the series of coinage metal precursors was Cu > Au > Ag and the trend in volatility was Cu > Ag > Au. In C₆D₆ solutions **1** was more thermally stable than **2**, where both compounds demonstrated increased decomposition rates under exposure to light with otherwise identical conditions. Solution NMR thermal studies resulted in metallic films on the tube surface and protonated ligand as the observable decomposition products. Rates of decomposition in solution could not be fit to simple models, suggesting complex decomposition pathways.

Compounds **1** and **2** are improved precursors for thermal CVD applications as compared to other amidinate and guanidinate compounds – their evaporation temperature and gas phase decomposition temperatures are well separated which is desirable for both CVD and ALD. The ligand design successfully blocked the previously problematic low temperature decomposition pathways of β -hydrogen abstraction and CDI deinsertion.¹¹⁶ Thermal decomposition of **1** and **2** could still be achieved at reasonable CVD process temperatures, affording metallic residues and thin films. The evidence suggests dehydrogenation of the ligand at higher temperatures but a thorough gas phase

decomposition mechanism study will be required for a detailed understanding of the process. Metallic thin films of silver and gold consisting of granular, nanoparticulate films were deposited at low pressures between 140 °C - 220 °C and 300 °C - 500 °C, respectively. Similar films were obtained from depositions with heated N₂ flow at 250 °C - 400 °C and 300 °C - 450 °C, respectively. Nitrogen flow assisted in greater film thickness uniformity for depositions with **1** but no significant change was observed for depositions with **2**. Further work to fully characterize the composition of the films may provide interesting insight into the deposition chemistry at the surface. Current investigations are focusing on further optimization of CVD conditions, plasmonic device fabrication, and evaluating the precursors in conjunction with reducing agents for use in ALD processes.

Chapter 7 - Conclusions

While the individual projects described in this work are diverse, they all concern the study and practical application of thin film deposition chemistry: the chemistry of the precursors used for chemical vapour deposition and atomic layer deposition, and the mechanism of thin film growth by these methods. Characterization of thin film precursors, in particular studies of their thermal behaviour, was pursued not only to evaluate the precursors for use in film deposition but also to examine their decomposition pathways. The deposited films were evaluated by several criteria: physical and chemical protection of metal alloys, optical and electronic behaviour, and physical morphology.

Bronze and brass coins and tokens were coated by ALD with aluminum oxide using a previously reported process and were found to provide significant protection against moderate chemical attack. Growth rates for deposition of films with thicknesses on the order of 1000 – 10,000 Å were independent of substrate and it was found that the films adhered more strongly to the metal substrates than to the silicon. This became particularly pronounced at film thicknesses of 6000 Å and above, where the silicon substrates demonstrated significant delamination. It was found that the TTIP/water ALD process yielded good titanium oxide film growth on metal samples coated with 1200 Å of aluminum oxide, as confirmed by XPS. The same process resulted in extremely poor growth on uncoated metal samples. Uniformity experiments on batch depositions on 2744 substrates revealed that a pulse program with three subsets of precursor/purge pulses for

each precursor was required at a process temperature of 250 °C. A preliminary three hour thermal equilibration period was also required for uniformity across all samples.

A study the effect of aluminum oxide thickness on perceived colour of the metal substrates was performed. In addition to a 1200 Å film that induced no noticeable change in colour, an array of colours including iridescence that may prove useful for numismatic, limited edition coins were observed. The optical properties of thin films on metals and metal alloys merit future investigation as anti-counterfeiting measures. Additionally, a study of the nature and composition of the interface layer between metal substrates and alumina film would help to understand both protective and cosmetic issues. A thorough study of protection from wear and chemical attack, particularly using laminate films, is recommended.

Motivated by these preliminary colour studies, a robot-based gonireflectometer was used to more carefully analyze the colours resulting from thin films (0 - 1613 Å) of aluminum oxide deposited by ALD on silicon. The experimental reflectivities obtained were compared to those predicted by software simulations and the observations were found to deviate from simulated results along the metrics of film thickness, wavelength of light, and angle of incidence/observation. With respect to film thickness, the largest disagreement between theory and experiment was observed for the films near 800 Å. These films are also the most iridescent. With respect to wavelength, the largest disagreement was most often observed at short wavelengths, with 7 of the 12 samples

exhibiting their largest deviations from the model between the wavelengths of 380 and 445 nm. An angular analysis of the data showed that the disagreements were higher at near-normal angles of reflection ($\leq 15^\circ$). Future efforts towards a more accurate simulation of the system should include measurements of the dispersion curves of the deposited films. A comparison study with other film and substrate compositions should also reveal interesting phenomena.

Various thicknesses of alumina films (approximately 4-10 nm) were deposited by ALD on flat and nanostructured silicon substrates, and incorporated into architectures that were then evaluated as photovoltaic devices. It was found that good photovoltaic MIS devices are possible when a traditional metal is replaced with PEDOT. The reverse saturation currents observed on flat devices made with Al_2O_3 films were quite similar to similar devices made with an SiO_2 layer. The forward currents are, however, substantially lower for the devices with Al_2O_3 . The structured samples with Al_2O_3 showed a considerable increase in efficiency (of up to five times) over the equivalent flat samples.

The nanostructured silicon used in this work had aspect ratios of 1:1. To achieve higher aspect ratio structures other techniques can be used such as etch of gold deposited by CVD and self-masking electron cyclotron resonance reactive ion etching (ECR RIE).^{34,155} The testing of the devices made with these techniques is ongoing.

It is expected that spin coating of PEDOT:PSS will be incompatible with the high aspect ratio structures that we hope to use on the substrates in the future. To mitigate this

problem deposition of PEDOT by vapour phase polymerization (VPP) or In_2O_3 by CVD will be attempted. The assembly of the deposition system is in progress.

The simple synthesis of a new indium precursor, $\text{In}[(\text{N}^i\text{Pr})_2\text{CNMe}_2]_3$, in high yields led to promising CVD experiments of indium oxide films. The precursor was found to eliminate protonated guanidine over time in an inert atmosphere, as well as producing diisopropylcarbodiimide and dimethylamine when heated to $140\text{ }^\circ\text{C}$ as a solution in deuterated benzene. Thermogravimetric analyses suggested that **1** decomposed to indium metal in an inert atmosphere, corroborated by vacuum CVD experiments without a reactant gas at temperatures above $275\text{ }^\circ\text{C}$. When air was used as a reactant gas in a CVD experiment above $275\text{ }^\circ\text{C}$, the compound was found to produce transparent indium oxide. At a temperature of $325\text{ }^\circ\text{C}$, the films were found to be crystalline cubic indium oxide. Small impurities of indium metal were observed, suggesting a film growth mechanism where indium undergoes reduction and is then re-oxidized to In_2O_3 . Further study of this precursor for CVD or ALD deposition of indium metal is advised.

Two thermally robust CVD precursors for silver and gold thin films were synthesized and thermally characterized. These precursors remained volatile up to $240\text{ }^\circ\text{C}$ during TGA in 1 atm of inert gas. Under low and high pressure CVD conditions, volatilization without decomposition between $110\text{ }^\circ\text{C}$ – $150\text{ }^\circ\text{C}$ yielded metallic films of silver and gold

at deposition temperatures between 140 °C – 220 °C and 300 °C – 500 °C, respectively. These films consisted of granular, nanoparticulate films on glass and silicon substrates. Similar films were obtained from depositions with heated N₂ flow at 250 °C - 400 °C and 300 °C - 450 °C, respectively. While nitrogen flow assisted in greater film thickness uniformity for depositions with **1**, no significant change was observed for depositions with **2**. Depositions with **2** at 300 °C yielded extremely uniform film thicknesses, suggesting **2** may be useful as an ALD precursor.

TGA, DSC and CVD experiments revealed **2** as more thermally stable than **1**. Solution NMR thermal studies resulted in metallic films on the tube surface and protonated ligand as the observable decomposition products. Rates of decomposition in solution could not be fit to simple models, suggesting complex decomposition pathways. Further study will be required to understand these solution-phase decomposition mechanisms. Thermal characterization further revealed that the ligand design successfully blocked β -hydrogen abstraction and CDI de-insertion decomposition pathways observed previously in analogous amidinate and guanidinate compounds.⁹⁸ The evidence suggests dehydrogenation of the ligand at higher temperatures.

Current investigations are focusing on further optimization of CVD conditions, plasmonic device fabrication, and evaluating the precursors in conjunction with reducing agents for use in ALD processes. A thorough gas phase decomposition mechanism study will also be required for a detailed understanding of the film deposition process.

References

1. L. Niinistö, M. Nieminen, J. Päiväsaari, J. Niinistö, and M. Putkonen, *Physica Status Solidi (A)*, 2004, **201**, 1443–1452.
2. C. R. Kleijn, in *Chemical Physics of Thin Film Deposition Processes for Micro- and Nano-Technologies*, ed. Y. Pauleau, Springer Netherlands, 2002, vol. 55, pp. 119–144.
3. K. L. Choy, *Progress in Materials Science*, 2003, **48**, 57–170.
4. M. Meyyappan, *Progress in Crystal Growth and Characterization of Materials*, 2009, **55**, 1–21.
5. S. H. Lee, D. H. Lee, W. J. Lee, and K. Sang Ouk, *Advanced Functional Materials*, 2011, **21**, 1338–1354.
6. J. López-García, C. Maffiotte, and C. Guillén, *Solar Energy Materials & Solar Cells*, 2010, **94**, 1263–1269.
7. P. Chen, G. Shen, H. Chen, Y. Ha, C. Wu, S. Sukcharoenchoke, Y. Fu, J. Liu, A. Facchetti, T. J. Marks, M. E. Thompson, and C. Zhou, *ACS Nano*, 2009, **3**, 3383–3390.
8. A. M. E. Raj, C. Ravidhas, R. Ravishankar, A. R. Kumar, G. Selvan, M. Jayachandran, and C. Sanjeeviraja, *Materials Research Bulletin*, 2009, **44**, 1051–1057.
9. Y. S. P. and H.-K. K. H. Lee, J.-W. Park, H. Lee, *J. Korean Phys. Soc.*, 2010, **56**, 625.
10. S. Kannan, L. Rieth, and F. Solzbacher, *Sensors and Actuators B: Chemical*, 2010, **149**, 8–19.

11. G. Korotcenkov, S.-D. Han, B. K. Cho, and V. Brinzari, *Critical Reviews in Solid State and Materials Sciences*, 2009, **34**, 1–17.
12. K. Arshak, G. Hickey, E. Forde, and J. Harris, *Nano*, 2008, **03**, 217–222.
13. G. Cheng, E. Stern, S. Guthrie, M. A. Reed, R. Klie, Y. Hao, G. Meng, and L. Zhang, *Applied Physics A*, 2006, **85**, 233–240.
14. G. Korotcenkov, *Sensors and Actuators B: Chemical*, 2005, **107**, 209–232.
15. T. Asikainen, M. Ritala, and M. Leskelä, *Journal of The Electrochemical Society*, 1994, **141**, 3210–3213.
16. O. Nilsen, R. Balasundaraprabhu, E. V. Monakhov, N. Muthukumarasamy, H. Fjellvåg, and B. G. Svensson, *Thin Solid Films*, 2009, **517**, 6320–6322.
17. N. Tripathi, S. Rath, V. Ganesan, and R. J. Choudhary, *Applied Surface Science*, 2010, **256**, 7091–7095.
18. K. L. Chopra, S. Major, and D. K. Pandya, *Thin Solid Films*, 1983, **102**, 1–46.
19. L. G. Bloor, C. J. Carmalt, and D. Pugh, *Coordination Chemistry Reviews*, 2011, **255**, 1293–1318.
20. J. a. Libera, J. N. Hryn, and J. W. Elam, *Chemistry of Materials*, 2011, **23**, 2150–2158.
21. S. Basharat, C. J. Carmalt, S. A. Barnett, D. A. Tocher, and H. O. Davies, *Inorganic Chemistry*, 2007, **46**, 9473–9480.
22. J.-H. Park, G. A. Horley, P. O'Brien, A. C. Jones, and M. Motevalli, *J. Mater. Chem.*, 2001, **11**, 2346–2349.

23. H. W. Kim, N. H. Kim, and J. H. Myung, *J. Mater. Sci. Let.*, 2005, **40**, 4991.
24. S. Suh and D. M. Hoffman, *Journal of the American Chemical Society*, 2000, **122**, 9396–9404.
25. D. Edwards, R. Harker, M. Mahon, and K. Molloy, *Inorganica Chimica Acta*, 2002, **328**, 134–146.
26. R. Voorhoeve and J. Merewether, *Journal of The Electrochemical Society*, 1972, 364–368.
27. S. K. Jana, A. Le Donne, and S. Binetti, *Journal of Physics and Chemistry of Solids*, 2011, **73**, 143–147.
28. F. Jansen and T. Kruck, *Advanced Materials*, 1995, **7**, 297–300.
29. R. G. Parkhomenko, N. B. Morozova, G. I. Zharkova, Y. V. Shubin, S. V. Trubin, V. V. Kriventsov, B. M. Kuchumov, T. P. Koretskaya, and I. K. Igumenov, *Chemical Vapor Deposition*, 2012, **18**, 1–7.
30. R. G. Parkhomenko, A. E. Turgambaeva, N. B. Morozova, S. V. Trubin, V. V. Krisyuk, and I. K. Igumenov, *Chemical Vapor Deposition*, 2013, **19**, 38–44.
31. M.-C. Daniel and D. Astruc, *Chemical Reviews*, 2004, **104**, 293–346.
32. S. Sarina, E. R. Waclawik, and H. Zhu, *Green Chem.*, 2013, **15**, 1814–1833.
33. Z. Huang, N. Geyer, P. Werner, J. de Boor, and U. Gösele, *Advanced Materials*, 2011, **23**, 285–308.
34. A. Kurek and S. T. Barry, *Advanced Materials*, 2011, **12**, 045001.
35. O. J. Hildreth, W. Lin, and C. P. Wong, *ACS Nano*, 2009, **3**, 4033–42.

36. S. Chan, S. Kwon, T.-W. Koo, L. P. Lee, and a. a. Berlin, *Advanced Materials*, 2003, **15**, 1595–1598.
37. L. H. Qian, X. Q. Yan, T. Fujita, a. Inoue, and M. W. Chen, *Applied Physics Letters*, 2007, **90**, 153120.
38. V. Iberi, N. Mirsaleh-Kohan, and J. Camden, *The Journal of Physical Chemistry Letters*, 2013, **4**, 1070–1078.
39. W. Zhou, D. Mandia, M. Griffiths, A. Bialliayeu, Y. Zhang, P. G. Gordon, S. T. Barry, and J. Albert, *Optics Express*, 2013, **21**, 245–255.
40. J. P. Coyle, A. Kurek, P. J. Pallister, E. R. Sirianni, G. P. a Yap, and S. T. Barry, *Chemical Communications*, 2012, **48**, 10440–2.
41. Y. a Wasslen, A. Kurek, P. a Johnson, T. C. Pigeon, W. H. Monillas, G. P. a Yap, and S. T. Barry, *Dalton transactions (Cambridge, England : 2003)*, 2010, **39**, 9046–54.
42. S. M. George, *Chemical Reviews*, 2010, **110**, 111–31.
43. T. Suntola and J. Antson, 1977.
44. T. Helbling, C. Hierold, C. Roman, L. Durrer, M. Mattmann, and V. M. Bright, *Nanotechnology*, 2009, **20**, 434010.
45. Y. Xuan, Y. Q. Wu, T. Shen, M. Qi, M. A. Capano, J. A. Cooper, and P. D. Ye, *Applied Physics Letters*, 2008, **92**, 013101.
46. Y. Au, Y. Lin, H. Kim, E. Beh, Y. Liu, and R. G. Gordon, *Journal of The Electrochemical Society*, 2010, **157**, D341.

47. L. Lari, T. Walther, K. Black, R. T. Murray, T. J. Bullough, P. R. Chalker, C. Chèze, L. Geelhaar, and H. Riechert, *Journal of Physics: Conference Series*, 2010, **209**, 12011.
48. D. M. King, S. I. Johnson, J. Li, X. Du, X. Liang, and A. W. Weimer, *Nanotechnology*, 2009, **20**, 195401.
49. M. K. Tripp, C. Stampfer, D. C. Miller, T. Helbling, C. F. Herrmann, C. Hierold, K. Gall, S. M. George, and V. M. Bright, *Sensors and Actuators A: Physical*, 2006, **130-131**, 419–429.
50. C. R. Stoldt and V. M. Bright, *Journal of Physics D: Applied Physics*, 2006, **39**, R163.
51. C. F. Herrmann, F. W. DelRio, V. M. Bright, and S. M. George, *Journal of Micromechanics and Microengineering*, 2005, **15**, 984.
52. G. L. Doll, B. a. Mensah, H. Mohseni, and T. W. Scharf, *Journal of Thermal Spray Technology*, 2009, **19**, 510–516.
53. T. W. Scharf, S. V Prasad, M. T. Dugger, P. G. Kotula, R. S. Goeke, and R. K. Grubbs, *Acta Materialia*, 2006, **54**, 4731–4743.
54. S. T. Christensen, H. Feng, J. L. Libera, N. Guo, J. T. Miller, P. C. Stair, and J. W. Elam, *Nano Letters*, 2010, **10**, 3047–3051.
55. H. Guo, M. Kemell, M. Heikkilä, and M. Leskelä, *Applied Catalysis B: Environmental*, 2010, **95**, 358–364.

56. T. K. Minton, B. Wu, J. Zhang, N. F. Lindholm, A. I. Abdulagatov, J. O'Patchen, S. M. George, and M. D. Groner, *ACS Applied Materials & Interfaces*, 2010, **2**, 2515–2520.
57. Q. Sun, H. Yu, Y. Liu, J. Li, Y. Lu, and J. F. Hunt, *Holzforschung*, 2010, 64, 757.
58. R. J. Phaneuf, A. E. Marquardt, E. Breitung, L. Henn-Lecordier, G. Rubloff, G. Gates, and T. Weisser, in *Abstracts of Papers, 241st ACS National Meeting & Exposition*, Anaheim, CA, 2011.
59. T. W. Scharf, D. R. Diercks, B. P. Gorman, S. V Prasad, and M. T. Dugger, *Tribology Transactions*, 2009, **52**, 284–292.
60. E. Cianci, S. Lattanzio, G. Seguni, and M. Fanciulli, *Thin Solid Films*, 2012, **520**, 4745–4748.
61. R. K. Grubbs, C. E. Nelson, N. J. Steinmetz, and S. M. George, *Thin Solid Films*, 2004, **467**, 16–27.
62. K. Nevalainen, R. Suihkonen, P. Etelaaho, J. Vuorinen, P. Jarvela, N. Isomaki, C. Hintze, and M. Leskela, *J. Vac. Sci. Technol. A*, 2009, **27**, 929–936.
63. R. Tilley, *Colour and the optical properties of materials : an exploration of the relationship between light, the optical properties of materials and colour*, Wiley, Chichester, West Sussex, UK, 2nd edn., 2011.
64. A. Lamminpää, S. Nevas, F. Manoocheri, and E. Ikonen, *Applied Optics*, 2006, **45**, 1392–1397.
65. M. V Diamanti, B. Del Curto, and M. P. Pedefferri, *Color Research and Application*, 2008, **33**, 221–228.

66. U. Beck, G. Reiners, I. Urban, and K. Witt, *Thin Solid Films*, 1992, **220**, 234–240.
67. S. Niyomsoan, W. Grant, D. L. Olson, and B. Mishra, *Thin Solid Films*, 2002, **415**, 187–194.
68. K. A. Tsokos, *Physics for the IB Diploma*, Cambridge Univ. Press, Cambridge, Fifth., 2008.
69. A. Luque and S. Hegedus, Eds., *Handbook of photovoltaic science and engineering*, Wiley, Chichester, West Sussex, U.K., 2nd edn., 2011.
70. R. Singh, PhD Thesis, McMaster Univeristy, 1979.
71. D. L. Pulfrey, *Electron Devices, IEEE Transactions on*, 1978, **25**, 1308–1317.
72. M. Green and R. Godfrey, *Applied Physics Letters*, 1976, **29**, 610–612.
73. S. J. Fonash, *Journal of Applied Physics*, 1975, **46**, 1286–1289.
74. S. Ashok, P. P. Sharma, and S. J. Fonash, *IEEE Transactions on Electron Devices*, 1980, **27**, 725–730.
75. A. K. Ghosh, C. Fishman, and T. Feng, *Journal of Applied Physics*, 1979, **50**, 3454–3458.
76. S. Admassie, F. Zhang, A. G. Manoj, M. Svensson, M. R. Andersson, and O. Inganäs, *Solar Energy Materials and Solar Cells*, 2006, **90**, 133–141.
77. V. S. Saji, *Recent Patents on Corrosion Science*, 2010, **2**, 6–12.
78. A. Stankiewicz, I. Szczygieł, and B. Szczygieł, *J. Mat. Sci.*, 2013.
79. R. Bhure and A. Mahapatro, *Silicon*, 2010, **2**, 117–151.

80. M. Guglielmi, *Journal of Sol-Gel Science and Technology*, 1997, **8**, 443–449.
81. N. Chawla, D. R. P. Singh, Y.-L. Shen, G. Tang, and K. K. Chawla, *Journal of Materials Science*, 2008, **43**, 4383–4390.
82. M. Makela, P. Soininen, and S. Sneck, 2009.
83. A. L. Brazeau and S. T. Barry, *Chemistry of Materials*, 2008, **20**, 7287–7291.
84. C. Kisielowski, J. Krüger, S. Ruvimov, T. Suski, J. W. Ager III, E. Jones, Z. Liliental-Weber, M. Rubin, E. R. Weber, M. D. Bremser, and R. F. Davis, *Physical Review B*, 1996, **54**, 17745–17753.
85. M. D. Groner, J. W. Elam, F. H. Fabreguette, and S. M. George, *Thin Solid Films*, 2002, **413**, 186–197.
86. M. Ritala, M. Leskela, L. Niinisto, and P. Haussalo, *Chemistry of Materials*, 1993, **5**, 1174–1181.
87. R. Baribeau, W. S. Neil, and E. Côté, *Journal of Modern Optics*, 2009, **56**, 1497–1503.
88. L. Simonot, M. Hébert, and D. Dupraz, *Color Research & Application*, 2011, **36**, 169–178.
89. E. Palik, Ed., *Handbook of Optical Constants of Solids*, Naval Research Laboratory, Washington, DC, 1985.
90. D. Lide, *CRC Handbook of Chemistry and Physics*, Taylor & Francis Group, Boca Raton, FL, 86th edn., 2005.

91. M. Groner, F. Fabreguette, J. Elam, and S. George, *Chemistry of Materials*, 2004, 639–645.
92. E. Born and M. Wolf, *Principles of Optics*, Cambridge Univ. Press, 7th edn., 2001.
93. E. C. Carter, Y. Ohno, M. R. Pointer, A. R. Robertson, R. Sève, J. D. Schanda, and K. Witt, Eds., *CIE 15-2004: Colorimetry*, 3rd edn.
94. *ISO 11664-1:2008(E)/CIE S 014-1/E:2006: Joint ISO/CIE Standard: CIE Colorimetry — Part 1: Standard Colorimetric Observers.*, .
95. *ISO 11664-2:2008(E)/CIE S 014-2/E:2006: Joint ISO/CIE Standard: CIE Colorimetry — Part 2: Standard Illuminants for Colorimetry.*, .
96. M. D. Fairchild, *Color Appearance Models*, Wiley-IS&T, Chichester, UK, 2nd edn., 2005.
97. *CIE S 014-4.3/E:2007: Colorimetry—Part 4: CIE 1976 L*a*b* colour space.*, .
98. N. K. Swami, S. Srivastava, and H. M. Ghule, *Journal of Physics D: Applied Physics*, 1979, **12**, 765.
99. D. L. Pulfrey, *Electron Devices, IEEE Transactions on*, 1978, 25, 1308–1317.
100. S. Sun and N. Sariciftci, *Organic Photovoltaics: Mechanisms, Materials, and Devices*, Taylor & Francis, Boca Raton, FL, 2005.
101. G. Dingemans, R. Seguin, P. Engelhart, M. C. M. Van De Sanden, and W. M. M. Kessels, *Physica Status Solidi - Rapid Research Letters*, 2010, **4**, 10–12.
102. H. M. Branz, V. E. Yost, S. Ward, K. M. Jones, B. To, and P. Stradins, *Applied Physics Letters*, 2009, **94**, 231121.

103. X. Li and P. W. Bohn, 2000, **77**, 2572–2574.
104. T. Hadjersi, N. Gabouze, N. Yamamoto, C. Benazzouz, and H. Cheraga, *Vacuum*, 2005, **80**, 366–370.
105. N. Geyer, B. Fuhrmann, Z. Huang, J. de Boor, H. S. Leipner, and P. Werner, *The Journal of Physical Chemistry C*, 2012, **116**, 13446–13451.
106. M. L. Green, E. P. Gusev, R. Degraeve, and E. L. Garfunkel, *Journal of Applied Physics*, 2001, **90**, 2057–2121.
107. A. Tataroğlu and Ş. Altındal, *Microelectron. Eng.*, 2008, **85**, 233–237.
108. S. Sze, *Physics of Semiconductor Devices*, John Wiley & Sons, Inc., New York, 1981.
109. S. R. Wenham, M. A. Green, M. E. Watt, and R. Corkish, Eds., *Applied Photovoltaics*, Routledge, Sterling, VA, 2nd edn., 2007.
110. T. J. J. Whitehorne, Carleton University, 2009.
111. J. P. Lock, S. G. Im, and K. K. Gleason, *Macromolecules*, 2006, **39**, 5326–5329.
112. M. Fabretto, K. Zuber, C. Hall, and P. Murphy, *Macromolecular Rapid Communications*, 2008, **29**, 1403–1409.
113. A. P. Kenney, G. P. A. Yap, D. S. Richeson, and S. T. Barry, *Inorganic chemistry*, 2005, **44**, 2926–33.
114. A. P. Milanov, R. A. Fischer, and A. Devi, *Inorganic Chemistry*, 2008, **47**, 11405–11416.

115. G. A. DiLabio, G. Litwinienko, S. Lin, D. A. Pratt, and K. U. Ingold, *The Journal of Physical Chemistry A*, 2002, **106**, 11719–11725.
116. J. P. Coyle, P. A. Johnson, G. A. DiLabio, S. T. Barry, and J. Müller, *Inorganic Chemistry*, 2010, **49**, 2844–2850.
117. L. Lutterotti, *Nuclear Instruments and Methods in Physics Research Section B: Beam Interactions with Materials and Atoms*, 2010, **268**, 334–340.
118. D. Beena, K. J. Lethy, R. Vinodkumar, V. P. Mahadevan Pillai, V. Ganesan, D. M. Phase, and S. K. Sudheer, *Applied Surface Science*, 2009, **255**, 8334–8342.
119. A. J. Downs, Ed., *Chemistry of Aluminium, Gallium, Indium, and Thallium*, Blackie Academic & Professional, London, 1993.
120. G. M. Sheldrick, *Acta Crystallographica Section A*, 2008, **64**, 112–122.
121. W. H. Weber and S. L. McCarthy, *Physical Review B*, 1975, **12**, 5643–5650.
122. E. Ozbay, *Science*, 2006, **311**, 189–193.
123. P. Doppelt, *Coordination Chemistry Reviews*, 1998, **178–180**, **P**, 1785–1809.
124. V. Miikkulainen, M. Leskelä, M. Ritala, and R. L. Puurunen, *Journal of Applied Physics*, 2013, **113**, 021301.
125. T. J. Wenzel, E. J. Williams, R. C. Haltiwanger, and R. E. Sievers, *Polyhedron*, 1985, **4**, 369–378.
126. P. Maartensson and J. Carlsson, *Journal of The Electrochemical Society*, 1998, **145**, 2926–2931.

127. K.-H. Park and W. J. Marshall, *Journal of the American Chemical Society*, 2005, **127**, 9330–9331.
128. Z. Li, A. Rahtu, and R. G. Gordon, *Journal of The Electrochemical Society*, 2006, **153**, C787–C794.
129. Z. Li, S. T. Barry, and R. G. Gordon, *Inorganic chemistry*, 2005, **44**, 1728–35.
130. B. S. Lim, A. Rahtu, and R. G. Gordon, *Nat Mater*, 2003, **2**, 749–754.
131. B. S. Lim, A. Rahtu, J.-S. Park, and R. G. Gordon, *Inorganic chemistry*, 2003, **42**, 7951–8.
132. J. P. Coyle, W. H. Monillas, G. P. A. Yap, and S. T. Barry, *Inorganic chemistry*, 2008, **47**, 683–9.
133. J. W. Park, H. S. Jang, M. Kim, K. Sung, S. S. Lee, T.-M. Chung, S. Koo, C. G. Kim, and Y. Kim, *Inorganic Chemistry Communications*, 2004, **7**, 463–466.
134. V. V Grushin and W. J. Marshall, *Advanced Synthesis & Catalysis*, 2004, **346**, 1457–1460.
135. Z. Yuan, N. Dryden, J. J. Vittal, and R. J. Puddephatt, *Chemistry of Materials*, 1995, **7**, 1696–1702.
136. M. Kariniemi, J. Niinistö, T. Hatanpää, M. Kemell, T. Sajavaara, M. Ritala, and M. Leskelä, *Chemistry of Materials*, 2011, **23**, 2901–2907.
137. J. D. Caldwell, O. J. Glembocki, F. J. Bezares, M. I. Kariniemi, J. T. Niinistö, T. T. Hatanpää, R. W. Rendell, M. Ukaegbu, M. K. Ritala, S. M. Prokes, C. M. Hosten, M. A. Leskelä, and R. Kasica, *Opt. Express*, 2011, **19**, 26056–26064.

138. S. M. Prokes, O. J. Glembocki, E. Cleveland, J. D. Caldwell, E. Foos, J. Niinisto, and M. Ritala, *Applied Physics Letters*, 2012, **100**, 53106.
139. E. R. Cleveland, O. Glembocki, and S. M. Prokes, *Proc. SPIE 8467, Nanoepitaxy: Materials and Devices IV*, 2012, 84670H–84670H–6.
140. S. M. Prokes, O. J. Glembocki, and E. Cleveland, *Proc. SPIE 8467, Nanoepitaxy: Materials and Devices IV*, 2012, 84670F–84670F–12.
141. T. J. J. Whitehorne, J. P. Coyle, A. Mahmood, W. H. Monillas, G. P. a. Yap, and S. T. Barry, *European Journal of Inorganic Chemistry*, 2011, **2011**, 3240–3247.
142. L.-Y. Shao, J. P. Coyle, S. T. Barry, and J. Albert, *Optical Materials Express*, 2011, **1**, 128.
143. A. M. James, R. K. Laxman, F. R. Fronczek, and A. W. Maverick, *Inorganic Chemistry*, 1998, **37**, 3785–3791.
144. P. B. Hitchcock, M. F. Lappert, and L. J.-M. Pierssens, *Chem. Commun.*, 1996, **0**, 1189–1190.
145. S. D. Bunge, O. Just, and W. S. Rees Jr., *Angew. Chem. Int. Ed.*, 2000, **39**, 3082–3084.
146. J. P. Coyle, P. Johnson, G. DiLabio, J. Müller, and S. T. Barry, in *Proceedings of the AVS Atomic Layer Deposition Conference*, 2009.
147. L. C. Ziffle, A. P. Kenney, S. T. Barry, and J. Müller, *Polyhedron*, 2008, **27**, 1832–1840.

148. J. P. Coyle, A. Kurek, P. J. Pallister, E. R. Sirianni, G. P. a Yap, and S. T. Barry, *Chemical Communications*, 2012, **48**, 10440–2.
149. J. P. Coyle, P. J. Pallister, A. Kurek, E. R. Sirianni, G. P. a Yap, and S. T. Barry, *Inorganic chemistry*, 2013, **52**, 910–7.
150. G. V Kunte, S. A. Shivashankar, and A. M. Umarji, *Measurement Science and Technology*, 2008, **19**, 25704.
151. Q. Ma, H. Guo, R. G. Gordon, and F. Zaera, *Chemistry of Materials*, 2011, **23**, 3325–3334.
152. T. Kim, Y. Yao, J. P. Coyle, S. T. Barry, and F. Zaera, *Chem. Maters.*, 2013, **submitted**.
153. R. Uson, A. Laguna, M. Laguna, D. A. Briggs, H. H. Murray, and J. P. Fackler, in *Inorganic Syntheses*, John Wiley & Sons, Inc., 1989, pp. 85–91.
154. I. Horcas, R. Fernández, J. M. Gómez-Rodríguez, J. Colchero, J. Gómez-Herrero, and a M. Baro, *The Review of scientific instruments*, 2007, **78**, 013705.
155. D. Murias, C. Reyes-Betanzo, M. Moreno, A. Torres, A. Itzmoyotl, R. Ambrosio, M. Soriano, J. Lucas, and P. R. i Cabarrocas, *Materials Science and Engineering: B*, 2012, **177**, 1509–1513.
156. J. C. C. Fan and J. B. Goodenough, 1977, **4**, 3524–3531.
157. P. K. Biswas, A. De, L. K. Dua, and L. Chkoda, *Bulletin of Materials Science*, 2006, **29**, 323–330.